Università degli Studi di Cagliari

Ph.D. DEGREE
in Industrial Engineering
Cycle XXXIV

TITLE OF THE Ph.D. THESIS

Experimental and numerical investigations of Wells turbines for wave energy conversion

Scientific Disciplinary Sector(s)
ING-IND/08

Ph.D. Student:	Fabio Licheri
Supervisors:	Prof. Pierpaolo Puddu Prof. Giorgio Cau

Final exam. Academic Year 2020/2021
Thesis defence: April 2022 Session

Questa Tesi può essere utilizzata, nei limiti stabiliti dalla normativa vigente sul Diritto d'Autore (Legge 22 aprile 1941 n. 633 e succ. modificazioni e articoli da 2575 a 2583 del Codice civile) ed esclusivamente per scopi didattici e di ricerca; è vietato qualsiasi utilizzo per fini commerciali. In ogni caso tutti gli utilizzi devono riportare la corretta citazione delle fonti. La traduzione, l'adattamento totale e parziale, sono riservati per tutti i Paesi. I documenti depositati sono sottoposti alla legislazione italiana in vigore nel rispetto del Diritto di Autore, da qualunque luogo essi siano fruiti.

This Thesis can be used, within the limits established by current legislation on Copyright (Law 22 April 1941 n. 633 and subsequent amendments and articles from 2575 to 2583 of the Civil Code) and exclusively for educational and research purposes; any use for commercial purposes is prohibited. In any case, all uses must report the correct citation of the sources. The translation, total and partial adaptation, are reserved for all countries. The documents filed are subject to the Italian legislation in force in compliance with copyright, from wherever they are used

Abstract

This thesis deals with the evaluation of the performance of a Wells turbine both with experimental and numerical investigations. In particular, results are used to highlight the contribution of different loss sources in determining the turbine efficiency.

Numerical investigations have been focused at calculating the turbine efficiency using both direct and indirect methods, i.e. by considering the quantities of interest at the inlet and at the outlet of the turbine, as well as through the estimation of entropy generation inside the domain.

Experimental investigations have been conducted at the University of Cagliari in a facility equipped with an Oscillating Water Column (OWC) simulator and a Wells turbine. The facility has been modified following a modular design of the test section, which allows an easier modification of the rotor configuration and simpler access to the test section for local flow investigations. Investigations have been focused on the determination of Wells turbine performance, both with global measurements (such as torque and static pressure drop) and detailed local measurements. Local investigations were carried out using aerodynamic probes and hot-wire anemometer (HWA), in order to reconstruct the flow field near the turbine, hence to estimate also the local performance and losses.

The analysis of turbine' s performance suggests two possible solutions to improve Wells turbine performance under periodic unsteady flow conditions, characteristic of the OWC device. The first solution is based on controlling the rotational speed of the rotor, while the second one requires a modification of the pitch of the rotor blade to control the incidence angle at different flow rates. The former solution has been experimentally investigated in the facility available at the University of Cagliari, while the latter has been evaluated by means of two dimensional CFD simulations.

Contents

List of Figures 9

List of Tables 13

1 Introduction 15

2 Wells turbine performance definition 21

2.1 Performance definitions 22

2.2 Second-law analysis 23

2.2.1 Linking first- and second-law efficiency 24

2.3 Losses in the Wells turbine 26

2.4 Additional performance parameters 29

3 Turbine efficiency calculation by means of CFD 31

3.1 Entropy calculation from CFD (RANS) simulations 33

3.1.1 Evaluation of entropy production with different turbulence models 35

3.2 Methodology 36

3.2.1 Verification and validation 40

3.3 Comparison among different turbulence models 44

3.3.1 Simulations for $\phi_{max} = 0.23$ 45

3.3.2 Simulations for $\phi_{max} = 0.345$ 49

3.4 Comparisons among different rotor geometries 51

4 Modifications to the facility housed at DIMCM 57

4.1 The existing facility 57

4.2 The new rig 60

4.3 A “modular” Wells turbine 63

5 Experimental characterization of a Wells turbine 65

5.1 Inertia and windage losses 67

5.2 Stall limit under stationary flow 69

5.3 Turbine behavior under non-stationary flow 70

5.3.1 Global performance 71

5.3.2 Local measurements and performance 74
5.4 Measurements with the HWA probe 83

6 Solutions to improve Wells turbines performance 91
6.1 The variable speed control 93
6.2 The variable pitch rotor blades 98
6.2.1 Stall limit and pitch-control law 101
6.2.2 Performance comparisons 101

7 Conclusions 105
7.1 Future investigations 107

A Comparison between fixed and rotating spinner 111

B Wall-proximity effects on “wedge” measurements 115

C Instrumentation data 119

Bibliography 121

List of Figures

1.1 Schematic views of an on-shore OWC system with a Wells turbine. . 16

2.1 Representation of specific works on the $T - s$ plane 25
2.2 Expansion through the Wells rotor in the $h - s$ diagram. 27
2.3 Velocity triangles at inlet and outlet of a Wells turbine. 28
2.4 Losses components for efficiency evaluation ($\beta_2 = 10°$, $\psi = 0.9$). . . . 29

3.1 Computational domain and details of the mesh (about 2 million cells) used for simulations. 38
3.2 Inlet boundary condition for dynamic simulations, in terms of flow coefficient ϕ. 39
3.3 Grid convergence analysis of non-dimensional parameters evaluated with five grid sizes. 41
3.4 Validation of grid (C) with the experimental data (dotted line) from [1]. 42
3.5 Verification of the temporal discretization using five different time-step sizes, for a maximum flow coefficient $\phi_{max} = 0.23$. 43
3.6 Verification of the temporal discretization using five different time-step sizes, for a maximum flow coefficient $\phi_{max} = 0.325$. 45
3.7 Non-dimensional performance of the rotor with NACA0015 blade profile and 6 blades, as a function of the flow coefficient ϕ, estimated with different turbulent closure models. 46
3.8 Non-dimensional entropy production averaged on a cycle. 46
3.9 Total exergy calculations averaged on a cycle for different turbulence closure models. 48
3.10 Close-up view of the non-dimensional entropy production at several blade span positions for the maximum flow coefficient $\phi = 0.23$ calculated using $k - \omega$ SST (left) and $k - \varepsilon$ STD (right) models 49
3.11 Rotor efficiencies averaged on cycle and calculated with different turbulence closure models 49
3.12 Non-dimensional performance of the rotor with NACA0015 blade profile and 6 blades under deep stall conditions, as a function of the flow coefficient ϕ, estimated with different turbulent closure models. 50

3.13 Iso-surfaces of Q criterion ($Q = 2.25\text{e}6\ \text{s}^{-2}$) colored by non-dimensional entropy production 51
3.14 Non-dimensional performance of the rotor with 6 blades and different blade profiles, as a function of the flow coefficient ϕ. 52
3.15 Non-dimensional performance of the rotor with NACA0020 blade profile and different number of blades, as a function of the flow coefficient ϕ. 52
3.16 Non-dimensional entropy production averaged on a cycle for different rotor geometries 53
3.17 Non-dimensional entropy production at several blade span positions for the maximum flow coefficient $\phi = 0.23$ and for rotor with $z = 5$ (left), $z = 6$ (center) and $z = 7$ (right) 54
3.18 Iso-surfaces of Q criterion ($Q = 2.25\text{e}6\ \text{s}^{-2}$) colored by non-dimensional entropy production for different flow conditions and for rotor with $z = 5$ (left), $z = 6$ (cent) and $z = 7$ (right) 55
3.19 Energy averaged on a cycle for different rotor geometries. 55
3.20 Rotors efficiencies averaged on a cycle for different rotor geometries. . 56

4.1 Simplified scheme of the experimental rig. 58
4.2 Close-up view of the turbine and of the top part of the experimental setup. 59
4.3 Motorized traversing system used for local measurements. 60
4.4 3-dimensional section view of the new rig with the modular Wells turbine. 61
4.5 Detailed pics of the novel rig. 62
4.6 Demonstrative views of the modular Wells turbine. 63

5.1 Windage and friction torque losses as a function of the rotational frequency of the turbine. 67
5.2 Typical test for inertia calculation. 68
5.3 Non-dimensional piston position as a function of the non-dimensional piston period in case of triangular wave form. 69
5.4 Non-dimensional performance under stationary flow. 69
5.5 Non-dimensional piston motion in experiments. 70
5.6 Non-dimensional performance under non-stationary flow. 71
5.7 Turbine global efficiency for different working conditions. 72
5.8 Flow angles calculated from global measurements. 73
5.9 Loss components and velocity reduction coefficient. 74
5.10 Schematic view of the “wedge” probe. 75
5.11 Non-dimensional calibration coefficients for the “Wedge” probe. . . . 76
5.12 Non-dimensional velocity distribution along the blade span for the maximum flow coefficient. 77

5.13 Velocity components and flow angles at turbine's inlet, for the inflow (solid line) and the outflow phase (dashed line), measured at blade midspan, as a function of the piston position. 78
5.14 Velocity components and flow angles at turbine's inlet, for the inflow (solid line) and the outflow phase (dashed line), measured along the blade span for the maximum flow coefficient. 79
5.15 Velocity components and flow angles at turbine's outlet, for the inflow (solid line) and the outflow phase (dashed line), measured at blade midspan, as a function of the piston position. 79
5.16 Velocity components and flow angles at turbine's outlet, for the inflow (solid line) and the outflow phase (dashed line), measured along the blade span for the maximum flow coefficient. 80
5.17 Contour plots of the performance parameters for the two phases. . . . 81
5.18 Performance parameters for the inflow (solid line) and the outflow phase (dashed line), calculated along the blade span for three flow coefficients. 82
5.19 Components of losses of the turbine during both the two phases. . . . 83
5.20 Schematic view of the DANTEC 55P12 HWA probe and its positioning near the rotor. 84
5.21 DANTEC 55P12 angular calibration. 85
5.22 HW measurements of turbulence intensity upstream the rotor, during both the inflow and the outflow phase, as a function of the non-dimensionalized blade pitch. 87
5.23 Contour plots of relative velocity components downstream the rotor, in two adjacent blade vanes. 88
5.24 Velocity components of the absolute flow and their extrapolated mean values (dashed line) as a function of the non-dimensional radius. . . . 89
5.25 Kinetic energy defect. 90

6.1 Control law for the rotational speed based on the best efficiency condition. 94
6.2 Comparison of the velocity reduction coefficient between the controlled turbine (red and blue dots) and the not-controlled turbine (black dots). 95
6.3 Comparison of turbine efficiencies for the two control laws with respect to their uncontrolled values. 95
6.4 Frequency distribution of operating conditions during a piston period for the controlled and the uncontrolled rotor. 96
6.5 Comparison of the flow angles for controlled and uncontrolled turbine. 96
6.6 Rotor efficiencies averaged on a cycle for the turbine with and without control. 97
6.7 Velocity triangles at inlet of the turbine with variable pitch blades. . 98
6.8 Blocking scheme and detailed view of the mesh around the blade. . . 99

6.9 Control laws for the pitch angle based on maximum output torque condition and self-actuated law. 101
6.10 Non-dimensional performance compared between controlled and not-controlled solutions. 102
6.11 Non-dimensional performance comparison, as a function of the pressure drop coefficient. 102

A.1 Computational domain. 111
A.2 Computational grid in the moving-reference-frame zone. 112
A.3 Non-dimensional performance comparison, as a function of the static pressure drop coefficient. 112
A.4 Velocity components at turbine's inlet and outlet during the outflow phase, as a function of the non-dimensional radius. 113
A.5 Comparison of local performance parameters during both the two phases. 113

B.1 Low-speed wind tunnel. 115
B.2 Correction factors for wall-proximity effects of the “wedge” probe. . . 116

List of Tables

3.1 Geometric and operating data from [1]. 37
3.2 Grid convergence estimation using grids B, C, D. 41
3.3 Grid convergence estimation using grids C, D, E. 42

4.1 High solidity Wells turbine data. 59

5.1 Geometric parameters of the novel low solidity Wells turbine. 65
5.2 Settings of experiments. 70
5.3 Settings for local investigations. 76
5.4 Hot-wire probe uncertainties. 85
5.5 Settings of HWA tests. 86

6.1 Constant values used for passive control. 100

Chapter 1

Introduction

The growing demand for renewable energy has drawn the attention to the strong potential of ocean-wave energy [2], with is global gross theoretical resource of about 2÷3.7 TW [3, 4]. Global evaluations on the potential of this renewable source have been developed in the last decades [4, 5], as well as regional analyses focused on the estimation of the overall amount of available energy and on its regularity [6–12]. Of particular interest for the present work are the analyses carried out in Europe [13] and more specifically in the Mediterranean Sea [14–20], which show that North West coasts of Sardinia are one of the most preferable site in Mediterranean Sea, with a estimated averaged energy of about $33.5 \div 95.5$ MWh/m per year. Local wave energy estimations in Mediterranean Sea have oriented also to the selection of the best Wave Energy Converter (WEC) for different sites of interest [20] for offshore installations.

Many concepts and designs of WECs have been proposed during the last four decades [21–23], as well as solutions and modifications to improve the most promising designs [24–27]. In particular, WECs devices can be grouped into three main categories [24, 28]: Oscillating Water Columns (OWCs), oscillating body systems and overtopping systems. The high reliability and simplicity of construction, mainly due to the absence of moving parts submerged into the seawater [29], and, in general, a reduced number of moving parts [25], makes the OWC technology the most attractive, also thanks to the possibility to apply the OWC concept in different locations and on different collectors platforms [22]. Electrical energy production with OWC systems is generally obtained with two conversion stages, starting from the potential energy contained in wave motion. Figure 1.1 (a) presents a schematic view of the two main units that compose an OWC: an open chamber, partially submerged under the sea free surface, and the power-take-off (PTO). In the open chamber the water movement induces an alternative movement of a column of air and the wave energy is converted into pneumatic energy of the bi-directional airflow of a mass of air. The PTO, generally an air turbine, driven by the airflow, converts the pneumatic energy into mechanical energy.

The bi-directional nature of the airflow inside the chamber of the OWC represents

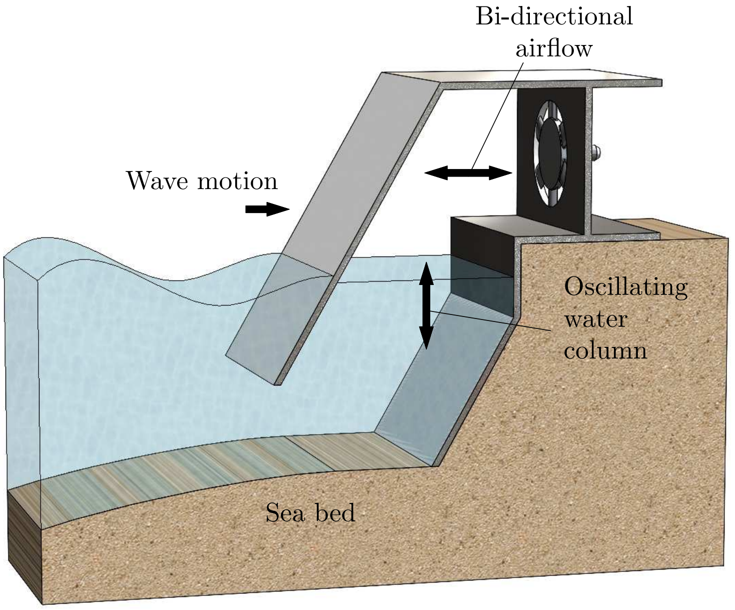
Bi-directional
airflow
Wave motion
Oscillating
water
column
Sea bed

(a) Schematic of the OWC system.

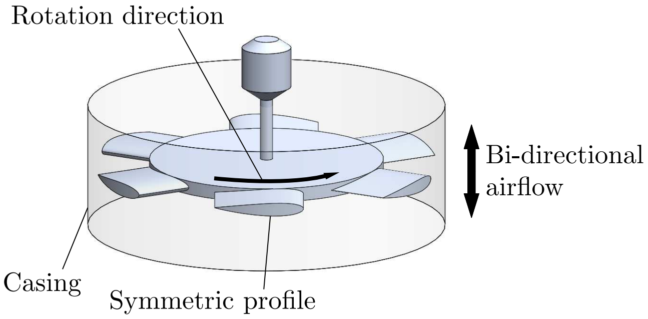
Rotation direction
Bi-directional
airflow
Casing
Symmetric profile

(b) Wells turbine working principle.

Figure 1.1: Schematic views of an on-shore OWC system with a Wells turbine.

a challenge in turbine selection [30, 31]. The periodic inversion of the air flow in the OWC chamber requires a system that is capable of maintaining the same direction of rotation regardless of the direction of the air flow. Non-return valve arrangements have been proposed to rectify the flow [32] in one of the first OWC installation in early 1980s. This large-scale WEC, i.e. the Kaimei designed by Yoshio Masuda, was equipped with conventional unidirectional turbines tested together with self-rectifying turbines. Traditional turbines, such as for example impulse turbines, can be coupled with OWCs [31,33,34] by introducing pneumatic valves or, alternatively, by using stator blades on both sides of the rotor. More recently, bi-radial turbines [35–38] and double-decker turbines [39, 40] have been proposed to be coupled with OWC devices.

The Wells turbine, patented by Dr. A. A. Wells in 1970s [41], is characterized by a symmetrical blade profile staggered at 90 degrees with respect to the axis of rotation, and it represents a solution of self-rectifying air turbine, see Fig. 1.1 (b), which ensures similar performance during the outflow (air flowing out of the chamber) and the inflow phase (air flowing into the chamber). Its simplicity of construction has made the Wells turbine the most used turbine in OWC devices [42], e.g. in the Mighty Whale device (Japan) [43], in the Pico Power Plant (Azores, Portugal) [44], in the LIMPET device (Islay, Scotland) [45] and in the Mutriku Wave Energy Plant (Basque Country, Spain) [46]. Besides its strengths, i.e. simplicity of construction and reliability, a number of weakness have been highlighted in Wells turbines operation [42, 47], and they drawing the attention of researchers:

- low tangential force, i.e. poor torque and power output,
- a relatively low aerodynamic efficiency,
- a limited operating range due to stall.

Experimental studies have been conducted under steady [48–54] and unsteady flow conditions with facilities representative of OWC simulators [1, 55–61]. Performance of traditional monoplane Wells turbines have been investigated in [59] under unsteady flow conditions obtained by acting on turbine rotational speed, while performance under bi-directional airflow, as in OWC systems, has been determined in [1, 55–57], with particular attention to the effects of the motion frequency on turbine performance. More detailed local measurements on the monoplane Wells turbine have been carried out in [58, 61], in order to evaluate its aerodynamic performance under a non-stationary bi-directional airflow. Several geometries have been experimentally tested in [48, 51], in order to quantify the effects of solidity and blade shape on performance, while [49, 52] investigate the behavior of a Wells rotor with variable-pitch rotor blades, a solution of particular interest to extend the limited operating range of the traditional turbine and avoid stall. Of particular interest for real installations are the measures on the aero-acoustic characteristics of the monoplane Wells turbine, as presented in [53]. Biplane and contra-rotating Wells turbines [50, 54, 60], with and without guide-vanes on both sides of the turbine or in between the two rotors, have been also proposed in order to reduce the kinetic energy of the exit flow and to improve turbine's global efficiency.

A wide number of numerical analyses have been carried out in the last decades, also due to the high diffusion of software for Computational Fluid Dynamics (CFD). Numerical simulations have been used to estimate the turbine performance [62–64], in particular when flow conditions are sever, e.g. under incipient and deep stall conditions [65, 66]. Numerical analyses gave a great impulse to researches of improved solutions with higher performance. The effects of design parameters, such as profile thickness and rotor solidity, on turbine performance, have been calculated in [67–70] while [71, 72] proposed a optimized design of the turbine and of the blade shape [73], in order to overcome the limitations of the symmetrical profile, that leads to a limited lift at low incidence angles and the occurrence of stall at high flow coefficients. Performance improvements have been researched also with unconventional blade designs [74–76] or by simulating control strategies as pitch-controlled blades [77–79], in order to extend the operating range and avoid stall at high flow coefficients. Combined structural and fluid dynamics calculations have been used to investigate the effectiveness of flexible blades [80, 81] which can change their shape, accordingly to the incident flow, by modifying the typical symmetric profile to a cambered one. Of particular interest for the present work are the recent numerical analyses conducted to estimate blade performance from a second-law point of view, by applying the exergy balance and by calculating the entropy produced by the airflow through the machine [82–89]. Finally, numerical approaches, not necessary based on CFD simulations, have been adopted to evaluate the unsteady performance of the Wells turbine and in particular to deeply understand the hysteresis behavior of Wells turbines highlighted by a number of authors [90–92]. More recently, the hysteresis phenomenon has been explained by means of CFD methods [93] and simplified numerical approaches [94, 95], all supported by experimental measurements [57].

Some works summarized in this introduction, sometimes suggests turbine modifications and enhancements solutions not always based on a deep knowledge of the mechanism of losses that characterize the Wells turbine performance. For example, great attention has been paid to recover the exit kinetic energy downstream the Wells rotor, identified as the most important source of loss that affect its efficiency. Solutions based on guide-vanes [50, 96, 97], contra-rotating rotors [98, 99] and biplane [54, 100–102] Wells turbines have been considered and analyzed with numerical and experimental approaches. On the other hand, blade profile optimizations [73, 103] have been carried out, as well as different blade thicknesses of NACA 00xx profiles [88, 104] have been compared to find the blade geometry for the best rotor performance. The strong constraint of a symmetric profile that characterizes the Wells turbine, limited the blade profile optimizations, as well as the bi-directional operating mode do not ensure optimal performance of solutions for kinetic exit energy recovery during both the two airflow phases. But above all, the unsteady nature of the airflow does not allow the Wells turbine to operate in its best efficiency conditions. Control strategies of turbine rotational speed or blade stagger-angle arrangement have been proposed, but rarely tested in conditions similar to the ones that happens in OWCs. A deep knowledge of all these factors of efficiency reduction of the Wells turbines is necessary to lead the research of improvements. The relative importance of these effects is also helpful and unexplored at this moment.

In the present work, experimental and numerical investigations have been conducted to characterize the Wells turbine performance with a particular attention to the evaluation of its efficiency. The efficiency definition based on a second-law approach has been discussed and compared with traditional first-law based definitions. CFD simulations have been carried out to calculate the second-law efficiency for the Wells turbine, with particular attention to its correct estimation by means of CFD and to the turbulence closure models which are generally used for turbomachinery applications. The preliminary work on this topic has been presented at the 39th International Conference on Ocean, Offshore & Arctic Engineering [105] while a journal publication [83] summarizes the complete analyses.

Experimental investigations, conducted in the facility available at the University of Cagliari, have been focused on the Wells turbine performance evaluation using both global measurements (torque and static pressure drop through the rotor) and local measurements, carried out with aerodynamic pressure probes and with the hot-wire anemometer, in order to reconstruct the flow field near the turbine. Global and local analyses provide an accurate description which can lead the turbine optimization and increase understanding of turbine's aerodynamic behavior. The preliminary part of this work has been presented at the 76th Italian National Congress ATI [61], while a extended and more detailed version of these analyses is now under review for journal publication. Finally, a control strategy based on turbine's rotational speed has been experimentally investigated, in order to verify its effectiveness on turbine performance, while a numerical work, yet published in [78], investigates two different kind of controllers for a variable-pitch Wells turbine.

This report is organized as follows: Ch. 2 presents the definitions of Wells turbine performance and efficiency, based on first- and second-law approach; the efficiency decomposition has been also presented. Chapter 3 presents results of entropy calculation for several simulations of different Wells turbine configurations after a brief explanation on how the intermediate quantities, required to evaluate the turbine efficiency, can be calculated from CFD results. The modifications made to the experimental facility housed at the Department of Mechanical, Chemical and Materials Engineering (DIMCM) are presented in Ch. 4, with a brief description of the "modular" Wells turbine designed and used in the experimental investigations. Results from experiments are reported in Ch. 5, where global and local measurements are presented, as well as the turbine performance. Two control strategies to improve turbine performance, i.e. the control of the rotational speed of the rotor and variable-pitch rotor blades, have been analyzed with experiments, the former, and numerically, the latter. The results of the these investigations are presented in Ch. 6. Finally, Ch. 7 draws the conclusions of this work and suggests some future investigations.

Chapter 2

Wells turbine performance definition

In this Chapter, the Wells turbine performance is presented, with particular attention to the efficiency definition reported in literature. Its common definition, based on a first-law approach, is compared to the definition based on the second-law analysis, leading to some theoretic implications for the specific case of the Wells turbine. Finally, the efficiency expression is decomposed as done in typical turbomachinery analyses, in order to identify the main terms of losses.

List of symbols

	Non-dimensional properties
η	efficiency
λ	velocity coefficient
Λ	work coefficient
p^*	static pressure drop coefficient
p_t^*	total pressure drop coefficient
ψ	reduction coefficient of the relative velocity
ϕ	flow coefficient
$\mathcal{T}^*$	torque coefficient
ξ_{EX}	loss coefficient related to the exit kinetic energy
ξ_R	loss coefficient related to the
Y_P	relative total pressure loss coefficient

	Dimensional properties
α	angle of the absolute flow
β	angle of the relative flow
c	blade chord
C	absolute velocity
C^*	reference velocity
c_p	specific heat at constant pressure
$\dot{E}_x$	exergy per unit time
h	enthalpy
l	specific work
$\dot{m}$	mass flow rate
Ω	angular rotational frequency
p	pressure
Q	volumetric flow rate

r	turbine radius
ρ	air density
s	specific entropy
$\dot{S}_G$	entropy generation rate
T	temperature
$\mathcal{T}$	torque
U	peripheral rotor speed, blade speed
$\mathcal{V}$	volume
w	specific work
W	relative velocity
$\dot{W}$	work
X	turbine tangential force
Z	turbine axial force
	Subscripts and superscripts
1	inlet
2	outlet
ad	aerodynamic
II	second-law approach
d	dissipation
g	production
hub	turbine hub
II	second-law approach
in	input
is	isentropic
$lost$	lost
$loss$	loss
opt	optimal value
out	output
pol	polytropic
ref	reference value
rel	relative reference system
t	total condition
θ	tangential component
tip	turbine tip
ts	total-to-static
tt	total-to-total
z	axial component

2.1 Performance definitions

Performance of Wells turbine is usually presented [106] in terms of the following non-dimensional parameters: the flow coefficient ϕ, the torque coefficient $\mathcal{T}^*$ and the static and total pressure drop coefficients p^* and p_t^*, respectively:

$$\phi = \frac{C_z}{\Omega r_{tip}} \qquad \mathcal{T}^* = \frac{\mathcal{T}}{\rho \Omega^2 r_{tip}^5} \qquad p^* = \frac{\Delta p}{\rho \Omega^2 r_{tip}^2} \qquad p_t^* = \frac{\Delta p_t}{\rho \Omega^2 r_{tip}^2} \tag{2.1}$$

where C_z is the (spatially averaged) axial flow velocity in the turbine duct, ρ is the air density (assumed constant and equal to the ambient density), Ω is the angular velocity of the rotor, r_{tip} is its tip radius, $\mathcal{T}$ is the torque, p and p_t are the static and total pressures, respectively, and Δ represents the difference between inlet and outlet conditions of the rotor. These non-dimensional parameters can be experimentally evaluated without reconstructing the local flow field inside the turbine. In particular, the estimation of performance parameters in Eqn. (2.1) needs to measure the torque at turbine shaft, the speed of rotation of the rotor, the axial flow velocity (or the volumetric flow rate) and the static or the total pressure drop through the rotor. Generally, the static pressure drop can be approximated by measuring the wall static pressure drop, as it is easier to measure near the rotor. In order to make evident when this measurement is used in the following analyses, the wall static pressure drop coefficient has been denoted as p_w^*.

As well known, the efficiency of a turbine is defined as the ratio between the useful output work and the available energy of the turbine. Two different formulations can be found in the scientific literature for Wells turbines, both entailing an assumption of incompressible flow [107]:

$$\eta_{ad} = \frac{\mathcal{T}\Omega}{\Delta p Q} \tag{2.2}$$

$$\eta_{tt} = \frac{\mathcal{T}\Omega}{\Delta p_t Q} \tag{2.3}$$

Several authors [48, 99, 108] use the formulation in Eqn. (2.2), as it contains parameters that can be more easily measured in experiments, i.e. the wall static pressure drop, and it is representative of the aerodynamic efficiency of the rotor

$$\eta_{ad} = \frac{\mathcal{T}\Omega}{\Delta p Q} = \frac{\mathcal{T}/r}{\Delta p \pi \left(r_{tip}^2 - r_{hub}^2\right) C_z/\Omega r} = \frac{X}{Z}\frac{1}{\phi} \tag{2.4}$$

where X and Z are axial and tangential forces.

Other authors [56,57,92,102,109] use Eqn. (2.3). It is the ratio between the rotor useful power and the power of an ideal (isentropic) process between the same initial and final total pressures (i.e., the available power), and it represents a *total-to-total* isentropic efficiency [107]. If the exhaust kinetic energy is entirely wasted, as in case of the Wells turbine [108, 110], the *total-to-static* isentropic efficiency definition is more appropriate than the *total-to-total* definition reported in Eqn. (2.3). Considering the subscripts 1 and 2 for the conditions upstream and downstream the rotor, respectively, the *total-to-static* efficiency reads as follows [108]:

$$\eta_{ts} = \frac{\mathcal{T}\Omega}{\left(p_{t1} - p_2\right) Q} \tag{2.5}$$

Even though this formulation is more representative of the energy conversion process in a Wells turbine, it has (seldom) been adopted both in experimental and numerical analyses.

2.2 Second-law analysis

In some recent works [84, 86–89], the efficiency presented in Eqn. (2.3) has been referred to as *first-law* efficiency, in contrast to a *second-law* efficiency derived from an exergy analysis.

Considering a steady-flow and adiabatic process, the exergy balance for an open system can be written as follows [111]:

$$\dot{E}_{x,in} - \dot{E}_{x,out} = \dot{W} + T_{t,ref}\dot{S}_G \tag{2.6}$$

where the net exergy flux per unit time ($\dot{E}_{x,in} - \dot{E}_{x,out}$) is equal to the sum of the rate of exergy due to the useful work ($\dot{W}$), and the lost exergy per unit time ($T_{t,ref}\dot{S}_G$). $\dot{S}_G$ represents the entropy generation rate inside the control volume and $T_{t,ref}$ is a reference temperature.

A *second-law efficiency* can be defined as the ratio between the useful work and the net exergy flux, i.e.:

$$\eta^{II} = \frac{\dot{W}}{\dot{E}_{x,in} - \dot{E}_{x,out}} = \frac{\dot{W}}{\dot{W} + T_{t,ref}\dot{S}_G} = \frac{\mathcal{T}\Omega}{\mathcal{T}\Omega + T_{t,ref}\dot{S}_G} \tag{2.7}$$

2.2.1 Linking first- and second-law efficiency

For a machine evolving an ideal gas, the Gibbs' equation integrated between the initial and final total conditions reads:

$$\int_1^2 \mathrm{d}h_t = \int_1^2 \frac{\mathrm{d}p_t}{\rho_t} + \int_1^2 T_t \,\mathrm{d}s \tag{2.8}$$

The term on the left hand side represents the actual work of the machine, w, the first term on the right hand side is the polytropic work, w_{pol}, and the last term represents the lost work, w_{lost}. Under the assumption of constant specific heats values and for a turbine:

$$|w| = \frac{|\dot{W}|}{\dot{m}} = -\int_1^2 \mathrm{d}h_t = c_p\,(T_{t1} - T_{t2}) \tag{2.9}$$

$$|w_{pol}| = \frac{|\dot{W}_{pol}|}{\dot{m}} = -\int_1^2 \frac{\mathrm{d}p_t}{\rho_t} \tag{2.10}$$

$$w_{lost} = \frac{\dot{W}_{lost}}{\dot{m}} = \int_1^2 T_t \,\mathrm{d}s \tag{2.11}$$

$$|w| = |w_{pol}| - w_{lost} \tag{2.12}$$

We can also define the isentropic work of the transformation at constant entropy between the initial and final total pressures

$$|w_{is}| = \frac{|\dot{W}_{is}|}{\dot{m}} = -\int_1^{2_{is}} \mathrm{d}h_t = c_p\,(T_{t1} - T_{t2,is}) \tag{2.13}$$

In Fig. 2.1 the polytropic, isentropic, actual and lost specific works for a machine evolving a compressible flow are graphically reported.

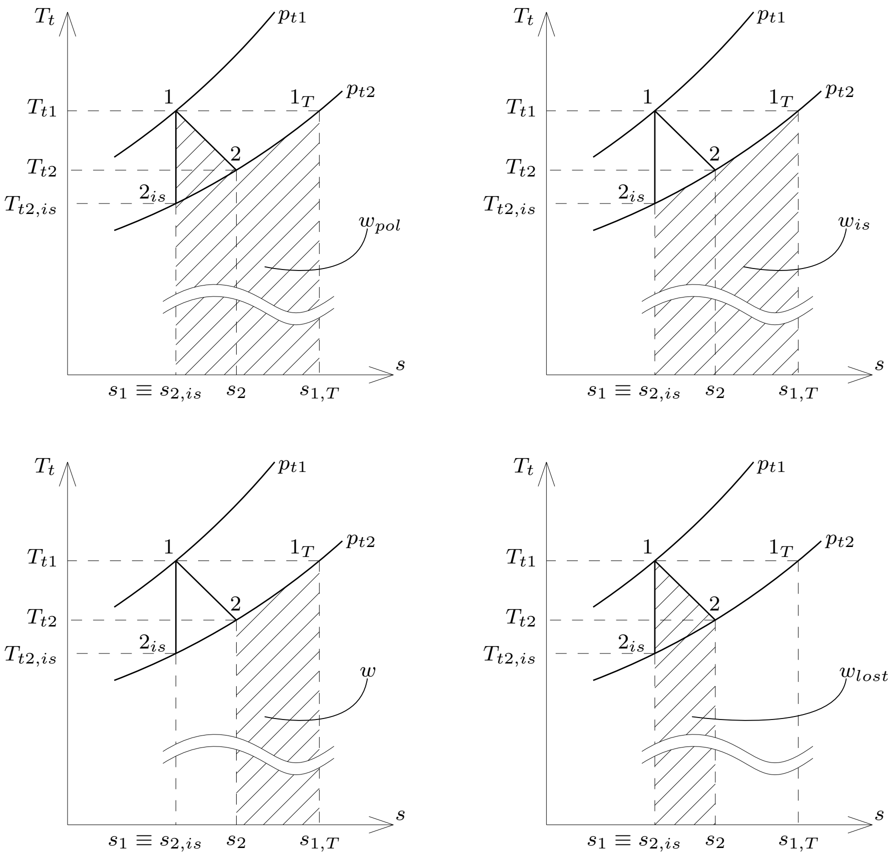

Figure 2.1: Representation of specific works on the $T - s$ plane

The isentropic work represents the maximum work that a turbine can exchange with the fluid (i.e. the available energy per unit time), while the polytropic work is the sum of actual work and lost work (due to friction). In a turbine, the polytropic work is always greater than the isentropic work, with the difference being the *heat recovery effect* [112].

$$|w_{pol}| = |w| + w_{lost} > |w_{is}| \tag{2.14}$$

Conversely, the isentropic efficiency $\eta_{is} = {}^{|w|}/_{|w_{is}|}$ is always greater than the polytropic efficiency $\eta_{pol} = {}^{|w|}/_{|w_{pol}|}$. The latter is more representative of the inefficiencies in a turbomachine, since it only considers the lost work.

For low pressure ratio machines (as in the case of Wells turbine) $(T_{t1} - T_{t2,is}) \ll T_{t1}$ and the following approximations can be made:

$$w_{pol} \approx w_{is} \implies \eta_{pol} \approx \eta_{is} \tag{2.15}$$

$$\int_1^2 T_t \, \mathrm{d}s \approx T_{t,ref} \, (s_2 - s_1) \tag{2.16}$$

provided that $T_{t,ref}$ is chosen appropriately (i.e. in the range of temperatures involved in the transformation), in order to obtain the area representing the energy lost in Fig. 2.1. Under these assumptions

$$|w| \approx |w_{pol}| - T_{t,ref}\,(s_2 - s_1) \tag{2.17}$$

In terms of powers, observing that for low speed flows ρ_t can be approximated with the static density, ρ, one has:

$$|\dot{W}_{pol}| = \dot{m}\,|w_{pol}| = -\dot{m}\int_1^2 \frac{\mathrm{d}p_t}{\rho_t} \approx \frac{\dot{m}}{\rho_t}\,(p_{t1} - p_{t2}) \tag{2.18}$$

$$\dot{W}_{lost} = \dot{m}\,w_{lost} = \dot{m}\int_1^2 T_t \mathrm{d}s \approx \dot{m}T_{t,ref}\,(s_2 - s_1) \tag{2.19}$$

$$|\dot{W}| = \dot{m}\,|w| = -\dot{m}\int_1^2 \mathrm{d}h_t = \dot{m}c_p\,(T_{t1} - T_{t2}) = \mathcal{T}\Omega \tag{2.20}$$

In addition, the lost work can be written in terms of the entropy generated inside the domain, following Gauss' divergence theorem [82]:

$$\dot{m}T_{t,ref}(s_2 - s_1) = T_{t,ref}\int_{CV} \rho\sigma\,\mathrm{d}\mathcal{V} = T_{t,ref}\dot{S}_G \tag{2.21}$$

where $\sigma = \mathrm{d}s_{\mathcal{V}}/\mathrm{d}t$ represents the entropy generation rate per unit mass, and CV a control volume enclosing the turbine.

By considering Eqns. (2.14), (2.18), (2.19) and (2.20) and the definitions of first- and second-law efficiencies, Eqns. (2.3) and (2.7), it follows that:

$$\eta^{II} = \frac{\mathcal{T}\Omega}{\mathcal{T}\Omega + T_{t,ref}\dot{S}_G} \approx \frac{\mathcal{T}\Omega}{\Delta p_t Q} = \eta_{tt} \tag{2.22}$$

Equation (2.22) is a direct consequence of the equivalence of polytropic and isentropic work for a low pressure ratio process.

2.3 Losses in the Wells turbine

In order to identify the loss components that affect the efficiency of a Wells turbine, it can be useful to consider the expansion through the rotor as represented on the enthalpy-entropy (h - s) diagram in Fig. 2.2.

Subscript t denotes total conditions, s refers to isentropic conditions, t, rel are the total conditions in the relative frame and C and W are absolute and relative flow velocity, respectively. Considering the available energy for the expansion in a turbine $h_{1t} - h_{2s}$, corresponding to the isentropic expansion $1_t \rightarrow 2_s$, and the

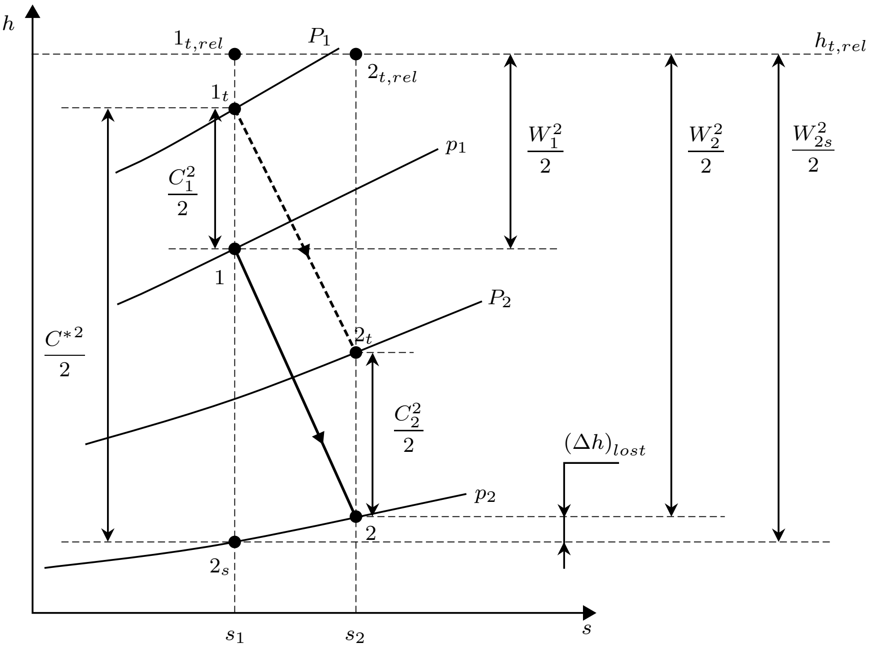

Figure 2.2: Expansion through the Wells rotor in the $h-s$ diagram.

useful work $h_{1t}-h_{2t}$, represented by the real expansion $1_t \rightarrow 2_t$, the *total-to-static* efficiency, see Eqn. (2.5), can be defined as follows:

$$\eta_{ts} = \frac{h_{1t}-h_{2t}}{h_{1t}-h_{2s}} = 1 - \frac{C_2^2/2}{h_{1t}-h_{2s}} - \frac{(\Delta h)_{lost}}{h_{1t}-h_{2s}} = 1 - \xi_{EX} - \xi_R \tag{2.23}$$

where ξ_R and ξ_{EX} are the loss coefficients related to the profile aerodynamics and exit kinetic energy, respectively. The isentropic expansion between total inlet conditions 1_t and static outlet conditions 2_s, allow to introduce a fictitious velocity C^*, as shown in Fig. 2.2. It can be practically calculated from global measurements as shown in Eqn. (2.24), by assuming air density constant at the value of the inlet conditions, i.e. $\rho = \rho_1 = const.$

$$\frac{C^{*2}}{2} = h_{t1} - h_{2s} = -\int_{t_1}^{2} \frac{\mathrm{d}p}{\rho} \approx \frac{\Delta p}{\rho} + \frac{C_1^2}{2} \tag{2.24}$$

Also, the loss of enthalpy $(\Delta h)_{lost}$ can be expressed in terms of relative velocities:

$$(\Delta h)_{lost} = h_2 - h_{2s} = \frac{W_{2s}^2 - W_2^2}{2} = \frac{W_{2s}^2}{2}\left(1-\psi^2\right) \tag{2.25}$$

where $\psi = W_2/W_{2s}$ is the reduction coefficient of the relative velocity and it is an useful measure of the aerodynamic efficiency of the rotor. (The relative velocity W_{2s} can be obtained taking into account that from the $h-s$ diagram, $W_{2s}^2/2 = W_1^2/2 + C^{*2}/2 - C_1^2/2 = U^2/2 + C^{*2}/2)$. Then, the rotor losses ξ_R can be rewritten based on Eqn. (2.25), introducing the velocity coefficient $\lambda = U/C^*$, where U is the peripheral speed of the rotor:

$$\xi_R = \frac{(\Delta h)_{lost}}{h_{1t} - h_{2s}} = \left(1 - \psi^2\right)\left(\frac{W_{2s}}{U}\right)^2 \lambda^2 \tag{2.26}$$

Generic velocity triangles at inlet and outlet of the Wells rotor, as reported in Fig. 2.3, are helpful to express ξ_R as a function of flow angles, rather than velocities.

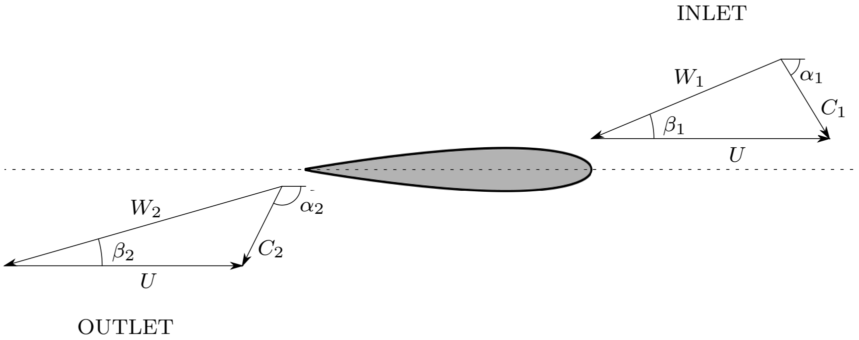

Figure 2.3: Velocity triangles at inlet and outlet of a Wells turbine.

$$\xi_R = \left(1 - \psi^2\right)\left(1 + \lambda^2 - 2\phi\lambda^2 \cot\alpha_1\right) \tag{2.27}$$

where the flow coefficient ϕ can be derived from the velocity inlet triangle in Fig. 2.3, i.e. $\phi = (C_1 \sin\alpha_1)/U$.

Following the same approach, it is possible to derive a similar expression for the exit losses ξ_{EX}:

$$\begin{aligned}\xi_{EX} = \frac{C_2^2/2}{h_{1t} - h_{2s}} &= \lambda^2 + \psi^2\left(1 + \lambda^2 - 2\lambda^2\phi\cot\alpha_1\right) \\ &\quad - 2\psi\lambda\cos\beta_2\left(1 + \lambda^2 - 2\lambda^2\phi\cot\alpha_1\right)^{1/2}\end{aligned} \tag{2.28}$$

where β_2 is the exit relative velocity angle.

Finally, the *total-to-static* efficiency can be expressed as a function of the flow angles α_1 and β_2 and of the non-dimensional parameters λ, ψ and ϕ:

$$\eta_{ts} = 2\lambda^2\left[\phi\cot\alpha_1 - 1 + \frac{\psi\cos\beta_2}{\lambda}\left(\lambda^2 + 1 - 2\lambda^2\phi\cot\alpha_1\right)^{1/2}\right] \tag{2.29}$$

The expressions for efficiency, Eqn. (2.29), and loss coefficients, Eqns. (2.27) and (2.28), can be simplified assuming the inlet flow to be axial, i.e. $\alpha_1 = 90°$, as typical for a Wells turbine inside an OWC when the airflow comes from the atmosphere.

$$\left.\begin{aligned}\xi_R &= \left(1 - \psi^2\right)\left(1 + \lambda^2\right) \\ \xi_{EX} &= \lambda^2 + \psi^2\left(1 + \lambda^2\right) - 2\psi\lambda\cos\beta_2\sqrt{1 + \lambda^2} \\ \eta_{ts} &= 2\lambda\left(\psi\cos\beta_2\sqrt{1 + \lambda^2} - \lambda\right)\end{aligned}\right\}\ \textit{for}\ \ \alpha_1 = 90^\circ \tag{2.30}$$

From Eqn. (2.30), it is clear that rotor losses depends on λ and ψ, which are related to the operating conditions, while they are independent from the deviation angle β_2 which influences the discharge loss ξ_{EX}, instead. A demonstrative representation of efficiency decomposition as a function of the operating conditions is reported in Fig. 2.4, where the values of the velocity reduction coefficient ψ and the exit relative velocity angle β_2 have been assumed constant for every flow condition.

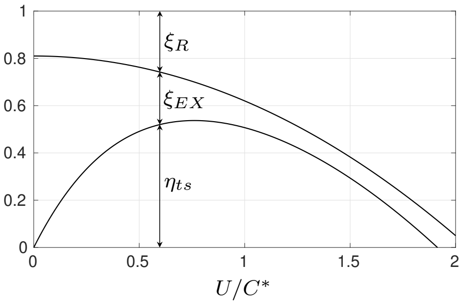

Figure 2.4: Losses components for efficiency evaluation ($\beta_2 = 10°$, $\psi = 0.9$).

The diagram in Fig. 2.4 shows the relative importance of the two losses as a function of the velocity coefficient U/C^*. This consideration becomes important because the Wells turbine works under variable flow conditions. In particular, the non stationary flow conditions determine continuous variation of the U/C^* parameter, which becomes higher than 1 when the mass flow rate decreases. Under these conditions, the losses ξ_{EX} are almost constant while the rotor losses considerably grow. In order to keep the efficiency as high as possible, it is necessary that the turbine works in the vicinity of the conditions for which U/C^* determines the maximum efficiency: due to the fact that C^* continuously changes, it becomes necessary to control the peripheral speed U. Maximum efficiency is obtained for the condition λ_{opt}, that can be analytically derived from Eqns. (2.29) and (2.30). In Eqn. (2.31) the inlet flow is assumed to be axial, i.e. $\alpha_1 = 90°$, and ψ constant for every flow condition. It follows:

$$\lambda_{opt} = \frac{\psi \cos\beta_2}{\left(1 - \psi^2 \cos^2\beta_2\right)^{1/2}} \tag{2.31}$$

2.4 Additional performance parameters

Aside the traditional performance parameters reported in Eqn. (2.1) and the efficiency definitions in Eqns. (2.2), (2.3) and (2.5), it is useful to introduce two additional non-dimensional parameters that can help to characterize the local and global performance of the Wells turbine. The first parameter is the reduction coefficient of the relative velocity, ψ, yet introduced in the present analyses. It should be note that ψ is directly related to a typical performance parameter used in turbine analyses, i.e. the *relative total pressure loss* coefficient Y_P defined in [113] as follows:

$$Y_P = \frac{p_{t1,rel} - p_{t2,rel}}{{}^1\!/_2 \rho_2 W_2^2} \tag{2.32}$$

It is a measure of the aerodynamic losses through the rotor [107] and it can be related to ψ by considering the transformations in the diagram of Fig. 2.2. Since points $1_{t,rel}$ and 2_s lie on an isentropic line, as for points $2_{t,rel}$ and 2, by applying Gibbs' equation and assuming the flow to be incompressible, it is possible to write:

$$\begin{cases} h_{t1,rel} - h_{2s} = \dfrac{p_{t1,rel} - p_2}{\rho} \\ h_{t2,rel} - h_2 = \dfrac{p_{t2,rel} - p_2}{\rho} \end{cases} \tag{2.33}$$

where the *rothalpy* is preserved during the transformation through a rotor [107] and it can be calculated as follows:

$$h_{t,rel} = h + \frac{W^2}{2} - \frac{U^2}{2} = const \implies \begin{cases} h_{t1,rel} = h_{2s} + \dfrac{W_{2s}^2}{2} - \dfrac{U^2}{2} \\ h_{t2,rel} = h_2 + \dfrac{W_2^2}{2} - \dfrac{U^2}{2} \end{cases} \tag{2.34}$$

Finally, by combining Eqns. (2.33) and (2.34), the *relative total pressure loss* coefficient reads:

$$Y_P = \frac{W_{2,s}^2 - W_2^2}{W_2^2} = \frac{1}{\psi^2} - 1 \tag{2.35}$$

The second useful parameter is the work coefficient Λ, which represents a dimensionless index of the specific work l:

$$\Lambda = \frac{l}{U_{tip}^2} = \frac{U\left(C_{1\theta} - C_{2\theta}\right)}{U_{tip}^2} \tag{2.36}$$

where subscript θ denotes the tangential component of the absolute velocity C.

Chapter 3

Turbine efficiency calculation by means of CFD

In this chapter, the different efficiency definitions presented in Ch. 2 have been compared by means of CFD simulations. They have been conducted on the well known case study proposed by Setoguchi *et al.* [1] which have been extensively investigated both numerically and experimentally.

In the first part, the method for entropy calculation from CFD simulations has been described, with particular emphasis on the decomposition of the generated entropy into a contribution due to the mean flow and another one due to the turbulent fluctuations. The use of the RANS approach to calculate entropy has been described and different turbulence closure methods have been proposed to solved it. The mid part presents the case study used for the analyses, and its verification and validation is described in detail. Then, two sets of comparisons have been proposed:

1. different turbulence closure models, typically used in Wells turbine analyses, have been tested in order to characterize them for turbine performance calculation, entropy production evaluation and stall prediction,

2. several rotors with different solidity and blade profiles thicknesses have been simulating in order to characterize their performance both with first- and second-law approach.

Finally, some important remarks have been resumed.

List of symbols

	Acronyms
CFD	computational fluid dynamics
CFL	Courant-Friedrichs-Lewy number
CV	control volume
LE	leading edge
NS	Navier-Stokes
PS	pressure side

RANS	Renynolds-averaged Navier-Stokes
REAL	realizable
S-A	Spalart-Allmaras
SS	suction side
SST	shear-stress transport
STD	standard
TE	trailing edge
	Non-dimensional properties
η	efficiency
f_{v1}	viscous damping function
I	identity tensor
$K_{\dot{S}}$	entropy generation/dissipation rate
p^*	static pressure drop coefficient
p_t^*	static pressure drop coefficient
ϕ	flow coefficient
Re	Reynolds' number
$\mathcal{T}^*$	torque coefficient
	Dimensional properties
c_p	specific heat at constant pressure
ε	rate of dissipation of k
E	energy, exergy
h	enthalpy
k	turbulent kinetic energy
λ	thermal conductivity
λ	volume viscosity
$\dot{m}$	mass flow rate
μ	dynamic viscosity
ν	kinematic viscosity
ω	specific dissipation rate
Ω	angular rotational frequency
p	pressure
$\mathbf{\Pi}$	stress tensor
Q	volumetric flow rate
r	turbine radius
ρ	air density
$\dot{S}_G$	entropy generation rate
σ	entropy generation rate per unit mass
T	temperature
t	time
$\mathcal{T}$	torque
$\mathcal{V}$	volume
T_w	wave period, piston period
U	peripheral rotor speed, blade speed
V	velocity
$\mathcal{V}$	volume
	Operators
∇	nabla operator
∇^2	laplacian operator
∇^S	sum of gradient and gradient transposed
$\overline{(\,)}$	mean value, time average
	Subscripts and superscripts
$'$	fluctuating component
d	dissipation
g	production
hub	turbine hub
II	second-law approach
in	input
ind	indirect
mf	mean flow
out	output
R	Reynolds'

ref	reference value
t	total condition
T	turbulent
tip	turbine tip
tt	total-to-total
ts	total-to-static
V	due to fluid flow

3.1 Entropy calculation from CFD (RANS) simulations

The quantities required to estimate the efficiency of a Wells turbine can be calculated using numerical simulations, i.e. by solving the governing Navier-Stokes (NS) equations numerically. These quantities include the turbine torque $\mathcal{T}$, the static and total pressure drops Δp and Δp_t, the volumetric flow rate Q, and the entropy generation rate $\dot{S}_G$.

As a Direct Numerical Simulation (DNS) of the NS equations for most flows of industrial interest is still beyond the capability of current computers, the most common and practical approach is the solution of the Reynolds Averaged Navier-Stokes (RANS) equations, which are derived by replacing the instantaneous flow variables in the NS with the sum of a mean value and a fluctuating component with zero mean value ($\varphi = \overline{\varphi} + \varphi'$).

For a compressible flow, assuming negligible heat transfer as common in turbomachinery applications, the RANS equations of conservation of mass, momentum and energy read as follows [114]:

$$\begin{cases} \dfrac{\partial \overline{\rho}}{\partial t} + \nabla \cdot \left(\overline{\rho} \overline{\mathbf{V}} \right) = 0 \\ \dfrac{\partial \overline{\rho} \overline{\mathbf{V}}}{\partial t} + \nabla \cdot \left(\overline{\rho} \overline{\mathbf{V}} \otimes \overline{\mathbf{V}} + \overline{\rho} \overline{\mathbf{V}' \otimes \mathbf{V}'} \right) = -\nabla \overline{p} + \nabla \cdot \overline{\mathbf{\Pi}} \\ \dfrac{\partial \overline{\rho} \overline{h}}{\partial t} + \nabla \cdot \left(\overline{\rho} \overline{\mathbf{V}}\, \overline{h} \right) = \dfrac{D \overline{p}}{Dt} + \overline{\mathbf{\Pi}} : \nabla \overline{\mathbf{V}} + \overline{\mathbf{\Pi}' : \nabla \mathbf{V}'} \end{cases} \tag{3.1}$$

where $\mathbf{V}$ is the velocity vector, h is the static enthalpy, and $\mathbf{\Pi}$ is the deviatoric stress tensor, that for a Newtonian flow can be expressed as the sum of the contributions due to the strain rate tensor $\nabla^S \mathbf{V}$ and the volumetric tensor $(\nabla \cdot \mathbf{V}) \mathbf{I}$, each one multiplied by a constant, i.e. the molecular viscosity μ and the bulk viscosity λ, respectively.

$$\mathbf{\Pi} = \mu \left(\nabla \mathbf{V} + \nabla \mathbf{V}^T \right) + \lambda \left(\nabla\, \mathbf{V} \right) \mathbf{I} = 2 \mu \nabla^S \mathbf{V} + \lambda \left(\nabla \cdot \mathbf{V} \right) \mathbf{I} \tag{3.2}$$

In Eqn. (3.1), the prime symbol denotes fluctuating quantities, and the overbar denotes time-averaged flow quantities. Density fluctuations, i.e. ρ', have been neglected as they start to affect turbulence around a Mach number of 1 [115]. In the presence of significant density fluctuations, the Favre-averaged NS equations can be used instead [116].

The terms which represent the effects of turbulent fluctuations on the mean flow are not resolved by the RANS approach and need to be modeled to allow the solution of the system of equations. The turbine torque $\mathcal{T}$ can then be calculated by integrating pressure and viscous stresses on the turbine blade, while the pressure drops require the evaluation of the (mass-flow) averaged pressure on surfaces appropriately defined upstream and downstream of the turbine. The evaluation of the entropy generation rate $\dot{S}_G$ requires more attention, as an entropy equation is not generally solved in CFD programs, as it would make the system of equations in Eqn. (3.1) overdetermined. An entropy equation can be derived by linking Gibbs' relation with the momentum and energy equations, as described in [82, 117]:

$$\frac{\partial \overline{\rho}\,\overline{s}}{\partial t} + \nabla \cdot \left(\overline{\rho}\overline{\mathbf{V}}\overline{s}\right) + \nabla \cdot \left(\overline{\rho}\overline{\mathbf{V}'s'}\right) = \overline{\rho}\sigma_{V,mf} + \overline{\rho}\,\overline{\sigma_{V,T}} \tag{3.3}$$

where the right hand side represents the entropy production rate per unit mass due to fluid flow: in particular, $\sigma_{V,mf}$ is the contribution due to the mean flow and $\overline{\sigma_{V,T}}$ is the one due to turbulent fluctuations. The two terms on the right hand side of Eqn. (3.3) are defined as follows, neglecting the effect of temperature fluctuations on viscous entropy production as in [117, 118]:

$$\overline{\rho}\,\sigma_{V,mf} = \frac{1}{\overline{T}}\left(\overline{\mathbf{\Pi}} : \nabla\overline{\mathbf{V}}\right) \tag{3.4}$$

$$\overline{\rho}\,\overline{\sigma_{V,T}} = \frac{1}{\overline{T}}\left(\overline{\mathbf{\Pi}' : \nabla\mathbf{V}'}\right) \tag{3.5}$$

Only the terms containing mean quantities are solved (and hence available) in a RANS approach. All terms involving fluctuating quantities ($\overline{\rho}\overline{\mathbf{V}'\otimes\mathbf{V}'}$ and $\overline{\mathbf{\Pi}' : \nabla\mathbf{V}'}$) need to be modeled. The most common approaches are Linear Eddy Viscosity models, based on the so-called Boussinesq's hypothesis:

$$-\overline{\rho}\overline{\mathbf{V}'\otimes\mathbf{V}'} = \mathbf{\Pi}_R = \mu_T\left(\nabla\overline{\mathbf{V}} + \nabla\overline{\mathbf{V}}^T\right) - \frac{2}{3}\overline{\rho}k\mathbf{I} = 2\mu_T\nabla^S\overline{\mathbf{V}} - \frac{2}{3}\overline{\rho}k\mathbf{I} \tag{3.6}$$

where $\mathbf{\Pi}_R$ is the Reynolds' stress tensor, μ_T is the turbulent viscosity and k is the turbulent kinetic energy per unit mass ($k = \frac{1}{2}(-\overline{\rho}\overline{u'^2} - \overline{\rho}\overline{v'^2} - \overline{\rho}\overline{w'^2})$). The term μ_t is usually modeled adding additional transport equations. The quantity $\left(\overline{\mathbf{\Pi}' : \nabla\mathbf{V}'}\right)$ represents the dissipation of turbulent kinetic energy into heat and is usually referred to with the symbol ε. Finally, the global entropy generation per unit time ($\dot{S}_G$) can be estimated by integrating the viscous dissipation in the domain of interest:

$$\dot{S}_G = \int_{CV} \overline{\rho}\left(\sigma_{V,mf} + \overline{\sigma_{V,T}}\right) d\mathcal{V} \tag{3.7}$$

This approach for the calculation of entropy production is referred to as a *direct* method in [117]. Alternatively, the same authors suggested the use of an *indirect* method, which is derived from the equation of conservation of entropy (Eqn. (3.3)), neglecting turbulent convection and diffusion across the boundaries, and integrating in an appropriate control volume CV.

$$\dot{S}_G \approx \int_A \overline{\rho}\,\overline{s}\,\overline{\mathbf{V}} \cdot \mathbf{n} dA + \frac{\partial}{\partial t} \int_{CV} \overline{\rho}\,\overline{s} d\mathcal{V} \tag{3.8}$$

In Eqn. (3.8), A represents the boundary of the control volume CV, and s the specific entropy which can be evaluated under the assumption of ideal gas, as recalled in Sec. 2.2.1.

3.1.1 Evaluation of entropy production with different turbulence models

As mentioned in the previous section, turbulent quantities are not directly available in RANS approaches and need to be modeled. Different turbulence closure methods are available in CFD solvers, the most common being the ones based on the so-called Boussinesq's hypothesis, which assumes a linear dependency between Reynolds' stress and strain tensors (Eqn. (3.6)). The most famous ones are $k - \varepsilon$ and $k - \omega$ models, which derive the turbulent viscosity μ_T based on two additional partial differential equations, for turbulent kinetic energy (k) and its rate of dissipation (ε), and for k and its specific dissipation rate (ω), respectively. Of particular interest for this work is the equation of conservation for the turbulent kinetic energy, which is reported in Eqn. (3.9):

$$\begin{aligned} \frac{\partial \overline{\rho} k}{\partial t} + \nabla \cdot \left(\overline{\rho} k \overline{\mathbf{V}}\right) = \nabla \cdot \left(-\overline{p' \mathbf{V}'} + \overline{\mathbf{\Pi}' \cdot \mathbf{V}'} - \frac{1}{2} \overline{\rho} \overline{\mathbf{V}' \cdot \mathbf{V}' \otimes \mathbf{V}'} \right) + \\ - \overline{\mathbf{\Pi}' : \nabla \mathbf{V}'} - \overline{\rho} \overline{\mathbf{V}' \otimes \mathbf{V}'} : \nabla^S \overline{\mathbf{V}} \end{aligned} \tag{3.9}$$

where the last two terms on the right hand side of the equation represent the rates of dissipation and production of k, respectively. The former, referred to with the symbol ε, is present also in the energy equation (Eqn. (3.1)), as the dissipated turbulent kinetic energy is transformed into heat. The production of k can be expressed following the Boussinesq's hypothesis in Eqn. (3.6):

$$\overline{\mathbf{\Pi}' : \nabla \mathbf{V}'} = \overline{\rho} \varepsilon \tag{3.10}$$

$$-\overline{\rho} \overline{\mathbf{V}' \otimes \mathbf{V}'} : \nabla^S \overline{\mathbf{V}} = 2 \mu_T \left(\nabla^S \overline{\mathbf{V}}\right)^2 - \frac{2}{3} \overline{\rho} k \left(\nabla \cdot \overline{\mathbf{V}}\right) \tag{3.11}$$

Using Eqn. (3.10), the viscous dissipation in Eqn. (3.4) and (3.5) can be calculated as follows:

$$\begin{aligned} \overline{T} \overline{\sigma_V} = \overline{T} \sigma_{V,mf} + \overline{T} \overline{\sigma_{V,T}} = \frac{1}{\overline{\rho}} \left(\overline{\mathbf{\Pi}} : \nabla \overline{\mathbf{V}} + \overline{\mathbf{\Pi}' : \nabla \mathbf{V}'} \right) = \\ = \frac{1}{\overline{\rho}} \left(2 \mu \left(\nabla^S \overline{\mathbf{V}}\right)^2 + \lambda \left(\nabla \cdot \overline{\mathbf{V}}\right)^2 + \overline{\rho} \varepsilon \right) \end{aligned} \tag{3.12}$$

Many authors [119–121], assuming a local equilibrium between turbulent entropy production and dissipation, i.e. $\overline{\rho}\varepsilon = 2\mu_T\left(\nabla^S\overline{\mathbf{V}}\right)^2 - \frac{2}{3}\overline{\rho}k\left(\nabla\cdot\overline{\mathbf{V}}\right)$, introduce the following approximation:

$$\overline{T\sigma_V} = \frac{1}{\overline{\rho}}\left[2\left(\mu+\mu_T\right)\left(\nabla^S\overline{\mathbf{V}}\right)^2 + \left(\lambda\nabla\cdot\overline{\mathbf{V}} - \frac{2}{3}\overline{\rho}k\right)\left(\nabla\cdot\overline{\mathbf{V}}\right)\right] \tag{3.13}$$

The last two expressions Eqns. (3.12) and (3.13)) are alternative methods for calculating the entropy production due to viscous dissipation per unit mass, and the choice between the two methodologies depends on the selected turbulence closure model:

1. In $k-\varepsilon$ and $k-\omega$ models, both approaches can be adopted because in the former ε is directly available, while in the latter it can be calculated as a function of the turbulent kinetic energy k and specific dissipation rate ω, i.e. $\varepsilon = \omega k\beta^*$, where β^* is a model constant which depends on the specific implementation. An important consideration has been proposed in [120], where the authors note that the second approach (Eqn. (3.12)) is more reliable, because in RANS approaches ε is only used as an intermediate quantity to calculate μ_t and $\mathbf{\Pi}_R$, which interact with the mean flow through the momentum and energy equations.

2. In Spalart-Allmaras (S-A) models only the second approach can be used, as the method solves directly a transport equation for kinematic eddy viscosity $\tilde{\nu}$, which is related to μ_T through the following expressions:

$$\mu_T = \overline{\rho}\tilde{\nu}f_{v1} \qquad f_{v1} = \frac{\left(\tilde{\nu}/\nu\right)^3}{\left(\tilde{\nu}/\nu\right)^3 + C_{v1}^3} \tag{3.14}$$

where f_{v1} is the viscous damping function. In addition to the standard formulation of the $k-\varepsilon$ model, the Realizable (REAL) $k-\varepsilon$ formulation has also been considered. It is a newer implementation [122] that differs from the original for a new formulation of the turbulent viscosity and a new transport equation for the dissipation rate ε. The Fluent® User's Guide [123] states that the $k-\varepsilon$ REAL model provides superior performance for flows involving rotation, boundary layers under strong adverse pressure gradients, separation and recirculation.

3.2 Methodology

The turbine geometry and operating conditions simulated in this work are the ones presented in the experimental work from Setoguchi *et al.* [1]. The main details are summarized in Table 3.1.

The domain for the numerical simulations is reported in Figure 3.1 (a): it is a straight duct representing a single blade passage of the turbine, with periodic

Table 3.1: Geometric and operating data from [1].

Rotor tip diameter	300 mm
Rotor hub diameter	210 mm
Tip clearance	1 mm
Chord length	90 mm
Sweep ratio	0.417
Hub-to-tip ratio	0.7
Number of blades	5 - 6 - 7
Airfoil profile	NACA 0012 - NACA 0015 NACA 0020
Solidity	0.56 - 0.67 - 0.78
Rotational speed	2500 rpm
Operating frequency	1/6 Hz
Non-dimensional frequency $(\pi f c)/U$	1.2×10^{-3}
Reynolds' number based on blade chord	$\approx 2\times10^5$

boundary conditions at the 2 sides. Simulating a single passage of a turbomachinery's blade row (or even multiple single passages from different blade rows, with an appropriate treatment of the inter-row interface) is a common practice in turbomachinery RANS simulations [124–126] when the hypothesis of periodic flow with respect to the blade pitch is valid, i.e. in the absence of flow structures larger than the blade pitch. This approximation has been often used in Wells turbine simulations [65, 67, 88, 92]. A comparison between the simulation of the Wells turbine's full rotor and of a single passage was conducted by the authors, showing a maximum difference in the performance coefficients of less than 0.1%. The interaction between stationary and moving parts has been modeled using a "frozen rotor approach", also referred to as the "multiple reference frame" (MRF) model in the Fluent User's Guide [123]. The model can be used for turbomachinery applications in which rotor-stator interaction is relatively weak, and the flow is relatively uncomplicated at the interface between the moving and stationary zones. This seems to be a good approximation for the present case study, where the interaction between moving parts is only at the hub and casing of the duct where the turbine is housed. The same model has been used in the majority of previous CFD analyses of Wells turbines [65, 76, 88, 89, 100, 127, 128]. The OWC chamber is not included in the domain (as done for example in [129–131]), because its main effect is to cause a delay between the movement of the water level in the chamber and the mass-flow in the turbine duct, without significant modifications to the turbine performance.

Uniform inlet boundary conditions have been used for velocity, total temperature

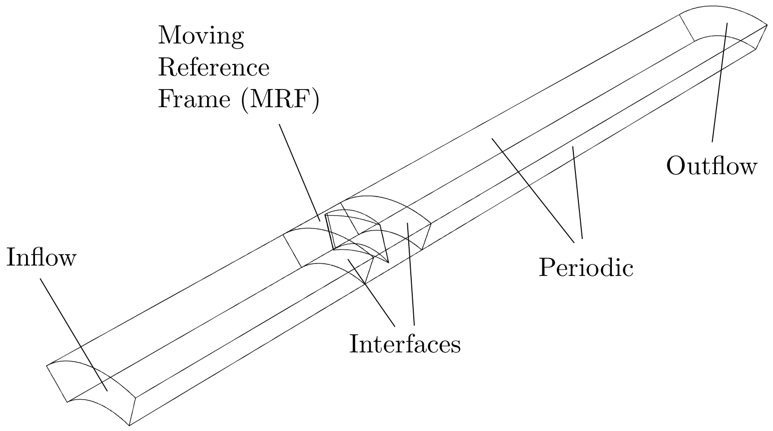

(a) Computational domain for simulations

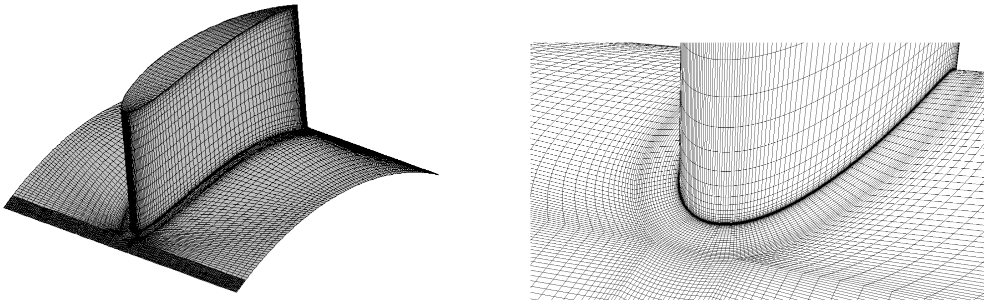

(b) Blade mesh

(c) Close-up view of the hub mesh

Figure 3.1: Computational domain and details of the mesh (about 2 million cells) used for simulations.

and turbulent quantities. The velocity has been set to a value, fixed in steady (fixed-ϕ) simulations and sinusoidally variable in time in dynamic simulations, chosen to obtain the required value or range of flow coefficients (see Eqn. (2.1)). Figure 3.2 shows a typical variation of flow coefficient ϕ, where T_w represents the wave period. The inlet total temperature has been set to 288 K and the turbulent quantities are calculated by the solver based on the values set for turbulent intensity and length scale (2% and 7% of the blade height, as suggested in [123]). A uniform value of static pressure has been specified at the outlet, while periodic boundary conditions have been used at the two sides of the passage of the computational domain (Fig. 3.1). Inlet and outlet are inverted for negative values of the flow coefficient. A multi-block structured grid has been used to discretize the volume, with a C-grid around the blade able to capture the boundary layer flow and an H-grid in the rest of domain, see Figs. 3.1 (b) and (c).

Four different turbulence closure models have been compared: the $k-\omega$ SST, the standard (STD) and realizable (REAL) $k-\varepsilon$ and the Spalart-Allmaras (S-A) model. Numerical simulations have been conducted using the commercial CFD software

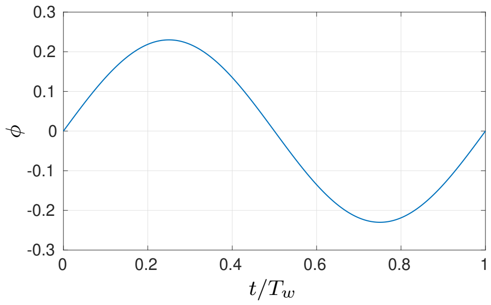

Figure 3.2: Inlet boundary condition for dynamic simulations, in terms of flow coefficient ϕ.

Ansys Fluent® 17.0. The SIMPLEC algorithm has been used for the pressure-velocity coupling (pressure-based segregated algorithm [115, 123]), a second-order centered scheme for pressure and viscous terms and a second-order upwind scheme for convective terms. Multiple-reference-frames have been adopted to simulate the interaction between stationary and rotating volumes. Steady (fixed-ϕ) simulations have been run with a time-dependent approach (and constant boundary condition) with a time step of 10^{-4} until convergence of the monitored quantities (torque and pressure drops) were obtained (within 0.1% in the last 1000 time steps), while time dependent simulations were run for 3 wave periods, with a time step sufficient to obtain results independent from the temporal discretization. Results from the last 2 periods differed always by less than 0.1%, hence periodic convergence has been considered achieved. A first-order implicit temporal discretization approach was used, with 5 sub-iterations per time step. The default settings of Ansys Fluent® have been maintained: at every sub-iteration, 2 sweeps of the algebraic multigrid with a maximum of 40 levels are allowed, with the Gauss-Seidel smoother. An explicit convergence criterion was not set in time-dependent simulations, but rather the number of sub-iterations was kept fixed, and the time step size reduced until results were independent from its value. Maximum residuals were found to be of the order of 10^{-4} for appropriate values of the time step. Increasing the number of sub-iterations would have achieved the same effect, at least to a certain time step size, as shown in [132]. As demonstrated in [132], the effect of the discretization order is negligible;. The error introduced at each time-step, which for an implicit method is the sum of temporal discretization and iterative errors [133], appears to be dominated by the latter.

All simulations were run on dual processor 3.30 GHz 8 core Intel Xeon E5-2667 v2 CPUs. Each time step required about 3 seconds, and complete periodic simulations required as long as 3 months.

3.2.1 Verification and validation

The choice of the spatial discretization has been made following a grid convergence study, with the $k-\omega$ model for turbulence closure, following the guidelines given in the JFE Editorials Policy Statement [134] and expanded in several articles [135,136]. These are based on the use of the Richardson Extrapolation, which involves the solution of the numerical problem on 3 grids with increasing size. Defining h_1, h_2 and h_3 the representative grid dimensions (these can be calculated as $(V/N)^{1/3}$, with V the volume of the fluid domain, and N the number of cells), and S_1, S_2 and S_3 the solutions obtained with the 3 grids for a quantity of interest, the apparent order of convergence can be calculated as follows:

$$p = \frac{1}{\log(r_{23})} |\log(|\epsilon_{12}/\epsilon_{23}|)| + \log\left(\frac{r_{12}^p - s}{r_{23}^p - s}\right) \tag{3.15}$$

where $s = sign(\epsilon_{12}/\epsilon_{23})$, $\epsilon_{ij} = (S_i - S_j)$ is the difference between the solution obtained with 2 grids of different sizes, and $r_{ij} = h_i/h_j$ the ratio of grid representative sizes. If $s > 0$ the convergence is monotonic, while $s < 0$ might be an indication of oscillatory convergence. A negative value for p might be an indicator of divergence (or that the grids do not lie within the asymptotic range). The asimptotic value can be estimated as follows:

$$S_{ext} = \frac{r_{23}^p S_3 - S_2}{r_{23}^p - 1} \tag{3.16}$$

Regarding the uncertainty linked to the evaluation, [136] suggests using a grid convergence index GCI defined as follows:

$$GCI_j = 1.25 \left| \frac{S_{ext} - S_j}{S_{ext}} \right| \tag{3.17}$$

while [135], in the presence of oscillatory convergence, suggest using half the range of variability in the data:

$$U_{Stern} = \frac{1}{2} |max(S_j) - min(S_j)| \tag{3.18}$$

Figure 3.3 presents the convergence of p^* and T^* for a flow coefficient $\phi = 0.16$, using 5 grids with different number of cells (each grid has about 2.9 times the cells of the previous one), the central (grid C) being the one that has been used for the rest of the calculations.

It is clear that none of the grids presents a large variation with respect to the finest one (the maximum deviation is less than 1.5% on the coarsest grid for the pressure drop coefficient). The grid used in this study, which has about 2 million cells, produces results that are extremely close to the ones obtained with the finest grid (17 million cells), producing errors of less than 0.3% and 0.05% of the most accurate prediction, for p^* and $\mathcal{T}^*$, respectively. It is interesting to note how, while the

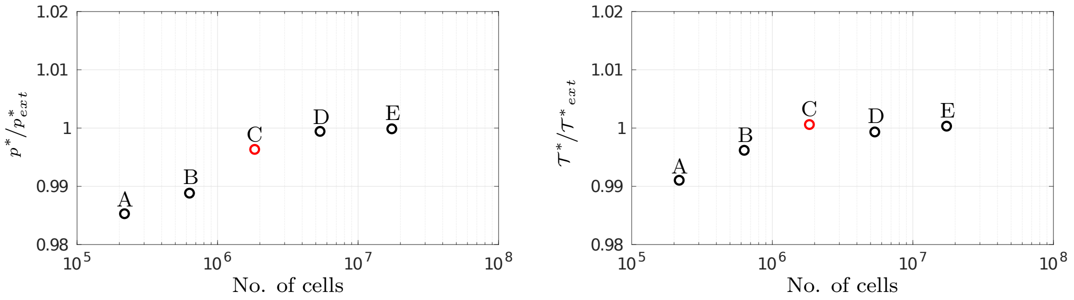

(a) Static pressure drop coefficient (b) Torque coefficient

Figure 3.3: Grid convergence analysis of non-dimensional parameters evaluated with five grid sizes.

pressure drop coefficient exhibits a monotonic convergence, the torque coefficients' convergence is oscillatory. Tables 3.2 and 3.3 present the evaluation of apparent convergence error and evaluation uncertainties, for 2 sets of grid triplets (B-C-D and C-D-E, respectively). The apparent convergence order calculated with the first set of grids is similar to the theoretical order of the method, which suggests that this grids are in the asymptotic convergence range. The value obtained with the last set of grids suggests that mesh independence has being reached.

Table 3.2: Grid convergence estimation using grids B, C, D.

	p^*	T^*
$N_1 = N_B$	631 200	
$N_2 = N_C$	1 836 480	
$N_3 = N_D$	5 360 165	
r_{12}	1.43	
r_{23}	1.43	
S_1/S_{ext}	0.9874	0.9963
S_2/S_{ext}	0.9950	1.0006
S_3/S_{ext}	0.9980	0.9994
p	2.57	3.62
GCI_1	1.048%	0.180%
GCI_2	0.420%	0.029%
GCI_3	0.168%	0.029%
U_{Stern}	–	0.220%

The validation has been conducted on the selected grid, i.e. grid C, which has non-dimensional wall distance (y^+) below unity (so that the $k-\varepsilon$ model was used for the enhanced wall treatment [123]). Figure 3.4 reports the results obtained for the

Table 3.3: Grid convergence estimation using grids C, D, E.

	p^*	T^*
$N_1 = N_C$	1 836 480	
$N_2 = N_D$	5 360 165	
$N_3 = N_E$	17 376 540	
r_{12}	1.43	
r_{23}	1.43	
S_1/S_{ext}	0.9964	1.0006
S_2/S_{ext}	0.9995	0.9994
S_3/S_{ext}	0.9999	1.0003
p	5.37	0.69
GCI_1	0.062%	0.244%
GCI_2	0.009%	0.244%
GCI_3	0.001%	0.133%
U_{Stern}	–	0.061%

non-dimensional coefficients of torque and pressure drop for steady calculations at different flow coefficients, for the turbine with the highest number of blades ($z = 7$, i.e. with a rotor tip solidity equal to 0.67) and NACA0020 profile, where the largest gradients of flow quantities are expected, in comparison with experimental data. The latter present the famous hysteretic loop due to the capacitive effect of the OWC chamber [129, 131, 137]. Numerical results lie in the middle of the hysteresis loop, therefore attesting the appropriateness of the numerical results.

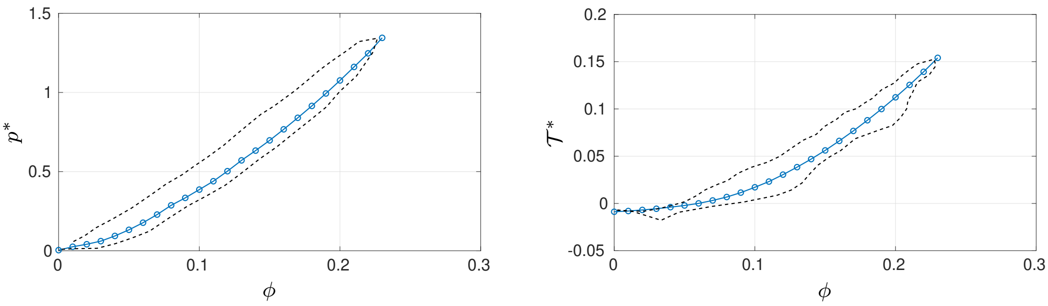

(a) Static pressure drop coefficient

(b) Torque coefficient

Figure 3.4: Validation of grid (C) with the experimental data (dotted line) from [1].

Figure 3.5 reports the effect of the time step size on the torque and the entropy generation coefficients. Five time step values have been compared running 3 periods of oscillation, with an amplitude for the sinusoidal inlet velocity appropriate to produce a maximum flow coefficient ϕ of 0.23, as in the experiment [1]. Only the last period is reported, for brevity.

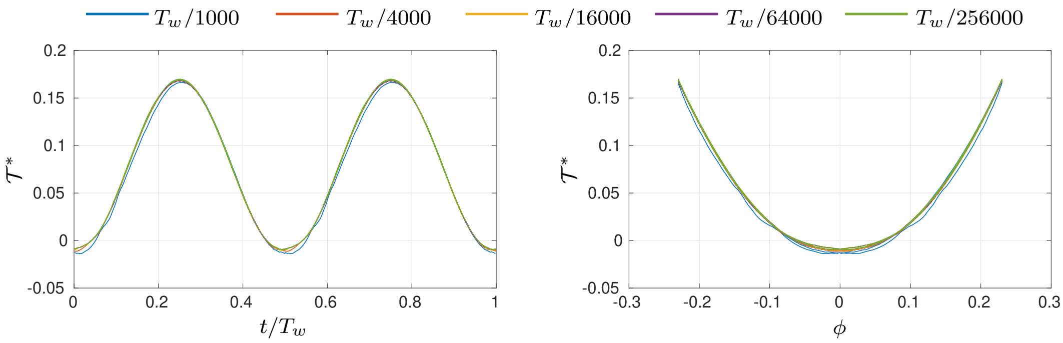

(a) Torque coefficient history (b) Torque coefficient vs flow coefficient

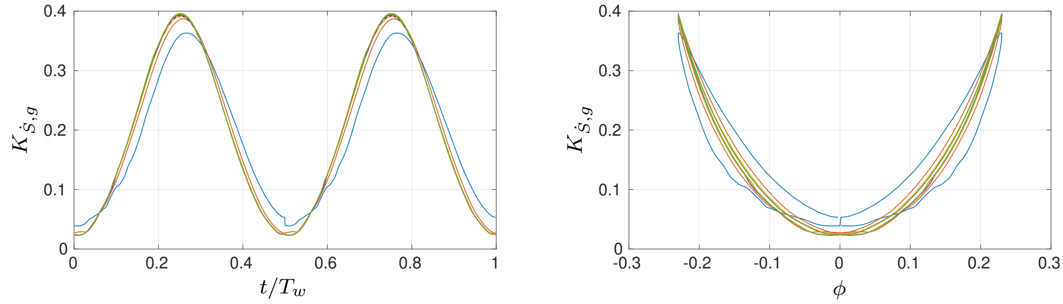

(c) Non-dimensional entropy generation history (d) Non-dimensional entropy production vs flow coefficient

Figure 3.5: Verification of the temporal discretization using five different time-step sizes, for a maximum flow coefficient $\phi_{max} = 0.23$.

The non-dimensional entropy generation has been evaluated using both the dissipation and the generation of turbulent kinetic energy (as explained in Section 3.1.1), and the results have been expressed in non-dimensional form, as follows:

$$K_{\dot{S},d} = \frac{\displaystyle\int_{CV} \left(2\mu\left(\nabla^S\overline{\mathbf{V}}\right)^2 + \lambda\left(\nabla\cdot\overline{\mathbf{V}}\right)^2 + \overline{\rho}\varepsilon\right) dV}{\frac{1}{2}\rho_{in}\Omega^3 r_{tip}^5} \tag{3.19}$$

$$K_{\dot{S},g} = \frac{\displaystyle\int_{CV} \left[2\left(\mu+\mu_T\right)\left(\nabla^S\overline{\mathbf{V}}\right)^2 + \left(\lambda\nabla\cdot\overline{\mathbf{V}} - \frac{2}{3}\overline{\rho}k\right)\left(\nabla\cdot\overline{\mathbf{V}}\right)\right] dV}{\frac{1}{2}\rho_{in}\Omega^3 r_{tip}^5} \tag{3.20}$$

where $K_{\dot{S},d}$ is the non-dimensional entropy production rate in the control volume, evaluated using the turbulent kinetic energy dissipation defined in Eqn. (3.12), and $K_{\dot{S},g}$ is the non-dimensional entropy production rate in the control volume, evaluated using the turbulent kinetic energy generation defined in Eqn. (3.13). It should be noted that in the presence of an incompressible flow, the second term in the round brackets of Eqn. (3.19) and the last term in the square brackets of Eqn. (3.20) are null. In the current analyses, given the low relative Mach number in the vicinity of the blade (about 0.3) these terms never accounted for more than 0.02% of the total entropy production. The flow has been treated as compressible for generality, as the derivation in the current form can be applied also for higher Mach number machines [138, 139].

The analysis highlights how time steps larger than $T_w/16000 \approx 4\times10^{-4}$ s produce spurious phase errors [134], which manifest in a false delay, previously erroneously interpreted as an aerodynamic hysteresis of the turbine [129,131,137,140]. This effect is reported in Figure 3.5, where it is evident how hysteretic effects disappear when sufficiently small time step sizes are used (below $T_w/16000 \approx 4 \times 10^{-4}$ s). Reducing the time-step size has a similar effect to increasing the number of sub-iterations: [132] have shown how it is the total number of sub-iterations per cycle (i.e number of time steps per cycle times number of sub-iterations per time step) that influences the temporal convergence. For the selected grid and working conditions, the maximum value of the Courant number (CFL) is proportional to the time step size and ranges from 6400 (for $dt = T_w/1000$) to 25 (for $dt = T_w/256000$). Performance during inflow (negative flow coefficients) and outflow (positive flow coefficients) does not present significant differences. The absence of dynamic effects is in agreement with the large literature on oscillating lifting surfaces [141–143], where significantly larger non-dimensional frequencies are required to produce an appreciable hysteresis [94, 144].

A similar analysis, Fig. 3.6, has been conducted in the presence of a temporal profile for the inlet velocity with a larger amplitude ($\phi_{max} = 0.325$), sufficient to lead to blade stall. The results of the analysis show how an even smaller temporal discretization is required to achieve results independent from the time step (about $1.25E-5$ s), with a corresponding value of the maximum CFL of about 12.5. In the presence of stall, a small hysteretic loop is present, which is caused by the fact that the boundary layer reattaches to the blade surface for a flow coefficient (and therefore an angle of attack) smaller than the one leading to stall during the acceleration phase. This phenomenon is not necessarily linked to the dynamic operating conditions, as a static stall hysteresis is documented for many lifting surfaces [145, 146], while significantly larger non-dimensional frequencies are required to produce appreciable effects on the performance [142, 143]. In any case, the value of the performance parameters after reattachment, during deceleration, is indistinguishable from the one attained during acceleration.

3.3 Comparison among different turbulence models

In this paragraph, simulations with different turbulence closure models are reported for the same rotor geometry, i.e. the rotor with 6 blades (rotor tip solidity equal to 0.57) and NACA0015 blade profile. Two periodic operating conditions have been

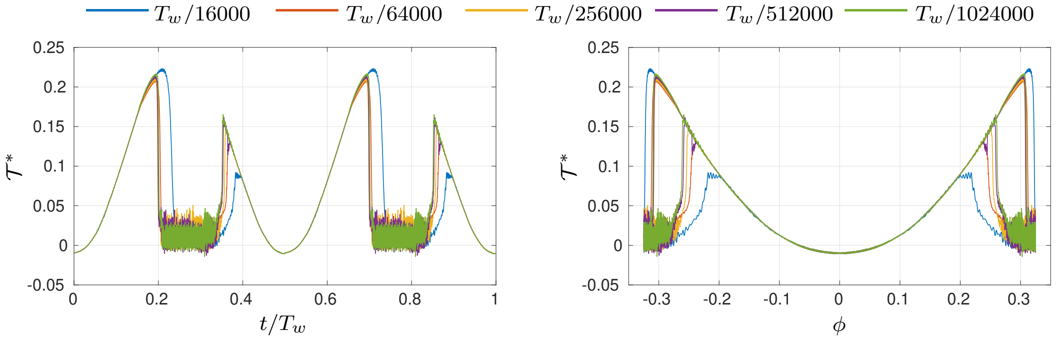

(a) Torque coefficient history (b) Torque coefficient vs flow coefficient

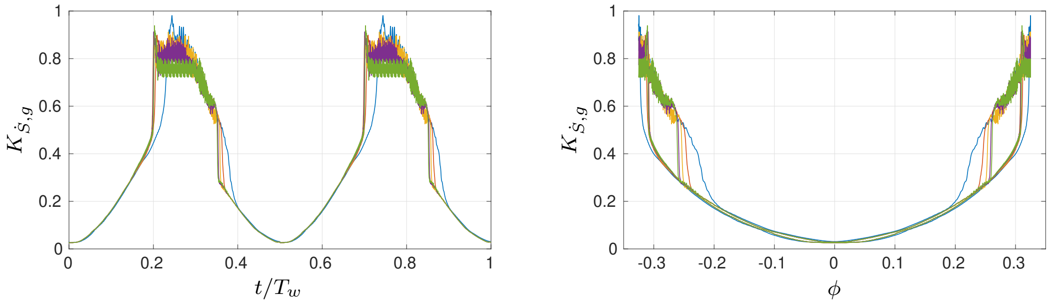

(c) Non-dimensional entropy generation history (d) Non-dimensional entropy production vs flow coefficient

Figure 3.6: Verification of the temporal discretization using five different time-step sizes, for a maximum flow coefficient $\phi_{max} = 0.325$.

simulated: one with a maximum flow coefficient $\phi_{max} = 0.23$, not sufficient to produce stall, and one with a $\phi_{max} = 0.345$, enough to cause deep stall of the rotor at least with some turbulence models.

3.3.1 Simulations for $\phi_{max} = 0.23$

Figure 3.7 reports the non-dimensional parameters commonly adopted in Wells turbines characterization with respect to the flow coefficient, as calculated in Eqn. (2.1). Positive values of the flow coefficient refer to the outflow, while negative ones refer to the inflow phase.

Using different turbulence models does not affect the prediction of the rotor performance and their estimated trends are substantially overlapping (see Fig. 3.7) and matching the experimental data as reported in Fig. 3.4. A small overprediction of the pressure coefficient, i.e. p^*, can be observed in the simulations made with the $k-\varepsilon$ models, while the comparison of $k-\omega$ and S-A does not highlight differences. The torque is well predicted by all models, and no significant differences can be observed.

On the contrary, the non-dimensional entropy generation, Fig. 3.7 (c), shows

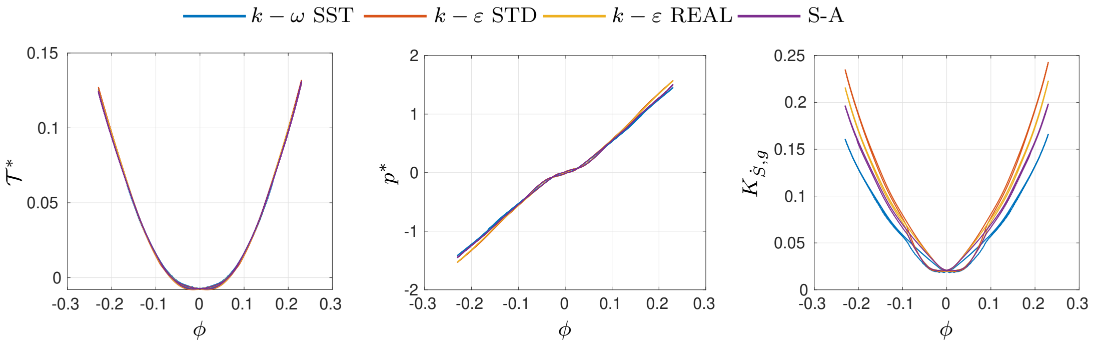

(a) Torque coefficient (b) Pressure drop coefficient (c) Non-dimensional entropy generation

Figure 3.7: Non-dimensional performance of the rotor with NACA0015 blade profile and 6 blades, as a function of the flow coefficient ϕ, estimated with different turbulent closure models.

different values depending on the turbulence model selected. In particular, $k-\varepsilon$ models estimate a higher entropy production with respect to the other models. In order to better understand these large differences, the entropy generation calculations have been reported in Fig. 3.8: the mean values over a cycle of both $K_{\dot{S},d}$ and $K_{\dot{S},g}$ (defined in Eqns. (3.19) and (3.20)) are reported, for two different control volumes, a smaller one going from half a chord upstream to half a chord downstream of the rotor (A), and a larger one enclosing all computational domain (B) (8 chords upstream and downstream of the rotor), as indicated in Fig 3.1 (a). The results from control volume A are reported in Fig. 3.8 (a), the results from control volume B are reported in Fig. 3.8 (b).

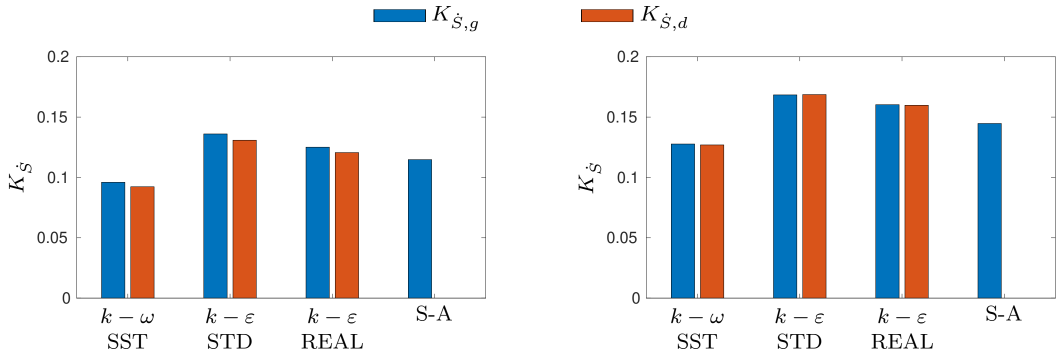

(a) Volume A (b) Volume B

Figure 3.8: Non-dimensional entropy production averaged on a cycle.

From the results presented in Fig. 3.8, the evaluation of the (non-dimensional) entropy production using the generation and dissipation of turbulent kinetic energy leads to the same results only if the calculation is made in a large enough control volume (control volume B), while an appreciable difference exists when the boundaries of the control volume are too close to the rotor (control volume A), mainly due to the neglection of the wake, where the turbulent energy dissipation is larger than its production. In the Spalart-Allmaras model, as explained in Section 3.1.1, only the production of turbulent kinetic energy is available.

Even more interesting it is to observe the differences between the turbulence models selected for this study. The $k-\epsilon$ models predict an entropy generation rate significantly larger than the $k-\omega$ model, by about 30%, in the larger control volume. The Spalart-Allmaras prediction is lower, but still larger than the one given by the $k-\omega$ model, by about 15%. This is due to the different formulation of the turbulent kinetic energy production and destruction terms, which are strictly related to the entropy production, as shown in Sec. 3.1. The $k-\omega$ SST models, in particular, uses a low-Reynolds correction in the boundary layer which is particularly effective in the presence of low Reynolds number flows, as in this case [147, 148]. This has an effect both on the amount of entropy generated, but also on the capability of the model to predict flow separation and stall at low Reynolds numbers.

Fig. 3.9 reports the total exergy in a cycle of period T_w, defined in Eqn. (2.6), using 3 approaches, which, as explained in Section 2.2.1, should in theory lead to very similar results.

$$\begin{aligned} E_P &= \int_{T_w} \Delta p_t Q \, dt \\ E_E &= \int_{T_w} \left(\dot{m} c_p \Delta T_t - \dot{m} T_{t,ref} \Delta s\right) dt \\ E_S &= \int_{T_w} \left(\mathcal{T}\Omega + T_{t,ref} \dot{S}_G\right) dt \end{aligned} \tag{3.21}$$

The last 2 methods are the *indirect* and *direct* approaches described by Herwig [117]. The exergy calculation E_S has been evaluated both considering the generation, $E_{S,g}$, and dissipation, $E_{S,d}$, of turbulent kinetic energy (Eqns. (3.19) and (3.20)).

It is interesting to note how the traditional approach (E_P) and the indirect method lead to same results, and this is a confirmation of the validity of the assumptions made in Section 2.2.1 ($\Delta p_t Q \approx \dot{m} c_p \Delta T_t - \dot{m} T_{t,ref} \Delta s$). On the contrary, the direct method (which requires the integration of the entropy production in the computational domain) based on the turbulent kinetic energy production ($E_{S,g}$) leads to an overestimation of the available energy. This difference is not too significant for the $k-\omega$ model (about 2%), larger for the other turbulence models, and especially for the $k-\epsilon$ STD (about 9%). This result is in line with the differences encountered when estimating the entropy generation in other applications: differences as large as 15% are not uncommon [149], and are due to the fact that CFD software do not solve the entropy equation, which therefore can be not strictly satisfied due to numerical errors, as explained in [150]. Lower discrepancies between the direct

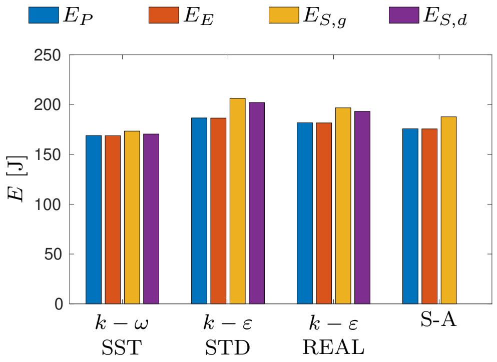

Figure 3.9: Total exergy calculations averaged on a cycle for different turbulence closure models.

method and the other ones can be obtained when using the turbulent kinetic energy dissipation ($E_{S,d}$). The overestimation still remains high for $k-\varepsilon$ models, but it almost disappears for the $k-\omega$ SST model.

The larger estimation of the available energy from Spalart-Allmaras and $k-\varepsilon$ models is linked to the overestimation of local entropy generation (see Fig. 3.8), which is due to the different treatment of the boundary layer region, assumed fully turbulent [147]. On the contrary, the $k-\omega$ SST model adopts the standard $k-\varepsilon$ model only away from the walls and an improved formulation within the boundary layer [148], where viscous effects predominate over turbulent ones.

This difference in boundary layer treatment among $k-\omega$ SST and $k-\varepsilon$ STD model is highlighted in Fig. 3.10, that clearly shows higher intensity of non-dimensional entropy production in the boundary layer region for the $k-\varepsilon$ model. This overestimation is more evident near the suction side of the blade and near the trailing edge, at all spanwise positions from hub to tip.

The above results have been used to evaluate the turbine efficiencies defined in Sec. 2. The values reported in Fig. 3.11 are a direct consequence of the results in Figs. 3.7, 3.8, and 3.9. The aerodynamic efficiency η_{ad} is lower than the total-to-total efficiency η_{tt}, as the static pressure drop that appears in its denominator is larger than the total pressure drop that is used to calculate the first-law efficiency (the former includes the exit dynamic head, which in a Wells turbine is lost). The second-law efficiency (which theoretically should be approximately equal to the latter), has a very similar value only when the denominator is calculated using the indirect method, while it is lower when the direct method is selected. A further difference exists depending on whether the entropy generation $\dot{S}_G$ is calculated using the dissipation or the production of turbulent kinetic energy, being the latter slightly larger than the former (see Fig. 3.8). These differences are smaller for the $k-\omega$ model than for Spalart-Allmaras and $k-\varepsilon$ models. The second-law efficiency calculated using the turbulent kinetic energy dissipation with the $k-\omega$ SST model is remarkably close to the first-law efficiency.

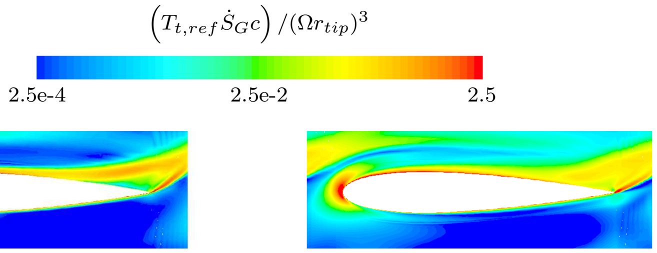

(a) 20% span

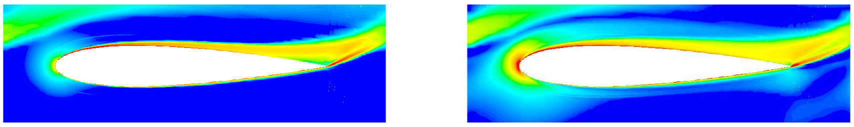

(b) 50% span

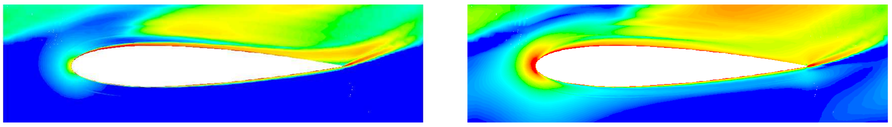

(c) 80% span

Figure 3.10: Close-up view of the non-dimensional entropy production at several blade span positions for the maximum flow coefficient $\phi = 0.23$ calculated using $k-\omega$ SST (left) and $k-\varepsilon$ STD (right) models

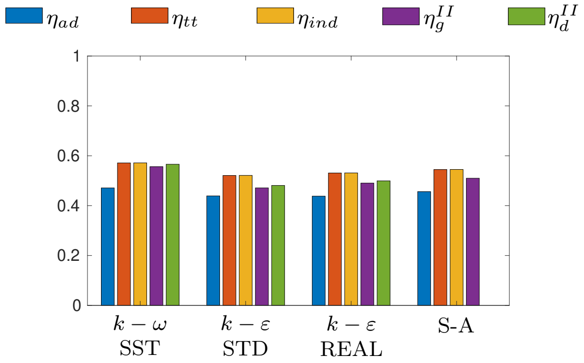

Figure 3.11: Rotor efficiencies averaged on cycle and calculated with different turbulence closure models

3.3.2 Simulations for $\phi_{max} = 0.345$

Figure 3.12 reports the performance parameters of the Wells turbine with an operating (sinusoidal) cycle with a maximum flow coefficient sufficient to produce deep stall conditions.

When comparing the curves in Fig. 3.12, the $k-\varepsilon$ model in its standard formulation is unable to predict the turbine stall and the performance is always increasing with the flow coefficient (in the range considered here, i.e. $\phi = -0.345 \div 0.345$). The $k-\varepsilon$ REAL model predicts the presence of light stall for a ϕ just above 0.3.

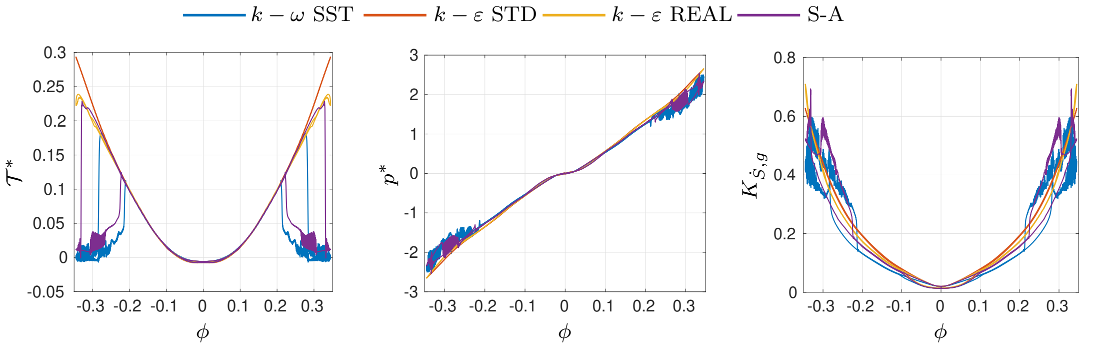

(a) Torque coefficient (b) Pressure drop coefficient (c) Non-dimensional entropy generation

Figure 3.12: Non-dimensional performance of the rotor with NACA0015 blade profile and 6 blades under deep stall conditions, as a function of the flow coefficient ϕ, estimated with different turbulent closure models.

This is due to the difficulty of $k-\varepsilon$ models to correctly predict the separation of the boundary layer for low Reynolds number flows, in particular in the $k-\varepsilon$ STD formulation where the boundary layer is considered as fully turbulent [147]. $k-\omega$ SST and Spalart-Allmaras model predict the occurrence of stall (at ϕ equal to 0.28 and 0.32, respectively). After stall, the torque coefficient drops dramatically, and the entropy generation increases correspondingly. A high frequency oscillation in all performance parameters can be observed. During deceleration, the reattachment of the boundary layer, which corresponds to the exit from the stalled conditions, happens for a lower flow coefficient (equal to 0.2 and 0.22 for $k-\omega$ SST and Spalart-Allmaras models). This leads to the presence of a hysteretic loop, which does not extend to the clean part of the curves, i.e. after reattachment. This hysteresis is not necessarily caused by dynamic effects, as a static stall hysteresis is well documented for many lifting surfaces [145, 146, 151, 152].

In order to better understand the difference between $k-\omega$ and $k-\varepsilon$ models predictions, Fig. 3.13 shows the vortical structures around the blade calculated with the two models. Iso-surfaces of Q-criterion, colored by the non-dimensional entropy production, are reported.

The comparisons in Fig. 3.13 show that the $k-\varepsilon$ model underestimates the large vortex located near the suction-side (SS) of the blade, as well as the large area of reversed flow near the trailing edge. The tip vortex grows for larger flow-coefficient values until it appears destroyed and a roll-up vortex can be observed on the same blade side near the trailing edge. The vortical structures located near the trailing edge when the blade is stalled are again smaller in $k-\varepsilon$ predictions than in $k-\omega$ ones. Both models show the entropy production growing with the flow-coefficient, as expected, with larger values being predicted by the $k-\varepsilon$ model especially near the blade surface, as previous observed in Fig. 3.10.

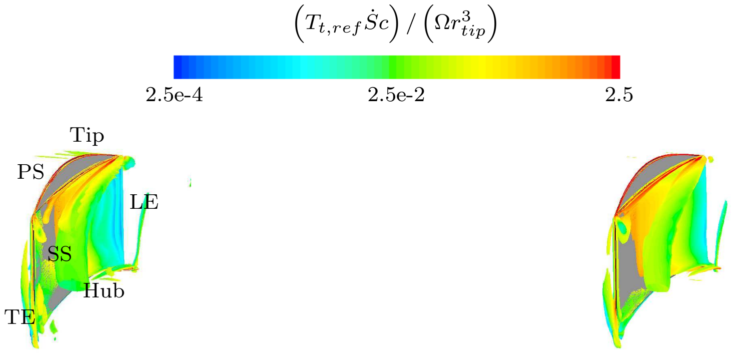
$\left(T_{t,ref}\dot{S}c\right) / \left(\Omega r_{tip}^3\right)$
2.5e-4
2.5e-2
2.5
Tip
PS
LE
SS
Hub
TE

(a) $\phi = 0.19$

(b) $\phi = 0.23$

(c) $\phi = 0.30$

$k-\omega$ SST
$k-\varepsilon$ STD

(d) $\phi = 0.345$

Figure 3.13: Iso-surfaces of Q criterion ($Q = 2.25\text{e}6\ \text{s}^{-2}$) colored by non-dimensional entropy production

3.4 Comparisons among different rotor geometries

Five rotor geometries have been compared, with 3 rotor-tip solidities (0.48, 0.57, 0.67) and 3 blade thicknesses (NACA 0012, NACA 0015, NACA 0020 profiles). All the calculations have been performed using $k-\omega$ SST model under dynamic (sinusoidal) flow-conditions.

Starting from the global performance comparisons as done in Sec. 3.3, Figs. 3.14 and 3.15 report the well-known non-dimensional parameters for the rotors with the same number of blades and with equal blade profile, respectively.

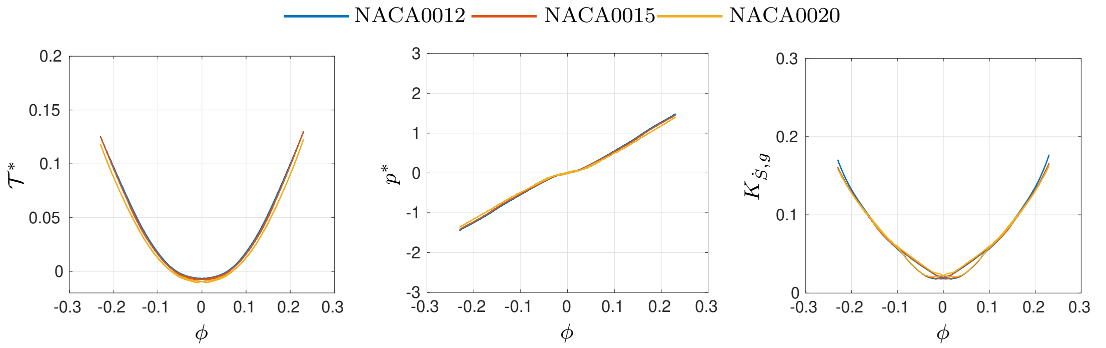

(a) Torque coefficient (b) Pressure drop coefficient (c) Non-dimensional entropy generation

Figure 3.14: Non-dimensional performance of the rotor with 6 blades and different blade profiles, as a function of the flow coefficient ϕ.

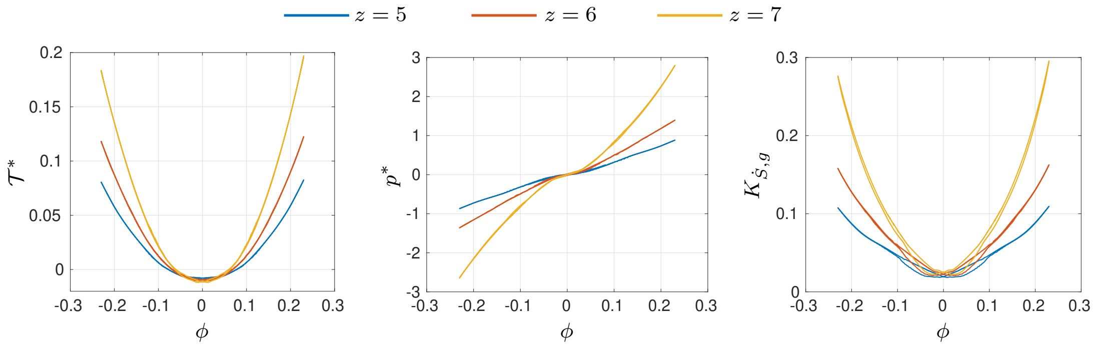

(a) Torque coefficient (b) Pressure drop coefficient (c) Non-dimensional entropy generation

Figure 3.15: Non-dimensional performance of the rotor with NACA0020 blade profile and different number of blades, as a function of the flow coefficient ϕ.

In Fig. 3.14, no significant modifications in performance can be noticed for a different blade profile thickness, while Fig. 3.15 highlights the strong effect of the rotor solidity on both torque- and pressure-coefficient. This is due to the blockage effect exerted by the rotor on the air-flow, directly dependent on the number of blades [64, 67, 153].

Fig. 3.16 compares the averaged non-dimensional entropy production for different rotor geometries.

The results are in agreement with the considerations drawn from the performance parameters comparisons, i.e. it is possible to state that the change in blade-profile

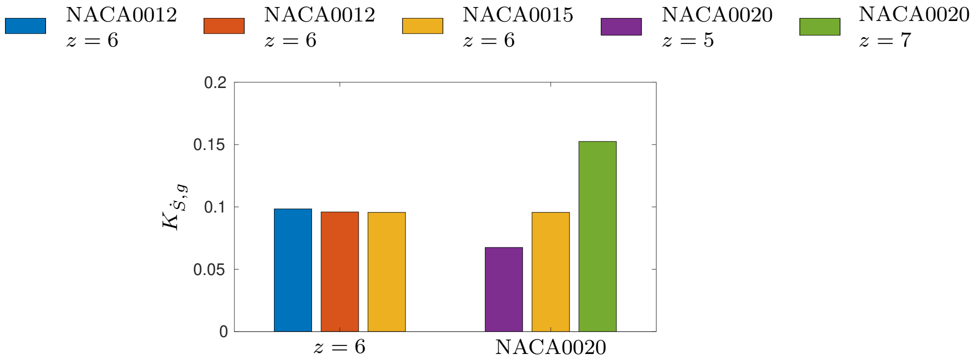

Figure 3.16: Non-dimensional entropy production averaged on a cycle for different rotor geometries

thickness does not modify substantially the averaged rotor losses over a cycle and this is confirmed by a very similar entropy production for all 3 rotors with equal solidity. On the contrary, when the rotor solidity increases, the entropy production also increases and this fact is again related to the blockage effect exerted by the rotor on the flow. The effect of the rotor solidity on the entropy production can be better observed in Fig. 3.17, where the local entropy production field around the blade is shown at different spanwise positions.

The contour plots allow to make a qualitative analysis of the losses along the blade span. In particular, while low solidity rotors ($z = 5, 6$) shows similar amounts of entropy production at all spanwise positions, the highest solidity rotor ($z = 7$) experiences higher losses along the whole blade span. This is more evident in the hub region where the blades are the closest (i.e. the solidity assumes its highest value) and the blockage effect determines higher losses, as it can be determined by comparing the vortical structures in Fig. 3.18 for two different flow conditions. In fact, near the tip region, the entropy generation field around the 3 rotors looks more similar than for lower spanwise positions (Fig. 3.17), except for a more pronounced disruption of the vortical structures (Fig. 3.18) downstream the suction side.

Fig. 3.19 reports the energy production for the different geometries simulated, calculated as in Eqn. (3.21).

The available energy calculated with the traditional and the indirect methods (E_P and E_E) lead to very close predictions. The differences are larger when the available energy is evaluated using the direct method, i.e. by integrating the production or destruction of turbulent kinetic energy inside the domain: it is interesting to note how this last estimation is always larger than the other two, except for the case of the rotor with the highest solidity. It is reasonable to assume larger numerical errors in the prediction of entropy generation for the rotor with the largest solidity, where secondary flow structures are larger and more complex due to the smaller flow passage and higher pressure difference across the blade. The difference is in any case well below the values reported in other similar studies [117, 120].

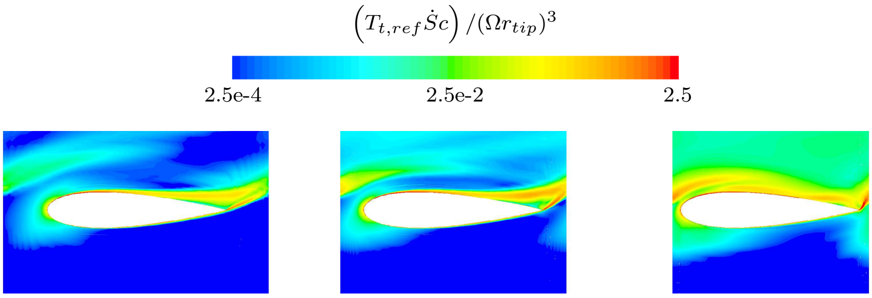

(a) 20% chord

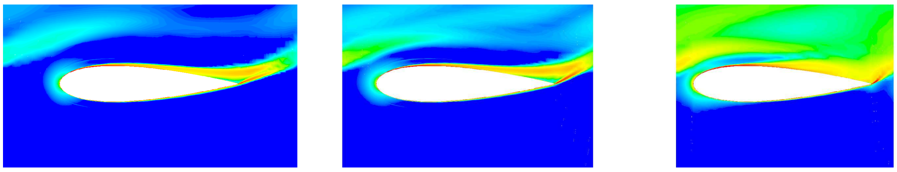

(b) 50% span

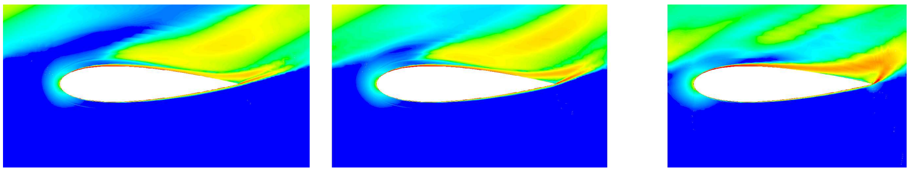

(c) 80% span

Figure 3.17: Non-dimensional entropy production at several blade span positions for the maximum flow coefficient $\phi = 0.23$ and for rotor with $z = 5$ (left), $z = 6$ (center) and $z = 7$ (right)

Finally, the mean rotor efficiencies reported in Fig. 3.20 allow to make a better comparison among the different geometries.

The rotors with different blade thicknesses do not present significant variations in efficiency for the selected rotor solidity, i.e. 0.57: a small drop in efficiency is reported for the rotor with the largest thickness, as already reported in the experiments [1]. On the contrary, the solidity has a higher impact on the efficiency, and the 2 lower solidities represent the best solutions under these flow conditions. These results are comparable with the ones obtained in the experiments of [1] and [153].

The analysis presented in this Chapter has shown that, under the assumptions typical for Wells turbines, the so-called first- and second-law efficiencies give almost the same values. While the former requires the evaluation of the pressure drop across the machine, the latter can be calculated either by evaluating the entropy rise across the machine (the so-called indirect method [117]) or by integrating the local entropy generation rate in the domain (the direct method [117]). These two measures are theoretically equivalent, but some discrepancies can arise from CFD simulations due to numerical errors, as entropy is not necessarily conserved in CFD solvers [150].

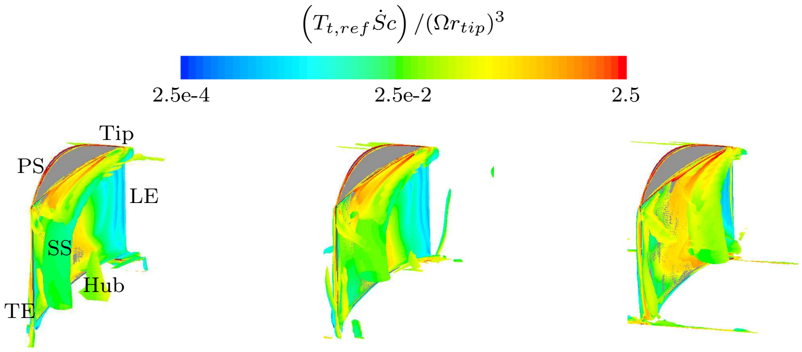

(a) $\phi = 0.19$

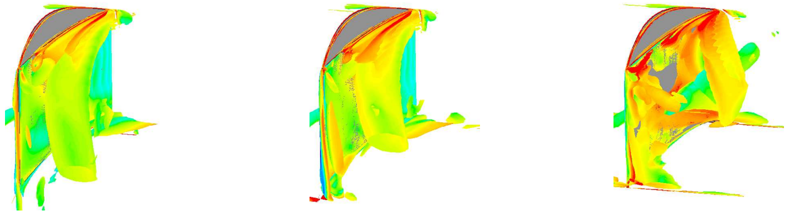

(b) $\phi = 0.23$

Figure 3.18: Iso-surfaces of Q criterion ($Q = 2.25\text{e}6\ \text{s}^{-2}$) colored by non-dimensional entropy production for different flow conditions and for rotor with $z = 5$ (left), $z = 6$ (cent) and $z = 7$ (right)

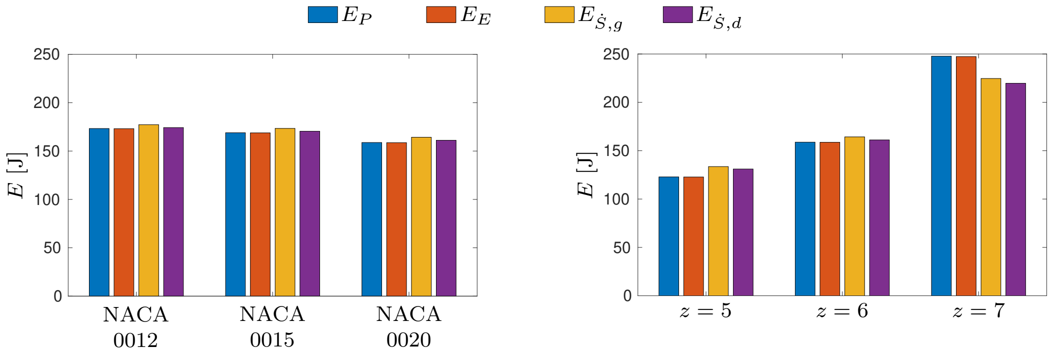

(a) Rotors with 6 blades

(b) Rotors with NACA0020 blade profile

Figure 3.19: Energy averaged on a cycle for different rotor geometries.

Performance comparison made between different rotor geometries have shown that the blade thickness has a minimal effect on the efficiency, for the case study under consideration. On the contrary, the efficiency is significantly affected by the solidity of the machine.

Finally, theoretical derivations and numerical analyses have been developed for a compressible flow in order to make the methodology applicable also to other problems. For the problems analyzed in this work, compressibility effects never accounted

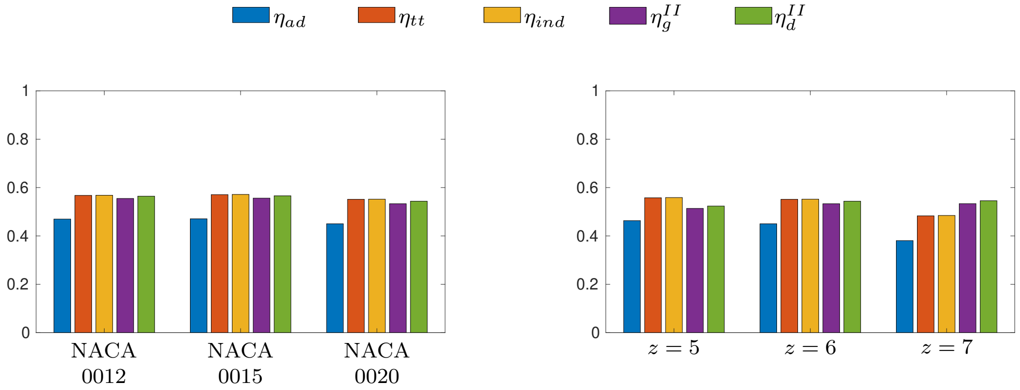

(a) Rotors with 6 blades

(b) Rotors with NACA0020 blade profile

Figure 3.20: Rotors efficiencies averaged on a cycle for different rotor geometries.

for more than 0.02% of the total entropy generation.

Chapter 4

Modifications to the facility housed at DIMCM

This chapter presents modifications and improvements to the experimental OWC simulator facility housed in the Turbomachineries Laboratory at DIMCM. The rig is composed of two main units: the OWC simulator and the PTO, i.e. a monoplane Wells turbine. Both these two parts have been modified and substituted to the old ones. In particular, a new duct to housed the turbine and a new "modular" Wells turbine have been designed and installed to be tested.

In the first Section of this Chapter, the existing rig is described highlighting the reasons that led the new design. The second Section presents a summary modifications to fixed parts of the facility, while the third Section introduces the "modular" Wells turbine.

4.1 The existing facility

In early 1990s, an experimental facility capable to simulate the working conditions of an OWC system coupled with a Wells turbine as power-take-off (PTO), was built in the Turbomachinery Laboratory of the Department of Mechanical, Chemical and Materials Engineering (DIMCM) in Cagliari State University. A schematic view of the test rig is shown in Fig. 4.1.

The facility is provided of a piston, driven by an hydraulic unit, which moves inside a steel chamber, reproducing the periodic wave motion as happens inside an OWC and generating a periodic bi-directional airflow. The chamber has a diameter of about 1 m and the ratio between its section and that of the turbine is about 38, ensuring a flow speed between 10÷20 m/s. The amplitude and period of the piston motion oscillation can both be adjusted in order to obtain the desired flow rate, while a linear potentiometer measures the piston position during its stroke and is used for feedback control in the hydraulic unit. Furthermore, the shape of the periodic motion of the piston can be sinusoidal or linear.

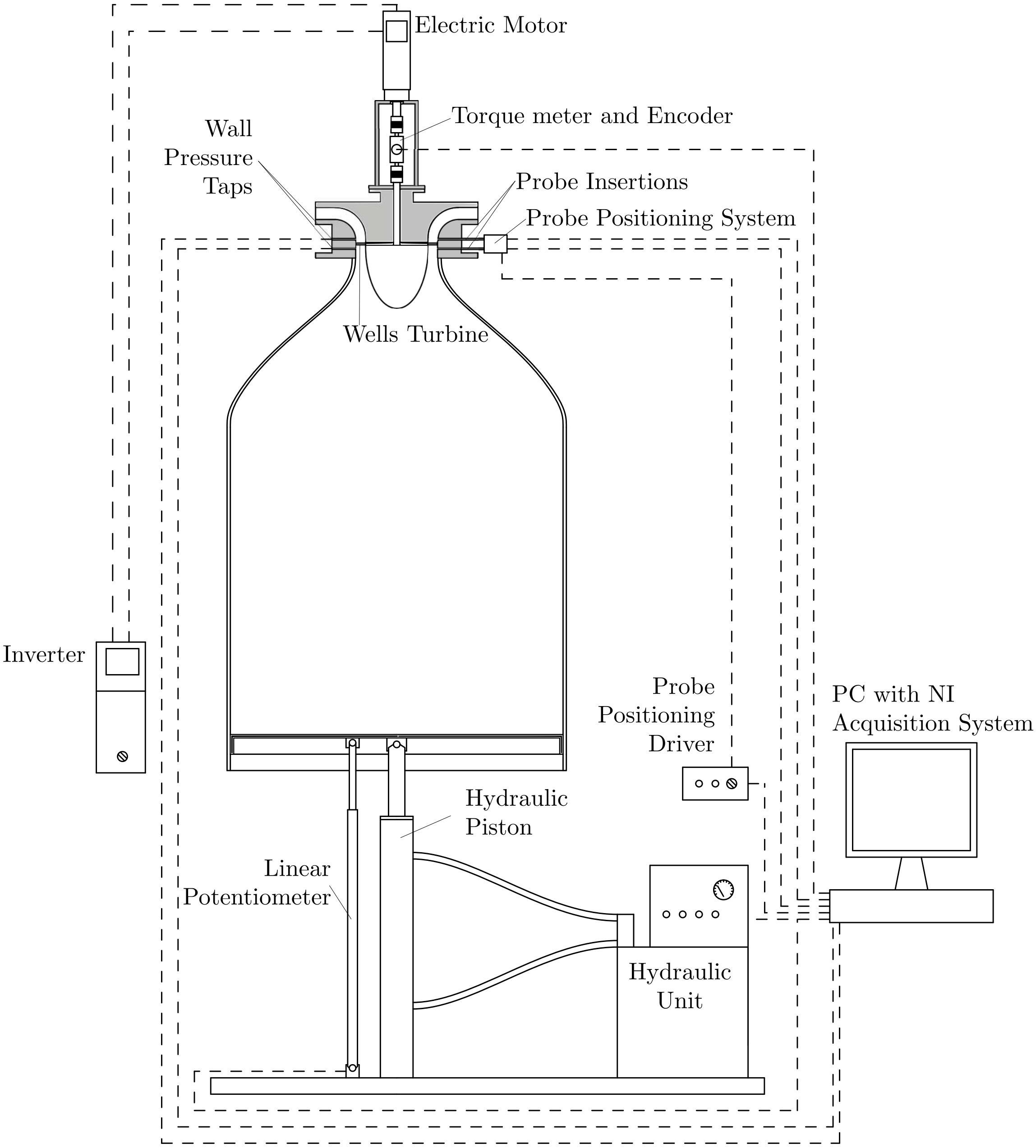
Electric Motor
Torque meter and Encoder
Wall Pressure Taps
Probe Insertions
Probe Positioning System
Wells Turbine
Inverter
Probe Positioning Driver
PC with NI Acquisition System
Hydraulic Piston
Linear Potentiometer
Hydraulic Unit

Figure 4.1: Simplified scheme of the experimental rig.

In the top section of the chamber, see close-up view in Fig. 4.2, is housed a Wells turbine which drives a electric induction machine controlled by an inverter with encoder feedback. Its main geometric characteristics are summarized in Tab. 4.1.

The output torque is measured by a shaft-to-shaft rotary torque sensor with a built-in optical encoder for speed rotation measurements. The DRFL_I Instrumen-

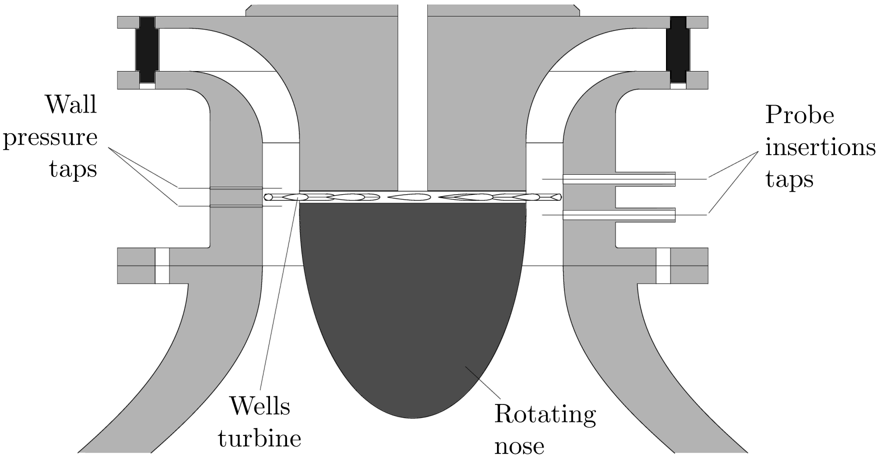

Figure 4.2: Close-up view of the turbine and of the top part of the experimental setup.

Table 4.1: High solidity Wells turbine data.

Rotor Tip Diameter	250 [mm]
Rotor Hub Diameter	190 [mm]
Tip Clearance	1 [mm]
Chord Length	36 [mm]
Number of Blades	14
Airfoil Profile	NACA 0015
Solidity	0.729
Sweep Ratio	0.417 (15/36)
Hub-to-tip Ratio	0.76

tation Devices torque transducer can read a maximum torque of ±2 Nm with a maximum measurement fault of 0.1% of full scale.

The fixed part of the rig is provided by wall pressure taps made both at its ambient and chamber side about ±7.5 mm far from the turbine blade chord (see Fig. 4.2). Transducers for wall pressure measurements have been selected with respect to the rotor side, i.e. ambient or chamber, as different maximum values of pressures were expected. Their calibration has shown a maximum uncertainty of ±3.5 Pa for the ambient side transducer and ±15 Pa for the chamber side one.

All the instrumentation used in the present work is listed in App. C, with more detailed specs.

Probe insertions have been made at both rotor sides, allowing to characterize the near-rotor flow by using both aerodynamic pressure probes [57] and hot-wire probes [58]. A motorized system, reproduced in Fig. 4.3, allows to rotate the probe around its axis, to change the orientation of the probe sensor, and to move it along the blade height to perform the radial traversing.

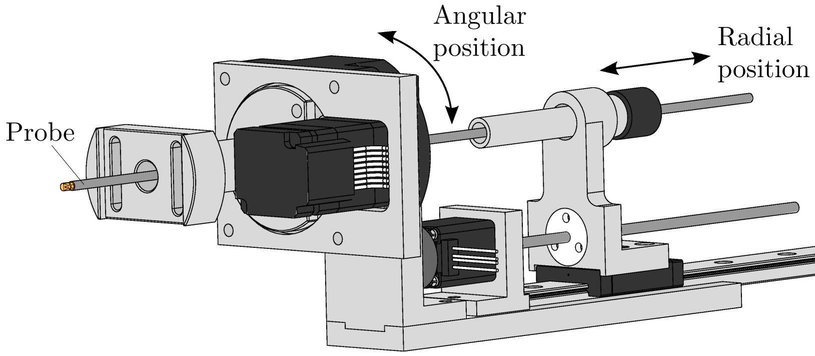

Figure 4.3: Motorized traversing system used for local measurements.

The configuration of the experimental setup does not allow to measure the flow rate with standardized measuring instruments, as possible in the case of a set-up in which the flow is permanent and unidirectional [48, 59]. The flow rate can be calculated based on the piston motion, and taking into account the time delay between the piston speed and the corresponding flow speed at the rotor inlet, induced by the presence of the chamber volume. This effect has been neglected in the past [1, 56, 84, 86, 90–92, 154], but it has been extensively described and clarified in a number of more recent papers [57, 58, 82, 93, 129, 131, 155].

4.2 The new rig

The existing rig, described in the previous section, involves some constructive limitations which have lead the design of the modifications that will be presented in the following sections. These effects can be summarizes as follows:

1. The bent duct at the ambient side of the rotor determines a pressure gradient along the blade span that mitigates the blockage effect at the blade root and makes the angle of incidence almost constant along the blade span [61]. Although these effects improve turbine performance, especially during the inflow phase, i.e. the flow is coming from the atmosphere to the chamber, in the outflow phase this behavior does not occur. In order to make almost symmetric the operation of the turbine, an axial duct has been introduced in place of the existing bent duct, thus obtaining the typical configuration used in a OWC plant.

2. As can be observed in Fig. 4.2, at the chamber side of the rig the spinner is joined to the rotor. The presence of a rotating spinner nose determines a swirled flow in the hub region which strongly affects the 3-dimensional nature

of the flow and makes more complicated the local investigations and the 3-dimensional local flow reconstruction by pressure probes. In order to reduce the differences in the configuration of the feeding channels to the turbine rotor, and thus obtain a similar incoming flow to the rotor during both the two phases, fixed ogives are used on both sides of the turbine. More detailed information about the differences between fixed and rotating spinner can be found in App. A, where the two configurations are compared by means of CFD simulations.

3. Another aspect concerns the possibility of using appropriate and different tools for local flow investigations, upstream and downstream of the rotor. In the existing test section, only cylindrical probes at fixed axial distance from the rotor blades can be used. This configuration does not allow to use probe geometries such as “L-shaped” ones. A probe insertion shaped as a buttonhole has been designed, coupled with a probe-holder shaped as the hole.

Figure 4.4 shown the new rig designed and built at the DIMCM, highlighting the most important modifications respect to the old setup, as described in the present section.

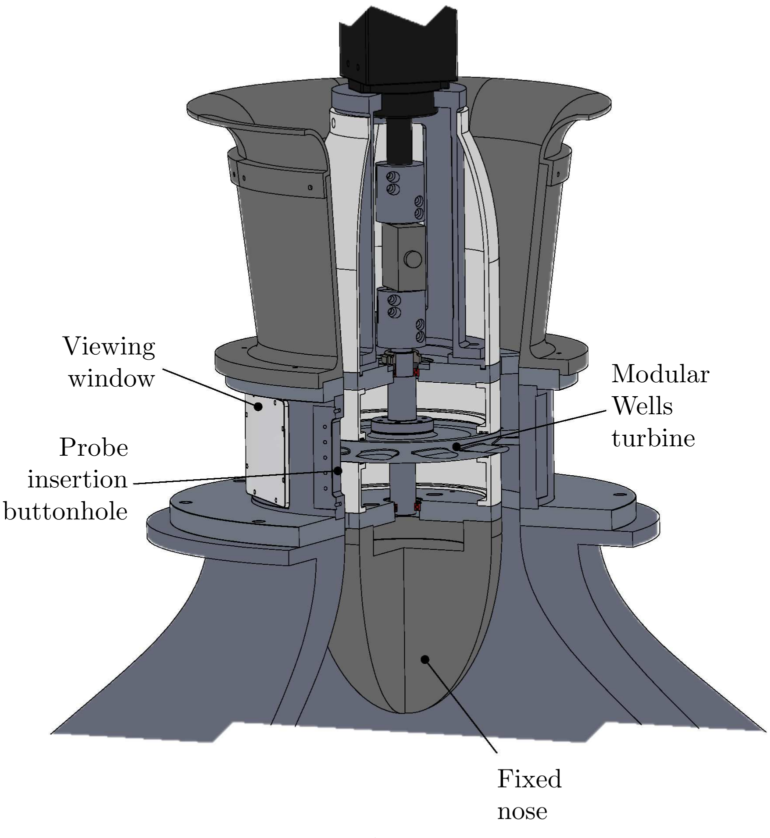

Figure 4.4: 3-dimensional section view of the new rig with the modular Wells turbine.

More pics of the novel rig are reported in Fig. 4.5, showing in particular the viewing window, made of transparent PMMA, Fig. 4.5 (b) and the aerodynamic probe in its insertion near the rotor, Fig. 4.5 (c).

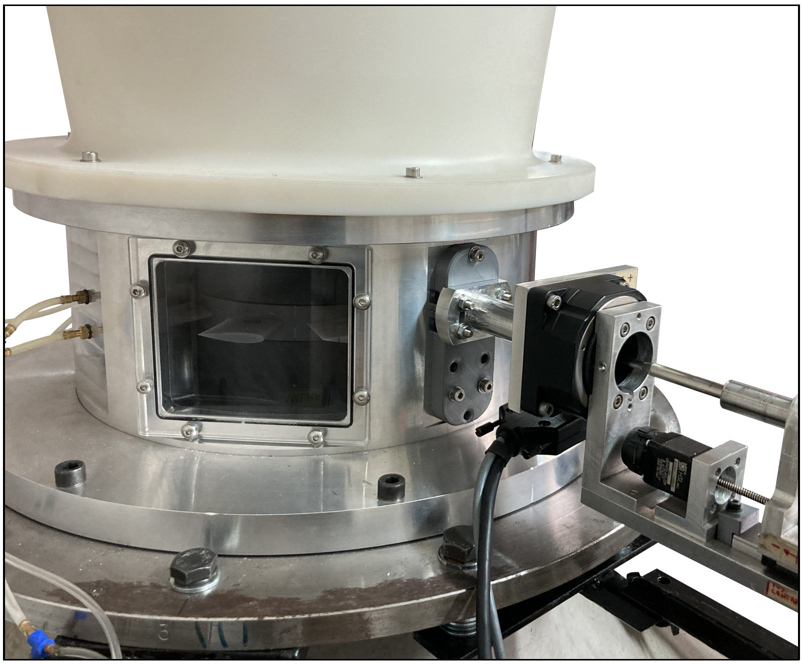

(a) Overall view.

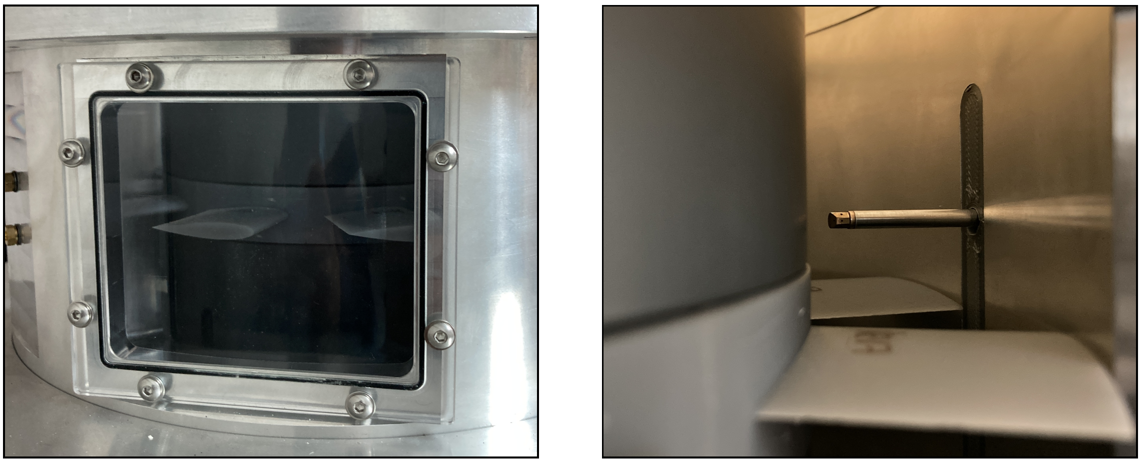

(b) Viewing window.

(c) Aerodynamic probe in the Wells turbine.

Figure 4.5: Detailed pics of the novel rig.

4.3 A "modular" Wells turbine

In order to make easier to experimentally investigate Wells turbines with different geometries, a "modular" turbine has been designed and built. The term "modular" means that the rotor geometry can be easily modified by substituting the blades. In particular, the new turbine is composed of two disks made of Aluminum (Ergal 7075) coupled together with bolts with 3D-printed blades in between, as shown in Fig. 4.6. This simple design is similar to the one used in traditional turbomachines such as fans or gas turbines, where two plates tight the root of the blades. The two disks, which determine the hub of the turbine, do not have any tangential constraint that holds the blade, as in traditional turbomachines: it means that rotor geometry can be changed by modifying its solidity, i.e. the number of blades or its chord, the airfoil shape and more in general the blade three-dimensional shape. The use of 3D-printing technology for blades ensures rapidity of blade construction, without loose geometrical tolerances and mechanical properties required for the experimental application. Furthermore, as materials used for 3D-printing the blade have a value of density about 3 times lower than aluminum, the moment of inertia of the modular rotor is lower than the old turbine, fully made of Aluminum alloy Ergal 7075, due to the reduction of the rotor mass in its most peripheral parts. This characteristics become relevant for turbine speed control, see Sec. 6.1, as the energy required by the inverter to act on the rotational speed decreases with the rotor moment of inertia and then rotational speed modification can be actuated faster.

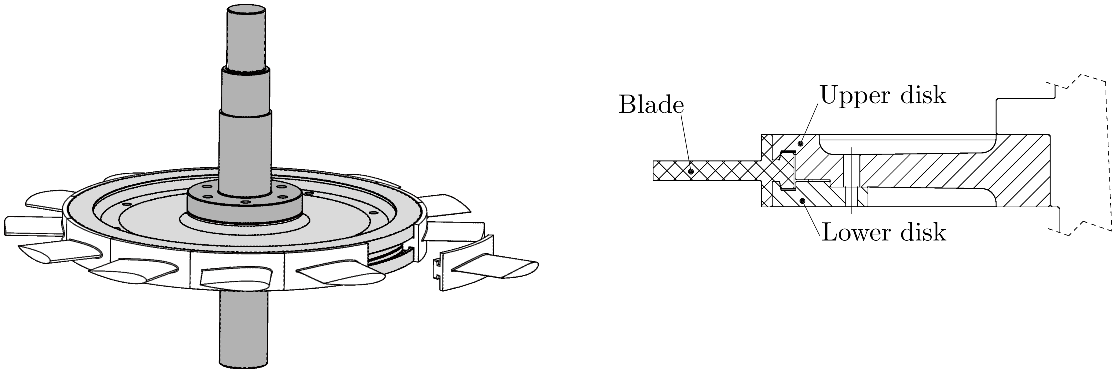

(a) Exploded view. (b) Axial sectional view.

Figure 4.6: Demonstrative views of the modular Wells turbine.

It could be noted that the existing Wells turbine, see Tab. 4.1, presents an unusual value of the *hub-to-tip* ratio, i.e. equal to 0.76. Wells turbines used in experimental analyses generally have a value of the *hub-to-tip* ratio around 0.6 [50, 56, 97, 106, 156] with a minimum of 0.43 for [157] and a maximum of 0.7 for [101]. Wells turbines installed in energy plants have similar values of the *hub-to-tip* ratio, e.g. equal to 0.6 for the Pico Power Plant [44] and 0.62 for the LIMPET device [45]. Raghunathan [158] suggests an optimum value of about 0.6 in designing of a Wells turbine, showing also its effect on turbine efficiency. The reasons behind the high value of the *hub-to-tip* ratio of the Wells turbine housed at the DIMCM, is strictly related to the size of the OWC chamber and to the capability of the piston to reproduce typical wave motion periods and amplitudes. The area ratio between the OWC and the turbine determines the averaged speed of the flow in the turbine section, when a piston motion is selected, and it is designed in order to reproduce the characteristic operating range of a Wells turbine. Consequently, turbine diameters at the hub and tip depend on the area ratio and rig fittings. This constrained choice also affects the definition of turbine solidity in order to ensure the self-starting behavior of the turbine (it was an important characteristic when the rig was designed in early 1990s). Raghunathan [158] shows that for high values of the *hub-to-tip* ratio, high values of turbine solidity are required to facilitate the self-starting behavior of the turbine.

The new rig has been designed by preserving the actual value of the *hub-to-tip* ratio also to make possible to test the modular turbine with a variable-pitch turbine designed in [159].

Chapter 5

Experimental characterization of a Wells turbine

This Chapter summarizes the experimental analyses on a new Wells turbine with a lower solidity respect to the one previously analyzed [57, 58, 61] (see Sec. 4.1, Tab. 4.1). Its main geometric parameters are reported in Tab. 5.1.

Table 5.1: Geometric parameters of the novel low solidity Wells turbine.

Rotor Tip Diameter	250 mm
Rotor Hub Diameter	190 mm
Tip Clearance	1 mm
Chord Length	36 mm
Number of Blades	12
Airfoil Profile	NACA 0015
Solidity	0.625
Sweep Ratio	0.417 (15/36)
Hub-to-tip Ratio	0.76

The solidity of the turbine has been modified to reduce the distortion of the flow field in the vicinity of the turbine hub region, as observed in [61]. The new solidity value is representative of the typical values adopted in literature [50, 56, 97, 106, 156], while the other geometric characteristics of the DIMCM's rig have been retained (in particular the *hub-to-tip* ratio, as discussed in 4.3).

In Sec. 5.1, preliminary analyses of the dynamic behavior of the new turbine have been presented, i.e. its value of inertia and the torque loss due to windage and friction. In Sec. 5.2, the stall limit of the turbine is investigated, under stationary flow conditions. Then, Sec. 5.3 presents the performance of the Wells turbine under non-stationary flow conditions, both with global and local measurements, i.e the 3-dimensional flow has been investigated upstream and downstream the rotor by using an aerodynamic pressure probe. More detailed analyses, Sec. 5.4, have been conducted on the reconstruction of the flow field in a blade pitch, by using a miniaturized hot-wire-anemometer (HWA) probe.

List of symbols

	Acronyms
BDC	bottom dead center
HW	hot-wire
NI	National Instruments ®
OWC	oscillating water column
PTO	power take off
TDC	top dead center
UPM	uncertainty propagation method

	Non-dimensional properties
η	efficiency
$K_{x,\phi}$	turbine damping coefficient
λ	velocity coefficient
Λ	work coefficient
ϕ	flow coefficient
ψ	velocity reduction coefficient
p_w^*	wall static pressure drop coefficient
r^*	$= {}^{(r-r_{hub})}/_{(r_{tip}-rhub)}$ non-dimensional turbine radius
$\mathcal{T}^*$	torque coefficient
Tu	turbulence intensity
ξ_{EX}	loss coefficient related to the exit kinetic energy
ξ_R	loss coefficient related to the aerodynamic of the rotor
z	number of blades
Z^*	$= {}^{(Z-Z_{min})}/_{(Z_{min}-Z_{max})}$ non-dimensional piston position
ζ_D	kinetic energy defect

	Dimensional properties
α	angle of the absolute flow
β	angle of the relative flow
c	blade chord
C	absolute velocity
E	voltage
J	rotor's inertia
$\dot{m}$	mass flow rate
Ω	angular rotational frequency
p	static pressure
p_w	wall static pressure
Q	volumetric flow rate
r	turbine radius
ρ	air density
s	circumferential position
σ	root-mean-square
t	time
$\mathcal{T}$	torque
t_b	blade pitch
T_w	wave period, piston period
U	peripheral rotor speed, blade speed
V	velocity
V_F	effective cooling velocity
W	relative velocity
Z	piston position

	Subscripts and superscripts
$\overline{()}$	mean value
1	inlet

2	outlet	r	radial direction
ad	aerodynamic	ref	reference value
fs	full scale	θ	tangential direction
g	gobal	tip	turbine tip
hub	turbine hub	w	wall
$loss$	lost	z	axial direction
$meas$	measured	t	total condition

5.1 Inertia and windage losses

In order to evaluate the torque loss for windage and bearing friction, the torque at the turbine axis has been measured at several speeds of rotation, kept constant and in no-load conditions. Each test lasted at least 5 seconds, in which torque and rotor speed were acquired with a sampling frequency of 1 kHz.

The result of the test is shown in Fig. 5.1, where the measured torque, non-dimensionalized with respect to the absolute full scale value ($\mathcal{T}_{fs} = 2$ Nm), is reported as a function of the rotational speed.

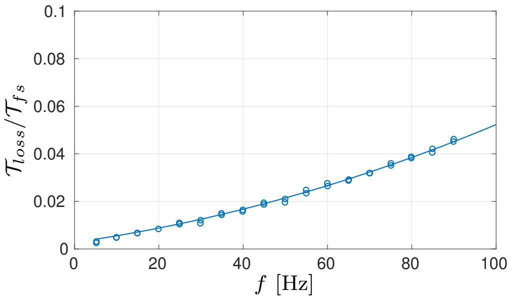

Figure 5.1: Windage and friction torque losses as a function of the rotational frequency of the turbine.

The continuous line represents the 2$^{\text{nd}}$ degree polynomial fitting of measured values (Eqn. (5.1)).

$$\frac{\mathcal{T}_{loss}}{\mathcal{T}_{fs}} = Af^2 + Bf + C \tag{5.1}$$

where f is the rotational frequency and constants' values, i.e. A, B and C, calculated with a least-square error method, are listed below.

$$\begin{cases} A = 2.44 \cdot 10^{-6} \\ B = 2.51 \cdot 10^{-4} \\ C = 2.80 \cdot 10^{-3} \end{cases} \tag{5.2}$$

In order to determine rotor's inertia, the turbine has been submitted to accelerating and decelerating ramps, by varying the rotor velocity with a inverter controlled by a voltage signal generated by a NI multi-function board. Several tests have been performed, by changing the slope and the amplitude of accelerating and decelerating phases. Figure 5.2 reports typical profile of turbine velocity and measured torque for a test.

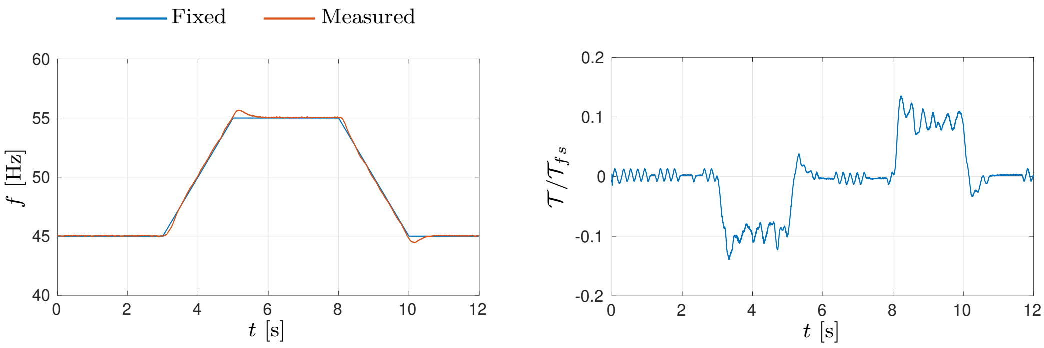

(a) Rotational frequency during the test.

(b) Measured torque.

Figure 5.2: Typical test for inertia calculation.

It can be observed that the turbine requires a small settling time to reach stationary operating conditions. In fact, only small overshoots and undershoots can be appreciated during the test. For the calculation of the inertia, only the part of the ramps cleaned of the settling zones was considered. The value of the turbine's inertia can be evaluated by applying the Newton's second law for rotational motion as done in Eqn. (5.3).

$$\mathcal{T}_{ad} - \mathcal{T}_{meas} - \mathcal{T}_{loss} = J\frac{\mathrm{d}\Omega}{\mathrm{d}t} \tag{5.3}$$

where J is the inertia of the rotor and $\mathrm{d}\Omega/\mathrm{d}t$ is the angular acceleration of the rotor. Then, assuming equal to zero the aerodynamic torque $\mathcal{T}_{ad}$, as these tests were conducted in no-load conditions, the value of the inertia can be evaluated as follows

$$J = \frac{-\mathcal{T}_{meas} - \mathcal{T}_{loss}}{{}^{\mathrm{d}\Omega}\!/_{\mathrm{d}t}} \tag{5.4}$$

The estimation of the value of rotor inertia has given a slight difference when it was estimated during accelerating and decelerating ramp, as listed below.

$$J = \begin{cases} 5.646 \cdot 10^{-3} \ \ [\mathrm{kgm}^2] \text{ during accelerating ramp} \\ 5.955 \cdot 10^{-3} \ \ [\mathrm{kgm}^2] \text{ during decelerating ramp} \end{cases} \tag{5.5}$$

The averaged value of $5.80 \cdot 10^{-3}$ [kgm^2] will be considered in future calculations, since the difference between the results in Eqn. (5.5) is smaller than the corresponding uncertainty, which depends on torque and speed measurement uncertainties and on the numerical calculation of turbine acceleration $\mathrm{d}\Omega/\mathrm{d}t$.

5.2 Stall limit under stationary flow

In order to characterize the stall limit of the turbine, tests under stationary flow have been conducted. The analysis has been carried out in the OWC simulator rig, by setting the piston motion to follow periodic ramps, as shown in Fig. 5.3.

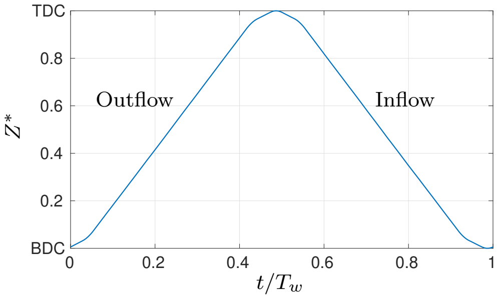

Figure 5.3: Non-dimensional piston position as a function of the non-dimensional piston period in case of triangular wave form.

The motion period has been set to 20 s and measurements have been performed only during the outflow phase, with a sampling rate of 1 kHz. Different operating conditions of the turbine have been considered by changing its rotational speed. During the ramp of the outflow phase, the flow velocity is constant as well as the wall static pressure drop through the turbine rotor and the measured torque. The flow speed has been calculated based on piston position recorded during the test. Then, global performance can be derived from these measurements and expressed in non-dimensional form (as proposed in Sec. 2.1). Measurements near motion inversion have not been used for calculations and only the central values (for about 4 s) of each ramp have been considered. Performance non-dimensionalized with respect to the turbine tip radius have been reported in Fig. 5.4.

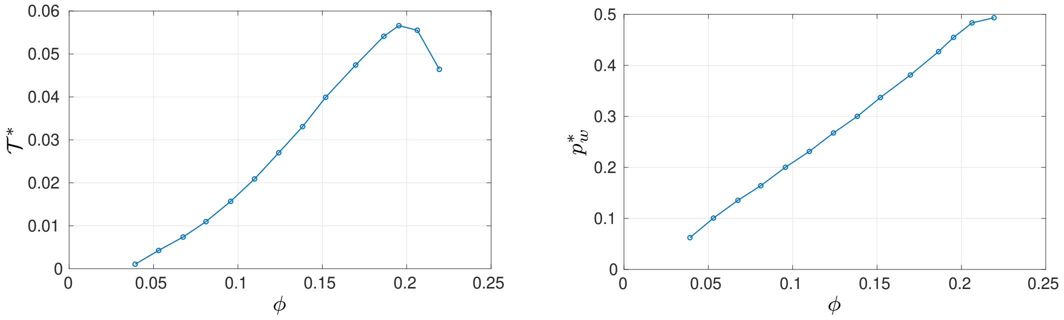

(a) Non-dimensional torque. (b) Non-dimensional static pressure drop.

Figure 5.4: Non-dimensional performance under stationary flow.

The trend of the torque coefficient $\mathcal{T}^*$ with respect to the flow coefficient ϕ clearly highlights that the stall limit is reached approximately for the value of $\phi = 0.2$.

This trend can be assumed as a function of order 2 of the flow coefficient, while the non-dimensional wall pressure drop p_w^* is almost linear with ϕ, except under stall conditions. This allows a simple evaluation of the turbine damping coefficient $K_{x,\phi}$, as proposed in [155], by calculating the slope of the curve in Fig. 5.4 (b). Then

$$K_{x,\phi} = 2.485 \tag{5.6}$$

This value characterizes the turbine and it can be useful to numerically reproduce its behavior.

5.3 Turbine behavior under non-stationary flow

This section describes the behavior of the tested turbine under non-stationary flow conditions, during a sinusoidal piston motion of the OWC simulator. The main settings of the experiments are reported in Tab. 5.2, while Fig. 5.5 shows the non-dimensional piston displacement as a function of the non-dimensional time.

Table 5.2: Settings of experiments.

Turbine rotational frequency, f	50÷80 Hz
Piston stroke amplitude	≈ 850 mm
Piston period, T_w	7 - 8 - 9 s
Reynolds' number of the outlet flow based on blade chord	$\approx 1.32\times10^5$

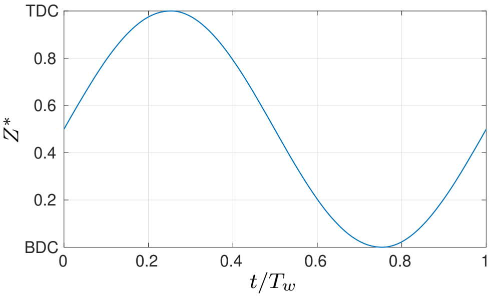

Figure 5.5: Non-dimensional piston motion in experiments.

The acquisition time for each test has been set to record signals for at least 5 piston periods. This allows to obtain a periodic mean distribution of the non-stationary flow variables after a phase locked averaging process of the acquired signals. Data acquisition has been performed with a sampling rate of 1 kHz for all the acquired signals.

The performance characteristics of the turbine will be presented considering both global and local measurements. With the global measurement approach, wall static pressures, both upstream and downstream of the rotor, the output torque at turbine shaft and its rotating speed, and the piston position were measured. Several test conditions have been considered by setting different periods of the piston motion and turbine rotating speeds.

5.3.1 Global performance

Traditional non-dimensional performance, as calculated in Eqn. (2.1), are reported in Fig. 5.6, in terms of torque coefficient, $\mathcal{T}^*$, static pressure coefficient, p_w^*, and aerodynamic efficiency, η_{ad}, as a function of the flow coefficient ϕ, for several operating conditions.

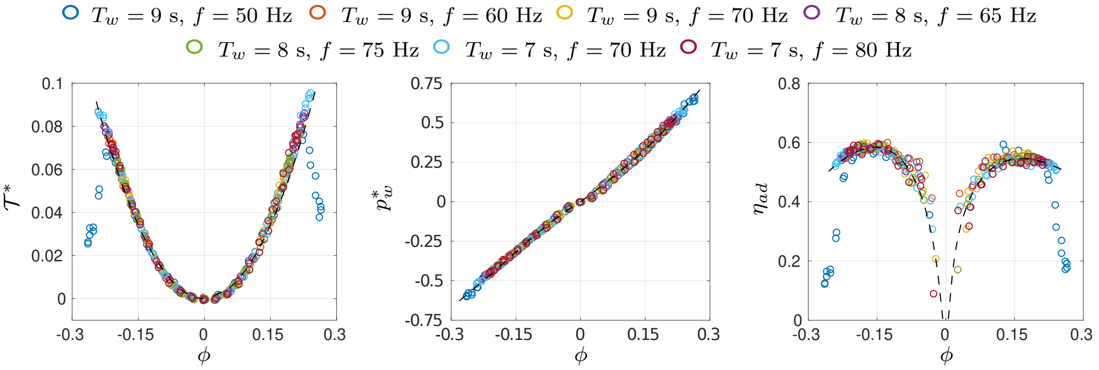

(a) Non-dimensional torque. (b) Non-dimensional wall pressure drop. (c) Aerodynamic efficiency.

Figure 5.6: Non-dimensional performance under non-stationary flow.

As expected, aerodynamic parameters trends clearly show a very good superposition for each flow condition except when the stall occurs. This situation, obtained with a piston period of 9 s and a turbine rotational frequency of 50 Hz, is highlighted by the rapid drop of the torque coefficient and of the efficiency, Figs. 5.6 (a) and (c), respectively. In the operating range where stall does not occur, both the pressure coefficient and the non-dimensional torque increase monotonically with the flow coefficient. Their trends with respect to the flow coefficient, do not significantly change from the ones obtained under stationary flow conditions and reported in Fig. 5.4. No differences can be observed between acceleration and deceleration phases, as well known from literature [132], given the low non-dimensional frequency $(\pi f c)/U$, of about 2.6×10^{-4}. The aerodynamic efficiency, Fig. 5.6 (c), is always positive and reaches its local maximum value for $\phi = \pm 0.15$ which represent the best efficiency condition.

In Fig. 5.7, different working conditions have been compared in terms of the global efficiency, η_g, of the turbine, calculated by considering the measured torque at turbine shaft, see Eqn. (2.2), only compensated with the inertial term.

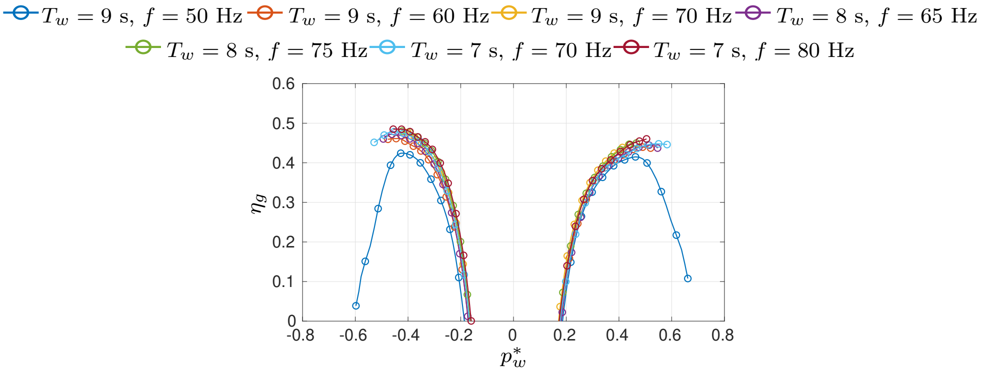

Figure 5.7: Turbine global efficiency for different working conditions.

Global efficiency results show that the pressure coefficient corresponding to the maximum efficiency is substantially in the range between 0.4 and 0.5, as shown in [57].

The measurements used to calculate the turbine global performance reported in Fig. 5.6, were also used to determine the velocity vectors, both at inlet and outlet of the turbine, in order to made the efficiency decomposition as described in Sec. 2. These calculations can be done only for the inflow phase, because the flow coming into the chamber from the outside environment has been experimentally verified to be fully axial [57, 58, 61]. Referring to Fig. 2.3, with $\alpha_1 = 90$ degrees, it is possible to write

$$W_1 = \sqrt{(C_{1z}^2 + U^2)} \tag{5.7}$$

and

$$\beta_1 = \arctan \frac{C_{1z}}{U} \tag{5.8}$$

where the value of U is calculated at turbine mean radius and $C_{1z} \equiv C_1$.

Assuming constant the axial velocity through the rotor, i.e. $C_{2z} = W_{2z} = C_{1z}$, and from the equation of conservation of angular momentum, it is possible to calculate the tangential component of the absolute velocity, as done in Eqn. 5.9.

$$\mathcal{T}_{ad} = \dot{m}r\,(C_{1,\theta} - C_{2,\theta}) \quad \Longrightarrow \quad C_{2,\theta} = \frac{-\mathcal{T}_{ad}}{\dot{m}r} \tag{5.9}$$

where $\mathcal{T}_{ad}$ is the aerodynamic torque, $\dot{m} = \rho Q$ is the mass flow rate and $C_{1,\theta}$ is null when $\alpha_1 = 90°$. Then, the velocity components are directly calculated based on the outlet triangle in Fig. 2.3.

$$C_2 = \sqrt{C_{2z}^2 + C_{2,\theta}^2} \tag{5.10}$$

$$W_{2,\theta} = U - C_{2,\theta} \tag{5.11}$$

$$W_2 = \sqrt{W_{2z}^2 + W_{2,\theta}^2} \tag{5.12}$$

$$\alpha_2 = \pi - \arcsin\left(\frac{C_{2,z}}{C_2}\right) \tag{5.13}$$

$$\beta_2 = \arcsin\left(\frac{C_{2,z}}{W_2}\right) \tag{5.14}$$

The reconstruction of the flow field from the global measurements, although is possible only for the inflow phase, is useful to give an approximate characterization of the flow through the turbine. Flow characteristics can be also used to estimate losses inside the turbine and its aerodynamic performance (see Sec. 2.3).

In Fig. 5.8, absolute and relative flow angles, α and β, respectively, are shown as a function of the non-dimensional piston position Z^*, defined as follows

$$Z^* = \frac{Z - Z_{min}}{Z_{max} - Z_{min}} \tag{5.15}$$

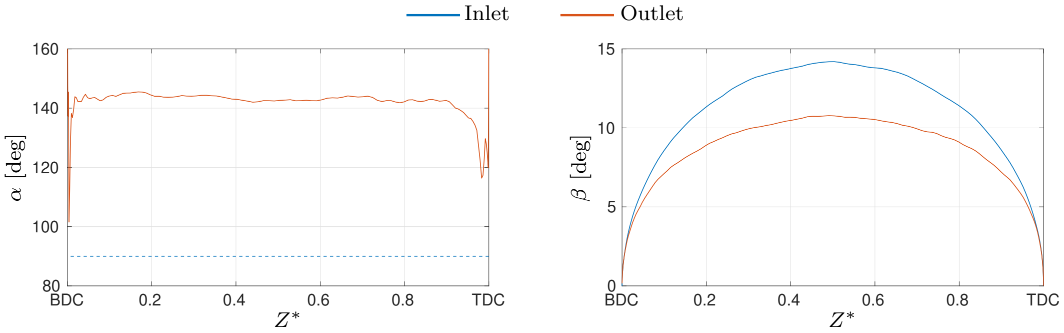

(a) Absolute flow angles.

(b) Relative flow angles.

Figure 5.8: Flow angles calculated from global measurements.

Flow angles calculations show an almost constant direction of the absolute velocity vector during the whole inflow phase, both at turbine's inlet and outlet. As expected, relative flow angles vary with an almost parabolic distribution accordingly to the piston sinusoidal motion. Incidence and deviation angles are very small, below 15 degrees in the non-stalled operating range, which is a characteristic of the Wells rotor cascade.

Starting from velocity vectors calculations, it is possible to calculate the loss components, in terms of the rotor loss coefficient ξ_R and the exit kinetic energy loss coefficient ξ_{EX}, for the inflow phase. In Fig. 5.9 (b) is reported the relative contribution of loss components on efficiency as a function of the velocity coefficient λ, while Fig. 5.9 (a) shows the values of the relative velocity reduction coefficient ψ (see Sec. 2.3) with respect to the flow coefficient ϕ.

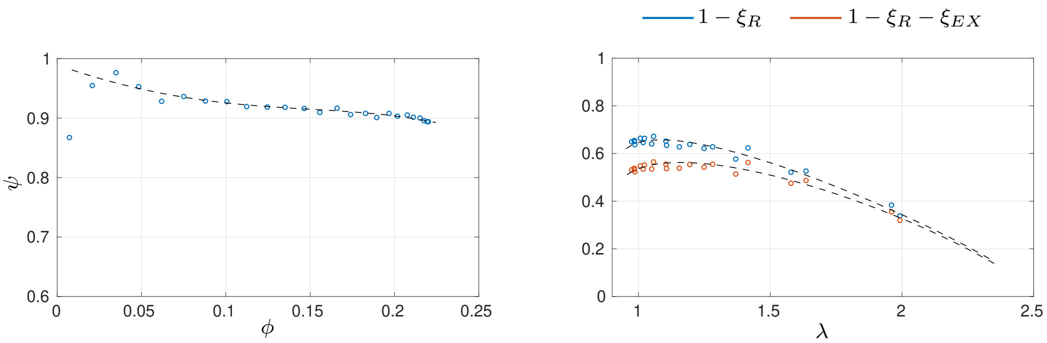

(a) Reduction coefficient of the relative velocity.

(b) Losses components.

Figure 5.9: Loss components and velocity reduction coefficient.

Figure 5.9 (a) shows a slow change with ϕ of the rotor's velocity reduction coefficient, except near the inversions of piston motion, i.e. for small values of ϕ. This result is very important to correctly read rotor losses values in Fig. 5.9 (b). In fact, the almost constant value of the aerodynamic performance of the rotor highlights that non-stationary operating conditions are intrinsically responsible for rotor losses when the turbine works away from its optimal efficiency range, i.e. for high values of λ. The turbine rotational speed could be controlled in order to keep operating conditions closer to the maximum efficiency. Finally, Fig. 5.9 (b) makes evident the relative importance of the two contributions of losses, thus clarifying that the losses in the Wells turbine are mainly due to the rotor losses, and only a relative small amount of losses could be related to the exit kinetic energy.

5.3.2 Local measurements and performance

The local flow field has been characterized by means of a 4-holes probe, designed and built for the DIMCM's OWC setup with Wells turbine. A schematic view of the "wedge" probe is shown in Fig. 5.10 with a definition of the flow planes considered for probe measurements.

The probe's head has a maximum dimension in the radial direction of about 2.5 mm, thus allowing a fine scan resolution along the blade span and to minimize the distortion of the flow field, considering the small blade height of the turbine. The aerodynamic probe has been used in "non-nulling" mode within its angular calibration range, in order to determine the flow angles and total and static pressures. Probe orientations have been selected accordingly to the expected flow directions both at the inlet and at the outlet of the turbine, by rotating the stem probe around its axis. The angular calibration has been conducted in a subsonic wind tunnel, by relating the pressures measured by the probe holes indicated in Fig. 5.10 with the true values, i.e. the total pressure p_t and the static pressure p, to the flow angles,

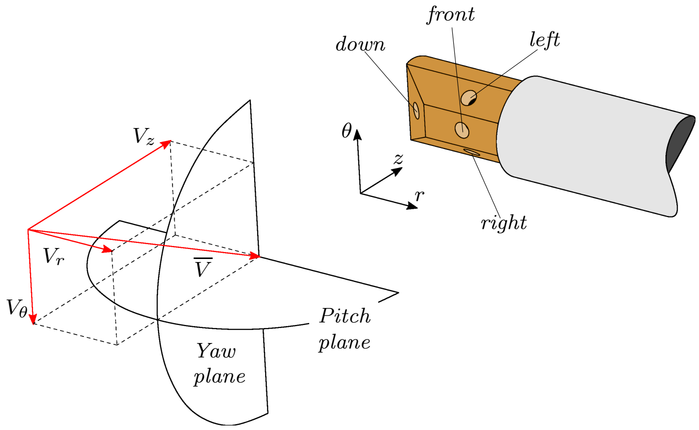

Figure 5.10: Schematic view of the “wedge” probe.

as follows:

$$\begin{aligned} k_Y &= \frac{p_{left} - p_{right}}{q_{ref}} \\ k_P &= \frac{p_{up} - p_{down}}{q_{ref}} \\ k_T &= \frac{p_t - p_{front}}{p_t - p} \\ k_S &= \frac{p - p_s}{p_t - p} \end{aligned} \tag{5.16}$$

where k_Y, k_P, k_T and k_S represent the yaw coefficient, the pitch coefficient and the total and static pressure coefficients, respectively; p_{up} is calculated by averaging *left* and *right* pressures, i.e. $p_{up} = (p_{left} - p_{right})/2$; p_s represents the “static pressure” of the probe, obtained as $(p_{down} + p_{left} + p_{right})/3$ and q_{ref} represents the “dynamic pressure” of the probe, calculated as $p_{front} - p_s$. The schematic representation in Fig. 5.10 shows probe’s taps and their names, making evident the directional taps, i.e. *down*, *left* and *right* taps, and the total pressure tap namely as *front*.

The calibration coefficients defined in Eqn. (5.16) are shown in Fig. 5.11 as the contour plots of their values evaluated during the calibration process.

The probe has been also characterized for its walls proximity effects (see App. B), that have been evaluated from testing in a subsonic wind tunnel and applied to correct the measurements performed near the walls in the Wells turbine.

Measurements uncertainties have been evaluated with the well known uncertainty propagation method (UPM) [160]. The uncertainties on calibration coefficients k_Y, k_P, k_T and k_S have been estimated from the calibration process, as done by [161]. The uncertainties of the interpolation process used to determine the probe angles, i.e. yaw and pitch, lead to a maximum error on both yaw and pitch angle of ±0.5 degrees. Consequently, total and static pressure have shown a maximum deviation of about ±15 and ±20 Pa, respectively. The differential measurement of directional signals, i.e. $p_{left} - p_{right}$ for the yaw angle and $p_{up} - p_{down}$ for the pitch angle, has been

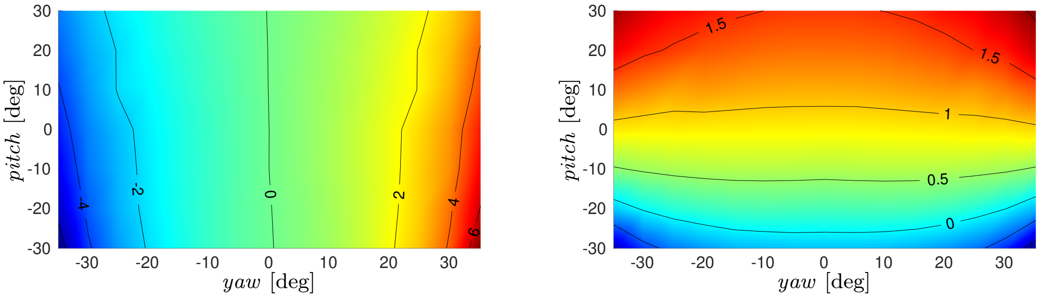

(a) Yaw coefficient.

(b) Pitch coefficient.

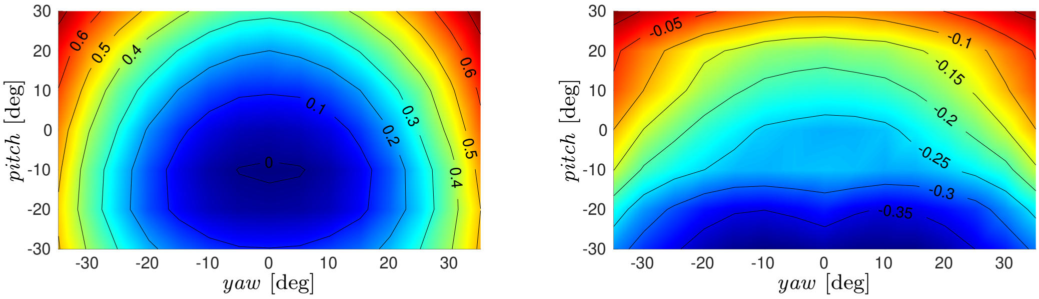

(c) Total pressure coefficient.

(d) Static pressure coefficient.

Figure 5.11: Non-dimensional calibration coefficients for the “Wedge” probe.

preferred to their single gauge measurement in order to minimize the uncertainty in the determination of the flow angles, as demonstrated in [161].

The “wedge” probe has been used to investigate both the inlet and outlet flow, by taking pressure measurements at a distance of 15 mm in the axial direction from the turbine plane, both at ambient and piston side. The blade span has been scanned at 18 radial positions, not equally spaced: smaller steps, less than 1 mm, have been taken near the walls where larger gradients of pressure were expected. Local measurements have been performed under non-stationary flow conditions, as done for global measurements. All the settings used for the experiments are listed in Tab. 5.3.

Table 5.3: Settings for local investigations.

Turbine rotational frequency, f	70 Hz
Piston stroke amplitude	$\approx$ 700 mm
Piston period, T_w	7 s
Maximum flow coefficient, ϕ	0.195
Reynolds’ number of the outlet flow based on blade chord	$\approx 1.53\times10^5$

The value of the piston period has been chosen to obtain high levels of signals, both for torque and pressure measurements; turbine rotational frequency has been selected to obtain a maximum flow coefficient of about 0.2, in the free-stall operating range. The acquisition time for each probe position has been set to record signals, including global measurements, for at least 5 piston periods.

Inlet flow

A preliminary investigation of the inflow phase has been conducted in order to characterize its boundary layer, by measuring the total pressure along the blade span with a very small flattened probe (nose radial dimension equal to 0.35 mm). Measures have been taken only at ambient side, i.e. during the inflow phase, for which the axial nature of the flow has been demonstrated in [61]. The probe has been placed about 1 chord upstream the rotor and the total pressure has been measured at 32 radial positions, with a detailed refinement in the near-walls regions. The static pressure, detected with the wall taps, placed on the same rotor side, has been coupled with the total pressure from the probe in order to calculate the boundary layer profile. Figure 5.12 shows the boundary layer profile, as a function of the non-dimensional radial position r^*, see Eqn. (5.17), in terms of the absolute velocity C non-dimensionalized with respect to the undisturbed mean velocity C_{ref} (outside the boundary layer).

$$r^* = \frac{r - r_{hub}}{r_{tip} - r_{hub}} \tag{5.17}$$

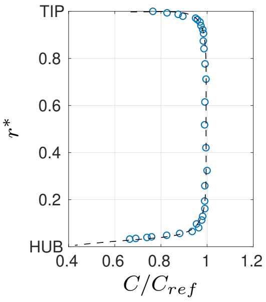

Figure 5.12: Non-dimensional velocity distribution along the blade span for the maximum flow coefficient.

The traverse measurements clearly show a very thin boundary layer, both near tip and hub walls, with a maximum thickness of $10 \div 15\%$ of the blade height.

Velocity components and flow angles at turbine's inlet, measured with the "wedge" probe placed at the blade midspan, are shown in Figs. 5.13, for both inflow and outflow phase.

As expected, a parabolic distribution of the axial velocity is obtained during both the inflow and the outflow phase, with very close values between the two phases. The

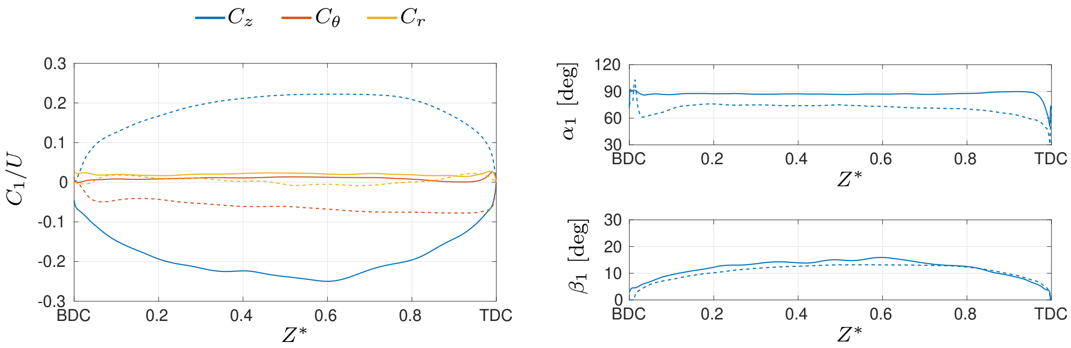

(a) Components of absolute velocity.

(b) Flow angles.

Figure 5.13: Velocity components and flow angles at turbine's inlet, for the inflow (solid line) and the outflow phase (dashed line), measured at blade midspan, as a function of the piston position.

small tangential velocity component at turbine's inlet during the inflow phase can be attributed to the potential effect induced by the rotor, while it is more pronounced during the outflow phase, because the swirl component of the previous inflow phase persists inside the chamber, as demonstrated in [57,58]. Similarly, the absolute flow angle α_1 confirms a substantially axial flow at the inlet during the inflow phase, and a value of α_1 smaller than 90 degrees during the outflow phase, in agreement with the presence of the swirl component. The axial flow direction at turbine's inlet does not significantly change during the whole period of both the inflow and the outflow phase, meaning that the swirl component is not dissipated as the flow rate grows. A small radial velocity component has been detected during both the two phases, due to the stronger blockage effect at the hub of the rotor where the solidity is higher. This determines a deviation of the flow from the hub to the tip. The angle of incidence, β_1, which corresponds to the relative flow angle, does not change significantly between the two phases and it maintains a parabolic distribution with a maximum value around 15 degrees. Lower values have been measured during the outflow phase as the swirl component determines a reduction of the flow incidence on the blade.

Velocity components and flow angles at turbine's inlet along the blade span, are shown in Fig. 5.14 for the maximum flow coefficient.

The inlet flow, during both the inflow and the outflow phase, shows an almost uniform distribution along the blade span except in proximity of the hub and tip regions. The tangential component, during the outflow phase also shows a linearly increasing value along the span, from the hub to the tip. This means that the swirl component, due to the previous phase, is not constant along the blade span so that the absolute flow angle α_1 slightly varies from the hub to the tip. Also the angle of incidence β_1 shows a trend with values that decrease moving from the hub to the tip during both the two phases, but it can be mainly attributed to the variation of

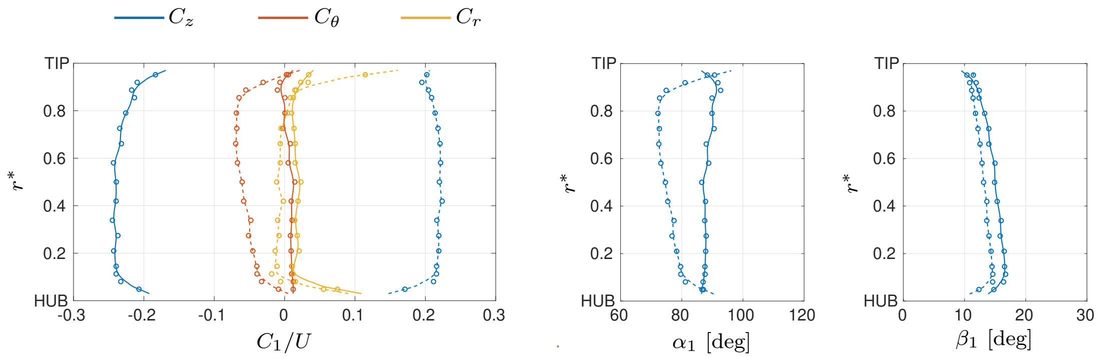

(a) Components of absolute velocity. (b) Flow angles.

Figure 5.14: Velocity components and flow angles at turbine's inlet, for the inflow (solid line) and the outflow phase (dashed line), measured along the blade span for the maximum flow coefficient.

the peripheral velocity with the rotor radius. During the outflow phase, the angle of incidence along the blade span is always lower than that measured during the inflow phase, and this is due to the presence of the swirl component, that explain the different performance between the two phases as the aerodynamic load on the rotor is reduced.

Outlet flow

Figure 5.15 shows velocity components and flow angles at turbine's outlet, measured at the blade midspan, during both inflow and outflow phase, as a function of the non-dimensional piston position Z^*.

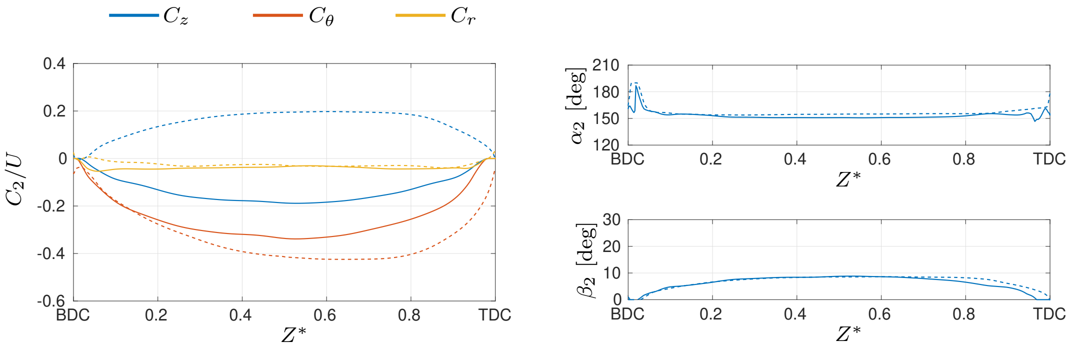

(a) Components of absolute velocity. (b) Flow angles.

Figure 5.15: Velocity components and flow angles at turbine's outlet, for the inflow (solid line) and the outflow phase (dashed line), measured at blade midspan, as a function of the piston position.

The outlet flow is characterized of higher negative values of the tangential velocity component, see Fig. 5.15 (a), in agreement to the work exchanged by the rotor

(Euler equation), while the axial component is similar in trend and intensity to the one measured at the rotor inlet, as the flow rate through the turbine is conserved. Radial components of velocity are very close to the ones measured at turbine's inlet, both for the two phases. Outlet flow angles, Fig. 5.15 (b), are almost overlapped for the two phases, with a nearly constant value of the absolute flow angle α_2 and a parabolic distribution of the relative flow angle β_2 during both the inflow and the outflow phase.

Measurements of velocity components and flow angles at turbine's outlet along the blade span, are shown in Fig. 5.16 for the maximum flow coefficient.

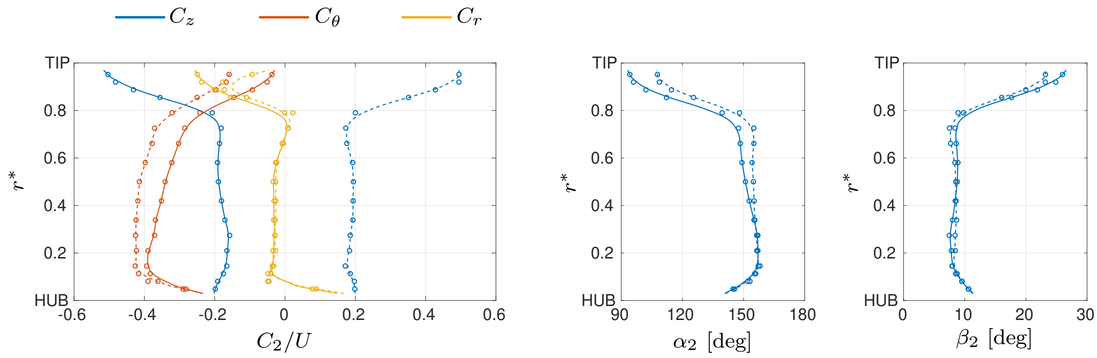

(a) Components of absolute velocity. (b) Flow angles.

Figure 5.16: Velocity components and flow angles at turbine's outlet, for the inflow (solid line) and the outflow phase (dashed line), measured along the blade span for the maximum flow coefficient.

As expected, velocity components and flow angles are very similar during the two phases, with only small differences. The effect of the tip leakage acts for a relevant portion of the blade span, as demonstrated by the strong reduction of the tangential component above the $70 \div 80\%$ of the blade span.

Local performance

Local performance of the turbine are here described in terms of the loss parameters ξ_R and ξ_{EX}, and by using two additional non-dimensional performance coefficients described in Ch.2, i.e. the reduction coefficient of the relative velocity, ψ, and the work coefficient, Λ. These last two dimensionless coefficients are reported in Figs. 5.17 (a) and (b), respectively, as contour plots, as a function of the piston position Z^* and of turbine radius r^*.

As expected, performance parameters, ψ and Λ, calculated for the two phases, show similar distributions and very close values. Slightly higher values of ψ during the outflow phase, can be attributed to a different incidence angle that determines higher aerodynamic performance and then a higher output work, while the work coefficient Λ do not present significant differences between the two phases. Both the two phases are characterized by an almost constant value of the reduction coefficient

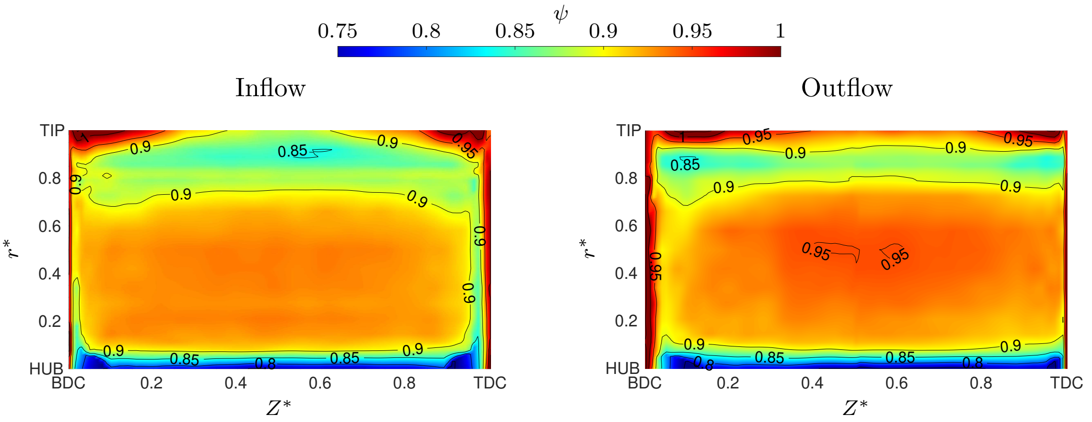

(a) Reduction coefficient of the relative velocity.

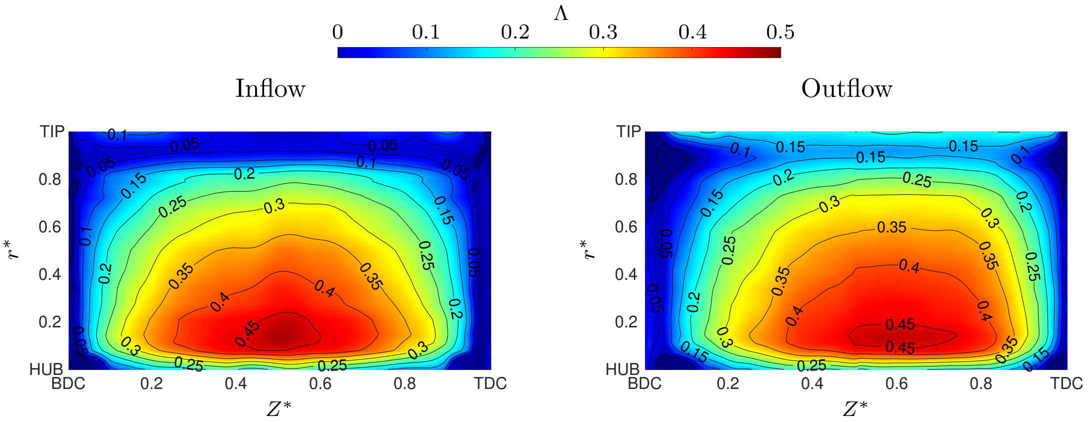

(b) Work coefficient.

Figure 5.17: Contour plots of the performance parameters for the two phases.

for a fixed radial position and different flow conditions: the best performance are recorded in the central region of the blade span, while the high solidity at the hub and the leakage flow at the blade tip, are responsible of poor aerodynamic performance near walls. The work coefficient of the turbine makes evident the regions of the highest work exchanged. The dependency of the work coefficient from the flow conditions is made evident in Fig. 5.17 (b), where the highest values of Λ are located around $Z^* = 0.5$, for both the two phases, at the highest flow rate. More quantitative considerations can be drawn by looking at plots in Figs. 5.18 (a) and (b).

Performance parameters ψ and Λ, Figs. 5.18 (a) and (b), respectively, have been reported for three different flow conditions during the accelerating phase, both for the inflow and outflow, as a function of the non-dimensional radial position r^*. It is interesting to note that for the same flow coefficient ϕ, based on the axial velocity of the inlet flow, turbine performance are not perfectly overlapped between the two phases. This is due to the presence of a swirl velocity component at turbine's

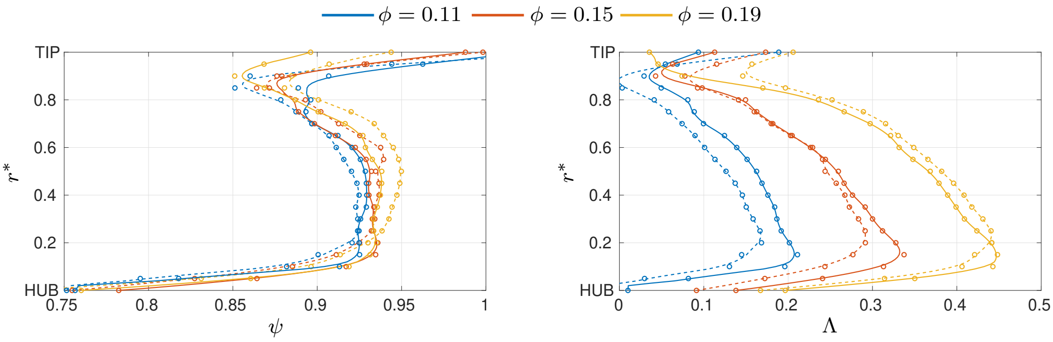

(a) Reduction coefficient of the relative velocity.

(b) Work coefficient.

Figure 5.18: Performance parameters for the inflow (solid line) and the outflow phase (dashed line), calculated along the blade span for three flow coefficients.

inlet only during the outflow phase which is responsible of lower aerodynamic blade loads. This effect is deleterious at low flow coefficients, as the incidence on the blade decreases, but it is helpful at the highest flow coefficients as the rotor is at his stall limit and aerodynamic performance are starting to decrease. In fact, at the maximum flow condition, i.e. $\phi = 0.19$, the reduction coefficient ψ is higher during the outflow phase than the inflow phase, as shown in Fig. 5.18 (a).

Similarly to representations of Fig. 5.17, Figs. 5.19 (a) and (b) shows the contour plots of loss components ξ_R and ξ_{EX}, respectively.

Rotor losses, Fig. 5.19 (a), show a declining trend with the flow coefficient, making evident that ξ_R takes into account not only aerodynamic performance, i.e. ψ, but also flow conditions. Their values are very close for the two phases, although slightly lower values have been calculated during the outflow phase, as a result of a lower aerodynamic load on the blades. The trend of ξ_R with the turbine's radius highlights again the effect of the tip leakage, which determines higher losses in a significantly wide portion of the blade height.

Exit losses, Fig. 5.19 (b), are characterized by a smooth variation with the non-dimensional piston position, as expected as the flow speed grows, thus the outlet kinetic energy. This effect is strongly emphasized in the tip region, again due to the leakage flow for which the highest velocities were expected.

On average, losses decomposition gives a comprehensive understanding of the behavior of the tested Wells turbine: the relative low solidity affects the flow field, that could be considered almost well organized and clean for about the 70% of the blade height. This result can be compared to what obtained for the high solidity Wells turbine tested in [61], for which the flow near the hub was more influenced by the higher solidity. On the other hand, the tip leakage affects the remaining portion of the blade height, thus drastically reducing performance at the highest radii. A reduction of tip gap size can be useful to mitigate this effect, coupled with a reduction of turbine *hub-to-tip ratio*, in order to reduce the relative effect of the

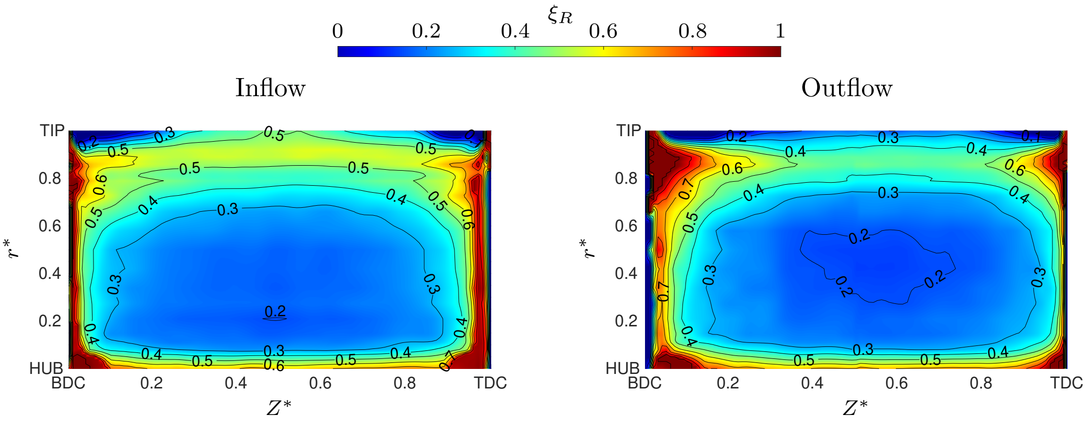

(a) Rotor losses.

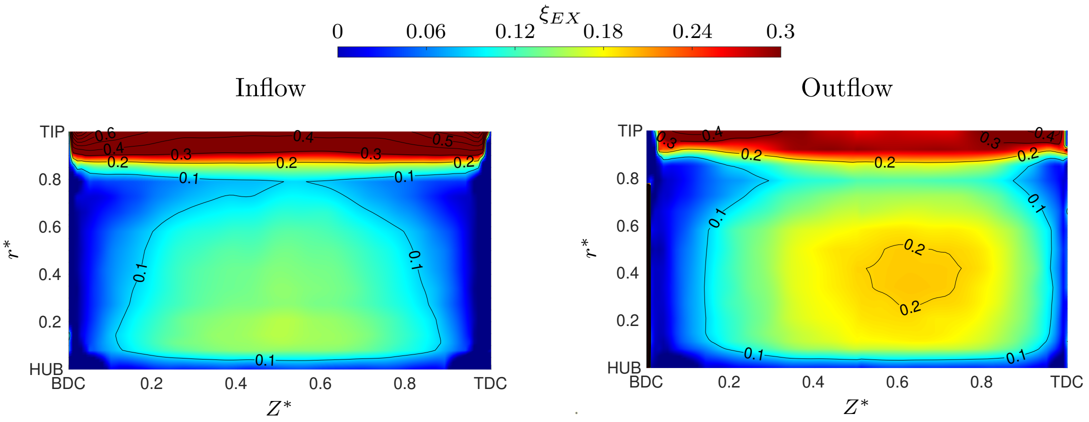

(b) Exit losses.

Figure 5.19: Components of losses of the turbine during both the two phases.

vortices that have been observed at the tip.

5.4 Measurements with the HWA probe

In order to deeply understand the behavior of the local flow field described with the "wedge" probe in Sec. 5.3.2, a more detailed investigation of the mean flow field downstream of a blade vane has been carried out. A hot-wire-anemometer (HWA) probe has been selected for the aim of the investigation, due to its lower intrusion and to its high frequency response. Only the downstream flow during the outflow phase has been reconstructed, as no significant variations have been observed between the two phases (see Sec. 5.3.2).

A slanted miniaturized HW probe has been adopted for the measurements, i.e. the DANTEC type 55P12. It is schematized in Fig. 5.20 (a), while its positioning in the test rig downstream of the rotor is represented in Fig. 5.20 (b). The sensor has been placed at an axial distance from the blade chord of 5.5 mm.

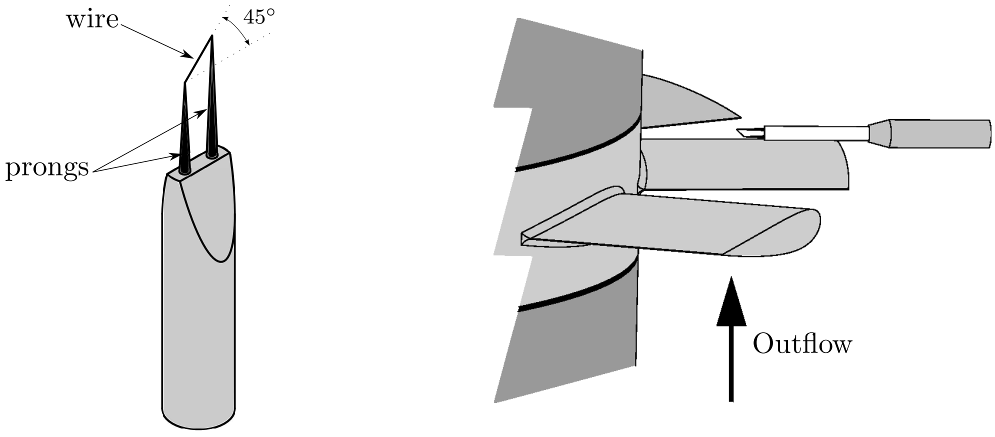

Figure 5.20: Schematic view of the DANTEC 55P12 HWA probe and its positioning near the rotor.

The rotating slanted HW technique [162–164], also known as multi-rotation technique, has been adopted for the reconstruction of the flow field. It allows the measurement, in a given steady or periodic flow field, of the three components of the mean flow velocity and the six components of the Reynolds stress tensor. Its main advantage [165] is that it uses only probes with one sensor, thus reducing flow distortions due to probe size. For the calculation of the three components of the mean flow velocity, at least three independent information, provided by HW measurements, are necessary. More than three different measurements are used, in order to reduce the error associated with data reduction, thus requiring to solve a overdetermined system of equations. Independent measurements are obtained performing different orientations of the sensor, by rotating the probe around its stem.

The probe calibration has been conducted in order to obtain a relation between electric signal and flow velocity and to establish the angular sensitivity. An open wind tunnel has been used [164, 166, 167] for these calibrations, using a motorized system to rotate the probe with respect to the yaw and the pitch plane. The well known King's law [168] can be used for velocity calibration, in order to relate the voltage measured from the sensor, E_i, and the effective cooling velocity of the wire, V_F:

$$E_i^2 = E_0^2 + B\, V_F^n \tag{5.18}$$

The relation between V_F and E_i, in this case, has been represented with a fourth degree polynomial equation, thus giving a better approximation and reducing uncertainties respect to the inversion of the King's law, as demonstrated in [166].

The angular calibration has been performed under a constant flow speed, in order to use the modified Jørgensen's law [169] to relate the velocity components, in the sensor's reference system (n-t-b), with the effective cooling velocity:

$$V_F^2 = K_N C_N^2 + K_T C_T^2 + K_B C_B^2 \tag{5.19}$$

where subscripts N, T and B are referred to the normal, tangential and binormal direction, respectively, for which coefficients K_N, K_T and K_B are the sensitivity coefficients in those directions. In Fig. 5.21, are reported the angular calibration curves in the form of the contour plot of V_F non-dimensionalized with respect to the flow speed V_{ref}, as a function of yaw and pitch angles.

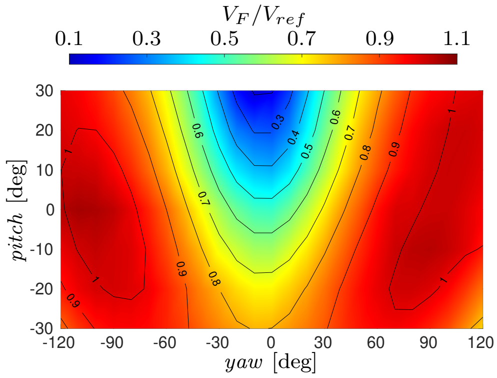

Figure 5.21: DANTEC 55P12 angular calibration.

Probe symmetry is clearly evident with respect to the yaw angle, while the wire inclination and the different prongs' length are responsible of the non-symmetric behavior of the sensor with respect to the pitch angle. In order to Eqn. (5.19) can correctly represent the angular response of the HWA, the directional sensitivity coefficients, K, have been considered dependent on the pitch and yaw angles, and not constant as originally proposed by Jørgensen.

Uncertainties in HW measurements have been estimated following [166], by taking into account: a) errors introduced in the calibration process and related to the measurement of the flow speed and the angles of rotation; b) the uncertainties in the polynomial expression used to approximate the calibration curve; c) the uncertainties in the calculation of the velocity components in the sensor's reference system. In Tab. 5.4 are reported the overall uncertainties of the measurements performed with HW probe.

Table 5.4: Hot-wire probe uncertainties.

Mean velocity	±2.5%
Flow angle	±2 deg
Probe alignment	±0.1 mm

Steady flow conditions, required to use the multi-rotation technique, have been realized by reproducing a triangular piston motion in the OWC simulator. The main parameters used for the tests are reported in Tab. 5.5.

Table 5.5: Settings of HWA tests.

Turbine rotational frequency, f	50 Hz
Piston stroke amplitude	≈ 850 mm
Piston period, T_w	9 s
Reynolds' number based on blade chord and on the outlet relative velocity	$\approx 1.28\times10^5$
Sampling rate	100 kHz

The piston displacement is similar to the one used for tests in Sec. 5.2 (see Fig. 5.3), with a constant piston speed during each ramp that determines a flow coefficient of about 0.2, very close to the maximum value reached under non-stationary conditions, as described in Sec. 5.3.2. By fixing a period of 9 seconds, the flow can be considered steady for at least 3 seconds during each ramp, which ensures about 150 rotor revolutions with a rotational frequency of 50 Hz. Rotor revolutions have been counted with a additional encoder, that has been used as a trigger signal during the phase averaging of sensor's signal. The sampling rate of 100 kHz allows to take at least 150 measurements along one blade pitch.

The blade height has been discretized by radially positioning the HW probe at 20 stations, not equally spaced: smaller steps have been taken where larger gradients were expected. For each radial position, signal acquisition have been done at 5 angular positions, in order to ensure a overdetermined system of equations for flow reconstruction. The reconstruction procedure leads to the determination of the mean flow components $\overline{C_i}$, knowing the effective cooling velocities V_F [167,170], and the angular orientations of the probe, with respect to the rotor reference system of coordinates:

$$V_F^2 = \sum_{i=1}^{3}\sum_{j=1}^{3} A_{ij}\overline{C_i C_j} \tag{5.20}$$

where the coefficients A_{ij} are a function of the directional sensitivity coefficients K and of the probe orientations. The solution of the overdetermined system of non-linear equations, Eqn. 5.20, is done following an iterative procedure where also the variations of K coefficients with probe orientation were taken into account.

Turbulence intensity of the inlet flow

Before to present the analysis of the flow field downstream the rotor, the HW sensor has been used to characterized the inlet flow in terms of its turbulence intensity, Tu. This measure, carried out both for the inflow and outflow phase, has been taken only at the mean radial position, by placing the probe 1 chord upstream the rotor, in order to reduce as much as possible the potential effect of the rotor on the measures.

The piston motion was set to linear, ensuring a almost constant flow coefficient at $\phi = 0.2$.

The HW sensor has been placed normal to the inlet flow direction, and measurements were taken only for this condition. Thus, the turbulence intensity is evaluated on the measured effective cooling velocity [171], which corresponds to the intensity of the flow velocity:

$$Tu = \frac{\sigma_F}{\overline{V_F}} \times 100 \tag{5.21}$$

where σ_F is the root-mean-square of the fluctuating component of V_F and $\overline{V_F}$ is its mean value after the phase averaging process based on the rotational frequency of the rotor.

In Fig. 5.22 the turbulence intensity Tu is reported for both the two phases, as a function of the non-dimensional blade pitch s/t_b.

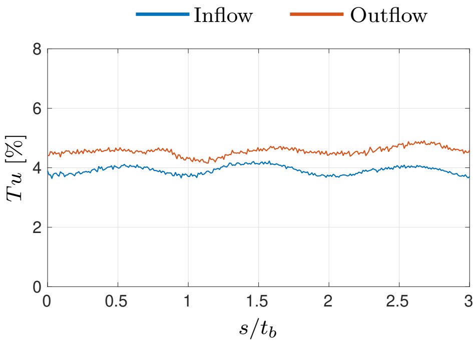

Figure 5.22: HW measurements of turbulence intensity upstream the rotor, during both the inflow and the outflow phase, as a function of the non-dimensionalized blade pitch.

The potential effect of the rotor is still detected by the sensor and it is responsible of oscillations in the acquired signals, although they could be neglected, due to their small amplitude. Calculations of turbulence intensity show only small differences between the two phases, with slightly higher values during the outflow phase, probably due to the turbulence level of the outlet flow from the previous phase that was not dissipated inside the chamber. A turbulence intensity for both the two phase can be assumed equal to 4%.

The flow field downstream the rotor

Contour plots of relative velocity components non-dimensionalized with respect to the rotor tip velocity, are reported in Figs. 5.23 (a), (b) and (c), for two blade pitches.

The superposition of blades outline in Figs. 5.23 is useful in order to better understand the velocity distributions determined by a Wells turbine rotor, which, as described, is quite different from the typical configurations of axial turbines. The

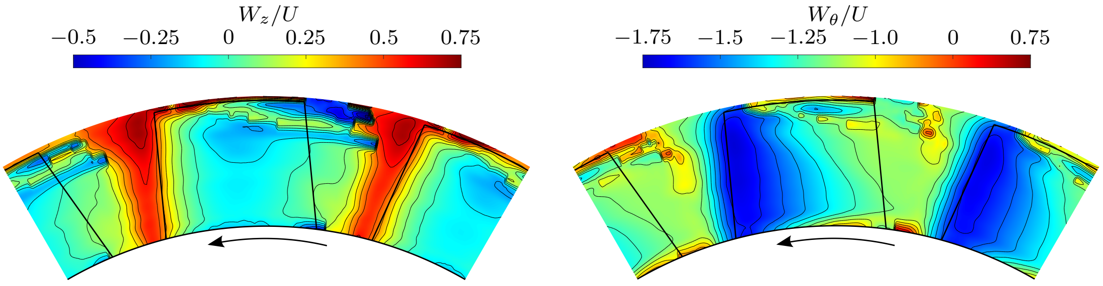

(a) Axial velocity component. (b) Tangential velocity component.

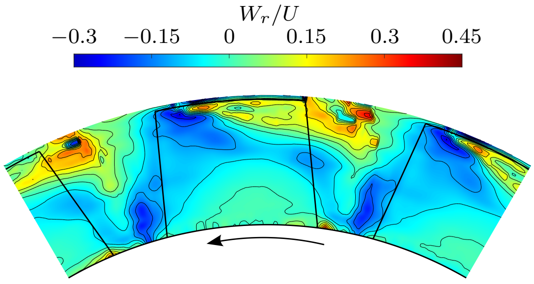

(c) Radial velocity component.

Figure 5.23: Contour plots of relative velocity components downstream the rotor, in two adjacent blade vanes.

stagger angle of 90 degrees, typical of the symmetrical profiles of the Wells turbine, strongly affects the velocity distribution downstream of the rotor cascade, which modifies the classic perception and interpretation of the flow. From the maps of the axial component, W_z, it can be observed that the wake region is not immediately identifiable for the uncommon Wells rotor. In fact, the greater velocity gradients, that usually characterize the blade wakes, are in this case placed near the leading edge of the blade profile. In this region, the highest values of the velocity components were also measured. This is a consequence of the strong blockage effect, exerted by the rotor blades, and by the proximity of the measurements points to the suction side of the profile, that sees the flow near both the trailing edge and the leading edge. The mass flow is forced to pass through the space in between to adjacent blades, thus a jet is observed close to the leading edge, while the wake detached from the trailing edge of the adjacent blade is altered. Most of the pitchwise axial velocity distribution is affected by the flow along the blade suction side that shows low values, close to zero. Near the tip region, especially in the region between the blades, values of negative axial velocity are observed due to the presence of the leakage vortex, which takes up a wide portion of the blade vane.

The radial velocity component, W_r, shows smooth gradients from midspan to both the walls. In the tip region, higher values of radial velocity and strong gradients are detected, due to the leakage flow. From Fig. 5.23 (c), it can be seen how this region develops from the leading edge of the blade and radially expands as it moves downstream, reaching almost the 30% of the span from the tip of the blade. In the the hub zone, close to the blade trailing edge, there is a small region characterized by a high value of the radial velocity as well as tangential and axial velocities, probably due to the secondary flow originates from the interaction of the wall boundary layer with the wake.

The tangential velocity component, W_θ, appears to be always negative, as expected, and smoothly variable from the leading edge to the trailing edge, while positive values are present in very small regions, where the vortices are expected.

The radial distribution of the absolute mean velocity components are shown in Fig. 5.24, as a function of the non-dimensional radius. These distributions have been obtained by mass-weighted averaging the velocity components in the circumferential direction.

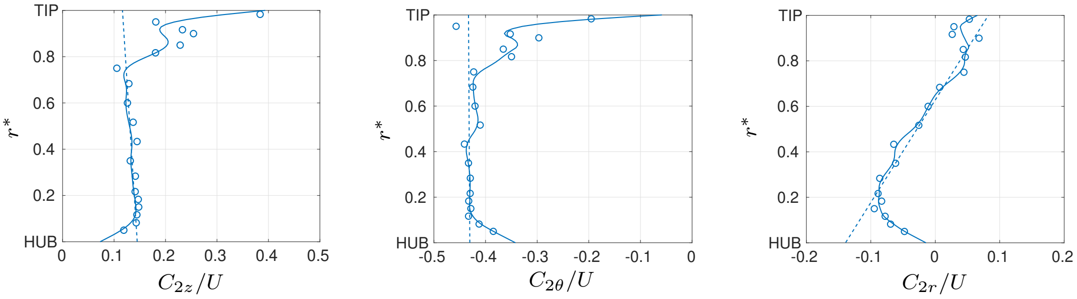

(a) Axial velocity. (b) Tangential velocity. (c) Radial velocity.

Figure 5.24: Velocity components of the absolute flow and their extrapolated mean values (dashed line) as a function of the non-dimensional radius.

The radial distribution of the axial velocity component, C_z, is characterized by an almost constant value, for $70 \div 80\%$ of the blade span. High gradients appear in the tip region, due to the presence of the leakage flow that affects for at least $20 \div 30\%$ of the blade span. This effect can be appreciated also by observing the radial distribution of the tangential component C_θ, while it appears less evident for the radial component C_r. The latter, shows a smooth gradient from the hub to the tip which means that the flow is moving from higher to lower radii, while this trend is overturned in the upper part of the blade height. Although unexpected, this trend of the radial component can be justified considering that the blockage effect at the hub and the leakage flow at the tip, considerably reduce the height of the blade channel in which the clean flow can pass through. These effects reduce, and the distribution appears smoother, at a greater axial distance downstream of the rotor depending on the intensity of the vortices, because the flow tends to occupy more uniformly the whole annulus area.

In Fig. 5.24 are also reported (dashed lines) the radial distributions of the mean values measured in the midspan region and linearly extrapolated in the wall regions to eliminate the effects of the secondary flows.

Another way to examine the flow field comes from a kinetic energy point of view, by introducing the kinetic energy defect ζ_D [167]:

$$\zeta_D = \frac{W^2 - W_{ref}^2}{W_{ref}^2} \tag{5.22}$$

where W_{ref}^2 is the reference axisymmetric flow, obtained from the mass-weighted averaged distribution of the velocity components which are linearly extrapolated in the hub and tip regions. The contour plot of the defect of kinetic energy is shown in Fig. 5.25.

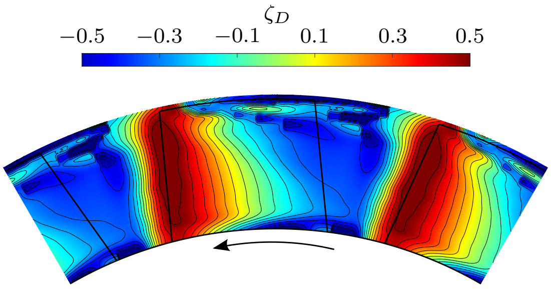

Figure 5.25: Kinetic energy defect.

The contours of kinetic energy defect show high levels of kinetic energy at the leading edge of the blade, thus confirming the presence of a jet which interferes with the wake detached from the trailing edge, pointed out with low levels of ζ_D, that characterize the region downstream the blade. Low values of kinetic energy are also observed at most of the circumferential positions due to the flow leaving the blade suction side. High values of the kinetic energy defect can be seen also in an extended region at the blade tip, where the leakage vortex develops, thus affecting the whole suction side of the blade and the downstream area.

Chapter 6

Solutions to improve Wells turbines performance

As mentioned in the Introduction (Ch. 1), many authors have oriented their studies in researching solutions to improve the performance of the Wells turbine under non-stationary air-flow conditions. From the experimental results presented in Ch. 5, it is possible to drawn two main considerations:

1. The detailed measurements of the flow field, carried out upstream and downstream of the Wells turbine rotor, are particularly useful since they provide important information on its aerodynamic behavior and allow to identify the regions of losses. This information can be suitably used to address changes of the rotor geometry with the aim of improving its aerodynamic performance.

2. Global measurements, carried out in non-stationary flow conditions, have also made it possible to highlight and quantify the extent of the turbine losses, which are particularly influenced by the non-stationary nature of its operation.

In this chapter, two solutions will be presented aimed to improving the turbine performance with the operating conditions, and which therefore concern improvements to only point 2 above.

Experimental investigations reported in Sec. 5.3 have shown that the best performance of the turbine were reached for the maximum flow coefficient before stall limit. Aerodynamic performance are the highest for a value of the flow coefficient lower than the stall limit, but not too far from this one. Thus, considering only the inflow phase, as done for global analyses in Sec. 5.3, the flow coefficient and the angle of incidence at turbine's inlet are linked as follows:

$$\tan \beta_1 = \phi = \frac{C_{1z}}{U} \tag{6.1}$$

This relation, which has been simply drawn from Eqns. (2.1) and (5.8), is valid only when the inlet absolute velocity C_1 is axial. It makes more evident that if you want to obtain a specified value of the flow coefficient, you may act on the rotational speed U or on the flow angle β_1 (considering that C_1 changes with the wave motion and it can be modified with a by-pass valve). Thus, two kind of control actions can be taken:

- the variable speed control of the turbine and
- the variable pitch rotor blades.

List of symbols

	Acronyms
CFD	computational fluid dynamics
OWC	oscillating water column
UDF	user defined function
	Non-dimensional properties
η	efficiency
ϕ	flow coefficient
ψ	reduction coefficient of the relative velocity
p^*	static pressure drop coefficient
$\mathcal{T}^*$	torque coefficient
z	number of blades
	Dimensional properties
α	angle of the absolute flow
β	angle of the relative flow
c	blade chord
C	absolute velocity
E	energy
γ	pitch angle
I_p	polar moment of inertia
k_m	elastic constant
M	pitching moment
Ω	angular rotational frequency
p	static pressure
Q	volumetric flow rate
r	turbine radius
ρ	air density
t	time
$\mathcal{T}$	torque
T_w	wave period, piston period
U	peripheral rotor speed, blade speed
V	velocity
W	relative velocity
ζ_m	damping coefficient
	Subscripts and superscripts
$\overline{(\,)}$	mean value
1	inlet
2	outlet
ad	aerodynamic
d	available
g	global
m	mean turbine radius
opt	optimal
tip	turbine tip
w	wall
z	axial direction

6.1 The variable speed control

Several authors have studied [53, 172–177], mostly with numerical approaches, the performance of speed-controlled Wells turbines during a typical operation of an OWC, i.e. under random waves, in order to avoid stall incoming and to increase the averaged efficiency of the system.

The analysis proposed in the present section aims to experimentally investigate the effectiveness of a speed control strategy, in order to keep the operating conditions closer to the turbine's maximum performance. The investigation has been conducted experimentally, by fixing periodic non-stationary flow conditions (i.e. a sinusoidal piston motion has been applied). Wells turbine performance have been determined from global measurements, and they have been compared with the performance of the non-controlled turbine (under similar operating conditions). Tests have been carried out on the low inertia "modular" Wells turbine presented in Sec. 4.3. The speed control strategy of the turbine has been performed sending a control signal to the inverter that drives the electric motor, in order to set the control law of the rotational speed as a function of the piston position.

The applied control strategy is not based on feedback control mode that uses the rotor speed as feedback signal and the piston position as input signal, in order to evaluate the corrected rotor speed and calculate the signal correction. Instead of this approach, a strategy based on an open-loop control has been preferred for two main reasons: a) to avoid too rapid control actions for the inverter capabilities and maintain the integrity of the torque sensor, that has a maximum operating range of ±2 Nm; b) because a tracking system needs to be correctly adjusted taking into account the natural delay that occurs when the control is based on a non-stationary parameter; the aim of this analysis is to verify the effectiveness of the speed control, not to find the best control approach.

Tests have been conducted in two parts: in the former, the piston position is recorded with the global variables, i.e. the pressure drop through the turbine, the output torque and the rotational speed of the turbine, while the desired law of variation of the rotational speed is calculated based on measured performance parameters; in the second part, the control law is applied to the turbine, when a signal of synchronization, i.e. a trigger, is generated by comparing the first value of the control variable and the piston position.

The period of the piston motion during the tests was 9 s, with a reference turbine speed of rotation of 60 Hz.

The variable used to establish the control law was the non-dimensional wall pressure drop p_w^* for the best efficiency point of the turbine. As shown in Sec. 5.3, the turbine can be characterized in terms of its aerodynamic and global efficiency. Then, maximum values of η_{ad} and η_g have been considered to determine the control law, as shown in Fig. 6.1 (a) where η_{ad} and η_g are the averaged values of the inflow and outflow phases, for a piston period of 9 s and a turbine rotational frequency of 60 Hz, which are reported as a function of p_w^*.

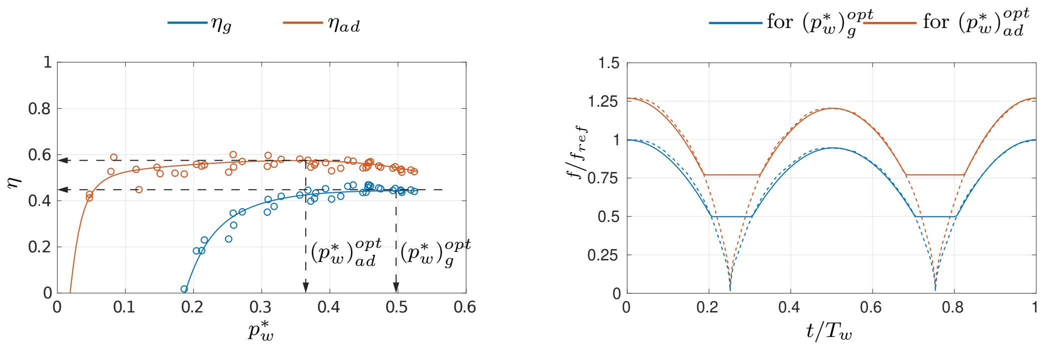

(a) Turbine efficiency.

(b) Theoretic (dashed line) and applied (solid line) laws.

Figure 6.1: Control law for the rotational speed based on the best efficiency condition.

Representations in Fig. 6.1 (a) make clear that both the aerodynamic and global efficiency do not vary significantly under the unsteady flow condition reproduced. More in detail, the aerodynamic efficiency η_{ad} shows an almost constant value of about 0.55 for a wide operating range, i.e. for $p_w^* = 0.1 \div 0.52$. The global efficiency shows a always growing trend with p_w^*, suggesting that for low values of p_w^*, which correspond to low values of the flow coefficient ϕ, the operating condition can be controlled to increase the efficiency. In Fig. 6.1 (a), two different variables of p_w^* for the optimization of aerodynamic and global efficiency can be identified. These variables are used to calculate the time evolution of the rotational speed reported in Fig. 6.1 (b) as a function of the non-dimensional time. The laws have been evaluated based on the definition of the wall pressure drop coefficient in Eqn.(2.1), from which the theoretic rotational frequency is derived as follows:

$$f_{th} = \frac{1}{2\pi}\sqrt{\frac{\Delta p_w}{\rho\,(p_w^*)^{opt}\,r_{tip}^2}} \tag{6.2}$$

where the pressure drop during the period is assumed equal to the one recorded in the reference situation of constant rotational speed. As expected, at the inversions of the piston motion, the requested rotational speed tends to zero (dashed lines in Fig. 6.1 (b)). The law used to control the rotational speed of the turbine approximates the theoretic law with two polynomial curves (solid lines), i.e. one for each phase. The polynomial approximation is obtained by setting a minimum value of the rotational speed compatibly with inverter and torque sensor constraints. The control law is established automatically during the test, with a training period necessary to identify the current operating conditions of the turbine.

Figure 6.2 shows the comparisons of the aerodynamic performance of the rotor subjected to the control laws and with a constant speed of rotation, in terms of reduction velocity coefficient ψ, as a function of the flow coefficient ϕ.

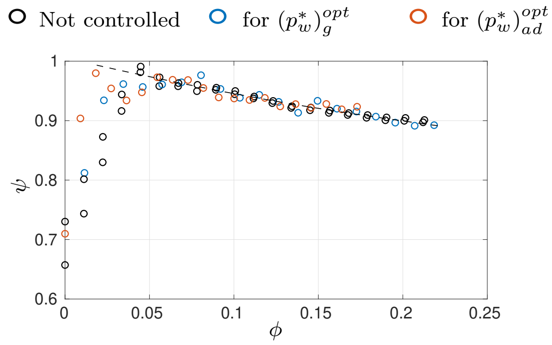

Figure 6.2: Comparison of the velocity reduction coefficient between the controlled turbine (red and blue dots) and the not-controlled turbine (black dots).

This representation makes evident that the instantaneous performance of the rotor do not change with the application of the control law, as they are characteristic of the tested turbine. The relative velocity reduction coefficient shows the same trend with the flow coefficient for every type of control, and only the maximum value of ϕ reached varies with the selected control strategy. The effectiveness of the control solutions is better shown in Figs. 6.3 and 6.4. In Fig. 6.3 the turbine efficiencies for the two control laws are compared to the case of the constant rotor speed, while Fig. 6.4 shows how frequently the different operating conditions (different values of ϕ), assumed by the turbine during a piston period, are occurred.

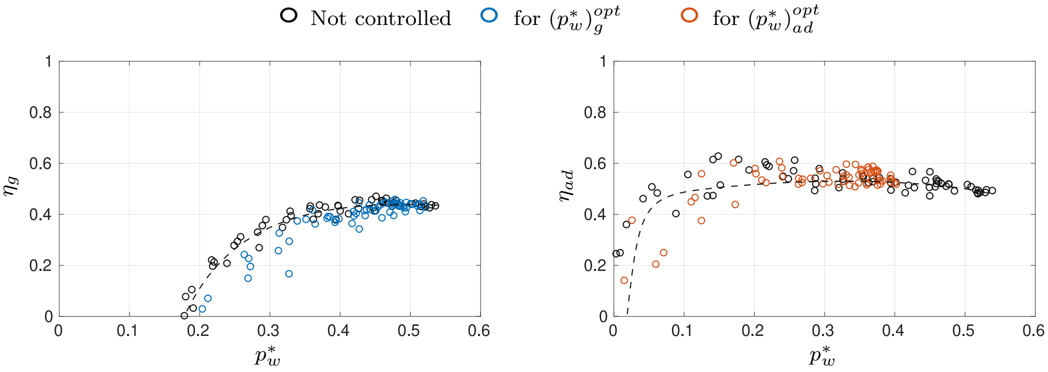

(a) Global efficiency.

(b) Aerodynamic efficiency.

Figure 6.3: Comparison of turbine efficiencies for the two control laws with respect to their uncontrolled values.

It appears clear in Fig. 6.4 that for the two control laws considered, most of the operating conditions are concentrated around the variable value. This is more evident in the control law for $(p_w^*)_{ad}^{opt}$: the working range is maintained for most of the time during the piston period close to the optimum conditions established with the speed control. The graphs in Fig. 6.3 make also evident that the instantaneous performance of the rotor do not change with the application of the control law, as

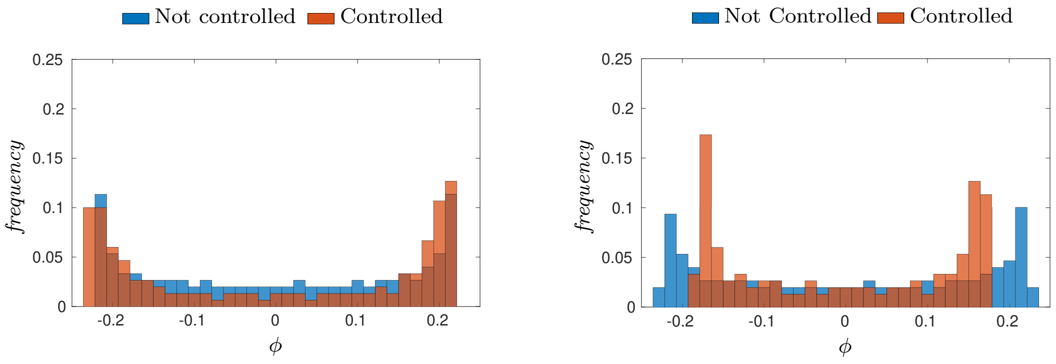

(a) Rotor controlled for $(p^*)_g^{opt}$.

(b) Rotor controlled for $(p^*)_{ad}^{opt}$.

Figure 6.4: Frequency distribution of operating conditions during a piston period for the controlled and the uncontrolled rotor.

they are characteristic of the tested turbine. The performance for controlled and uncontrolled turbines show the same trend with the head coefficient (p_w^*).

From Fig. 6.3, one may observe that the control strategy acts to improve turbine efficiency, both aerodynamic and global, in conditions where the available energy is lower. This means that if efficiency improvements can be obtained mainly for low energetic conditions, the mean efficiency averaged on a cycle will not significantly improve. This consideration will be verified later in the present section.

Flow angles, calculated based on global measurements, for the inflow phase at the mean radius, are compared for the different operating conditions in Fig. 6.5, as a function of the non-dimensional piston position. The absolute flow angle at turbine's inlet is assumed normal to the tangential direction, i.e. $\alpha_1 = 90°$, and it has been not calculated.

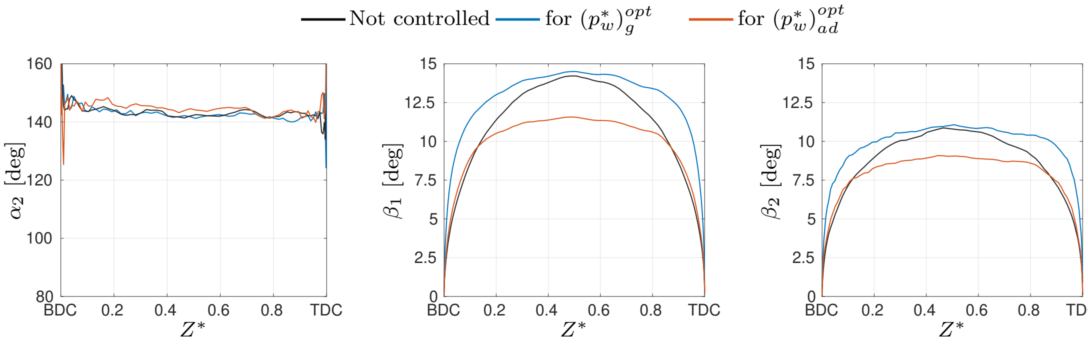

(a) Absolute outlet flow angle. (b) Relative inlet flow angle. (c) Relative outlet flow angle.

Figure 6.5: Comparison of the flow angles for controlled and uncontrolled turbine.

The relative flow angle at the inlet of the turbine, Fig. 6.5 (b), can be read as the effective control law applied to the turbine, which takes into account the dynamic effects of the control system. It has been compared between the different control strategies, making evident that the value of β_1 for the best aerodynamic efficiency is considerably lower than the corresponding value for the best global efficiency. The deviation angle β_2, Fig. 6.5 (b), depends on the incidence angle β_1, as follows from the potential flow analysis with blades of negligible thickness [30]. The same theoretic calculations explain the trends of the absolute flow angle at turbine's outlet, Fig. 6.5 (a), which appears almost unchanged among the different control strategies. In fact, from the potential flow analysis [30], follows that α_2 depends only on the rotor solidity (and not on the blade velocity or the inlet flow velocity).

In order to evaluate the effectiveness of the applied control laws on turbine efficiency, one may considered its value averaged on a cycle. Equations 6.3 are used for the calculations of the energy generated by the aerodynamic forces, E_{ad}, the output energy E_g, i.e. measured at turbine's shaft, and the available energy E_d, averaged on a cycle.

$$\begin{cases} E_{ad} &= \displaystyle\int_{T_w} (T_{ad}\,\Omega)\,\mathrm{d}t \\ E_g &= \displaystyle\int_{T_w} (T_{meas}\,\Omega)\,\mathrm{d}t \\ E_d &= \displaystyle\int_{T_w} (\Delta p_w\,Q)\,\mathrm{d}t \end{cases} \tag{6.3}$$

Following this definitions, the averaged values of turbine's efficiencies are calculated by dividing the useful energy by the available one:

$$\begin{cases} \overline{\eta_{ad}} = \dfrac{E_{ad}}{E_d} \\ \overline{\eta_g} = \dfrac{E_g}{E_d} \end{cases} \tag{6.4}$$

Bars in Fig. 6.6 compare the averaged value of the aerodynamic efficiency and the global efficiency, among the controlled and uncontrolled Wells turbine.

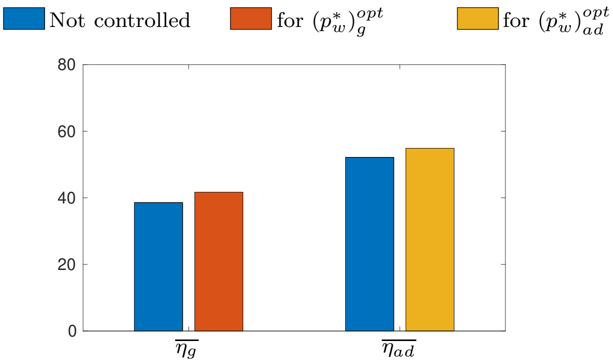

Figure 6.6: Rotor efficiencies averaged on a cycle for the turbine with and without control.

Efficiency comparisons in Fig. 6.6 show small improvements, in the order of $2 \div 4\%$, from the application of a rotational speed based control strategy, whatever the variable selected, thus confirming what expected from Fig. 6.3. However, the purpose of the present work is to demonstrate that, for a specified variable, the control strategy is capable to realize the expected result, although limited in value. Figure 6.6 shows that the two control laws effectively contribute to increase the averaged values of the aerodynamic and global efficiency.

The reported analysis, concerning the control of the rotational speed of the Wells turbine, was aimed to experimentally demonstrate the effectiveness and applicability of the control strategy as never done before in a OWC simulator rig. Although the improvements appear to be small, the authors do not exclude that more calibrated control strategies designed ad-hoc can increase the benefits. This control mode can be much more effective especially adapting the rotational speed of the turbine to the changing conditions of the sea state that occur during the operations of OWC devices with Wells turbines. Moreover and interesting, future experimental investigations could be performed to evaluate the effectiveness of this control strategy in reducing the noise emissions of the Wells turbine, which are of importance for full-scale installations. Starzmann et al. [53] show, with a numerical approach, the potential of a variable speed control in reducing the equivalent sound power level of a Wells turbine.

6.2 The variable pitch rotor blades

In order to control the incidence angle on the blades, a well known solution is to rotate the blade, of an angle γ, around a pivot, as schematized in Fig. 6.7.

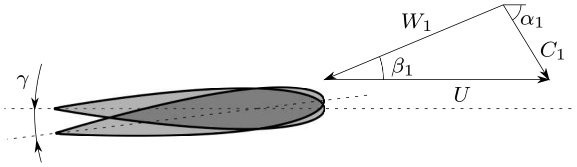

Figure 6.7: Velocity triangles at inlet of the turbine with variable pitch blades.

This solution, which is adopted in compressors, wind turbines, propellers, hydro turbines and so on, has been extensively studied also for the case of the Wells turbine [49,52,154,178,179]. Most of the works have been conducted with numerical approaches, while experimental studies have been carried out mainly to characterized turbine performance at different values of the stagger angle [52,154]. A Wells turbine with variable-pitch rotor blades was also designed to the Pico Power Plant [180], although it has never been tested at full-scale.

Although the pitch modification is generally thought as an active control, i.e. a external force acts on a kinematic that controls blade positioning around its pivot, it is possible to perform this control action also passively, i.e. by using the aerodynamic forces that act on the blade to realize the rotation. This has been studied in different works [154], and compared to the active control. For this purpose, bi-dimensional numerical investigations have been conducted on a Wells turbine with variable pitch [78], with the aim of extending the operating range of the turbine without stall occurrence.

The reference geometry chosen for these analyses was the high solidity Wells turbine housed at DIMCM laboratory, i.e. the existing facility described in Sec. 4.1. In Tab. 4.1 are summarized the main characteristics of the turbine. Numerical simulations were carried out on a multi-block structured grid, Fig. 6.8, composed of a central C-grid used for the discretization of the blade profile, surrounded by an unstructured triangular grid that allows mesh deformation and re-meshing when the blade is rotated. Inlet and outlet regions are fixed and build as structured grids. After a refinement study conducted to ensure grid independent results, a mesh with about 9×10^4 cells was selected, with a non-dimensional wall distance y^+ in the order of 1. The commercial CFD software Ansys Fluent® was used for simulations, by selecting the $k - \omega$ SST model for the turbulence closure and the SIMPLEC algorithm for the pressure-velocity coupling. A second-order upwind scheme was selected for discretizing convective terms and a second-order centered scheme for pressure and viscous terms. A User Defined Function (UDF) has been written to set the inlet absolute velocity as sinusoidal.

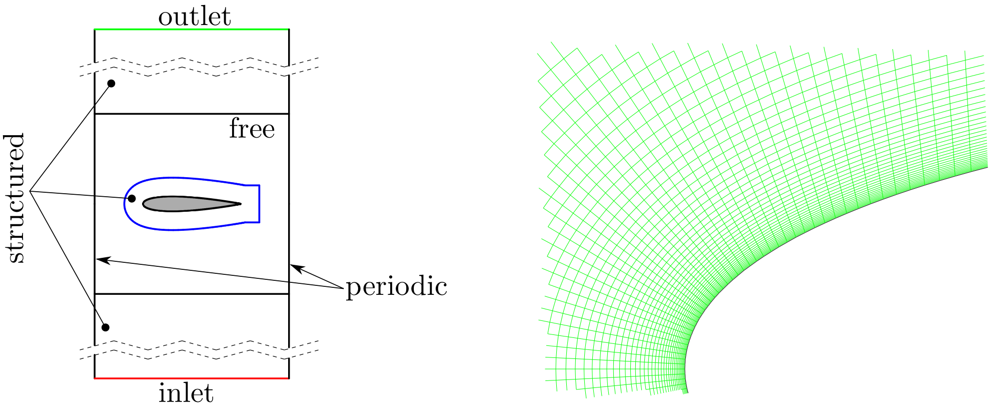

(a) Blocking scheme (b) Close-up view of the mesh

Figure 6.8: Blocking scheme and detailed view of the mesh around the blade.

Investigations have been divided into two main parts:

1. the stall limit of the rotor has been investigated for several stagger angles of the blade row, in order to determine a control law of pitch variation that extends the operating range while optimizing the energy production;

2. active and passive pitch controllers have been tested under dynamic simulations representative of the unsteady conditions inside a OWC.

Control actions were applied with two additional UDFs: the active pitch control was obtained by setting a variation of the pitch angle based on the stall limit constraint, while the passive control was performed by solving the differential equation that balances the forces acting on the blades, as expressed in Eqn. (6.5).

$$I_p\ddot{\gamma} + \zeta_m\dot{\gamma} + k_m\gamma = M \tag{6.5}$$

where I_p is the polar moment of inertia of the blade section, ζ_m is the damping coefficient and k_m is the elastic spring constant and M is the pitching moment acting on the section of the profile. The values of constant parameters in Eqn. (6.5) have been evaluated in order to extend the operating range of the turbine to $\phi = 0.5$, by considering the turbine made of aluminum and by modulating the system response to avoid oscillations. Thus, their values are listed in Tab. 6.1.

Table 6.1: Constant values used for passive control.

Aluminum density	2700 kg/m^3
Polar moment of inertia, I_p	2.93×10^{-5} kg/m^2/m
Damping coefficient, β_m	0.05 Nms/m
Elastic spring constant, k_m	3.16 Nm/m
Pivot position (percentage of the chord length)	12.5%

A semi-implicit time marching scheme has been used to solve Eqn. (6.5) in dynamic simulations.

The pivot position, around which the blade rotates, has been selected following the evaluation of the pressure center position for a NACA0015 profile staggered at different angles. It results, for stagger angles of $-5 \div 15°$, that the position of the pressure center is located around $25 \div 30\%$ of the blade chord. The pivot position at 12.5% of the blade chord has therefore been chosen.

A period of 9 s was selected for the sinusoidal velocity applied at the inlet boundary during dynamic simulations. The maximum value of the inlet velocity was selected depending on the required flow coefficient, for a fixed rotational speed of the rotor of 3000 rpm. Dynamic simulations were run for 3 working periods to ensure their repeatability without differences with respect to the previous period. Time-step size has been fixed to 5×10^{-5} s, in order to avoid any phase error on results.

The performance parameters, used to characterize and compare the different control solutions, are the torque coefficient $\mathcal{T}^*$, the static pressure drop coefficient p^*, the flow coefficient ϕ and the aerodynamic efficiency η_{ad}, as presented in Eqn. (2.1). Bi-dimensional simulations were carried out at turbine's mean radius, thus performance parameters were non-dimensionalized with respect to r_m.

6.2.1 Stall limit and pitch-control law

Different periods of the piston motion have been considered to realize different flow velocity at the inlet of a 2-dimensional bladed row oriented at several pitch angles, from 0 to 10 degrees. Results are reported in Fig. 6.9 (a), in terms of $\mathcal{T}^*$ versus ϕ, where black circles highlight the stall limit that are used to calculate the active pitch law shown in Fig. 6.9 (b).

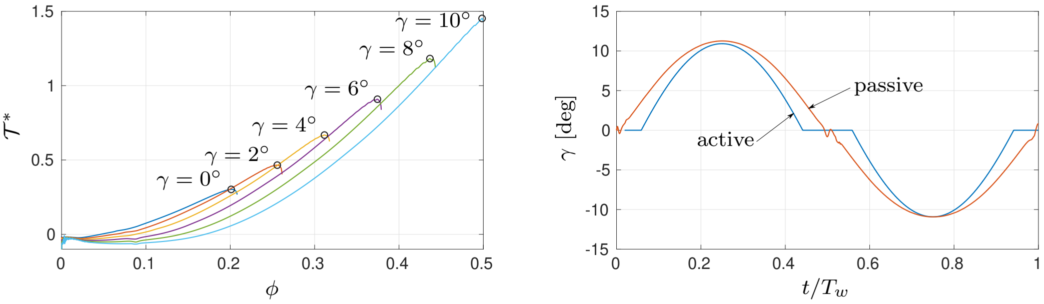

(a) Stall limit with different pitch angles.

(b) Pitch control laws.

Figure 6.9: Control laws for the pitch angle based on maximum output torque condition and self-actuated law.

After identifying the stall limit for the different pitch angles of the blade row, the control law has been calculated for the maximum output torque as shown in Fig. 6.9 (b). The same representation reports also the variation of the pitch angle when the passive control is simulated. By comparing active and passive control laws, it is reasonable to expect less output torque when the passive control is performed, for the same blade pitch angle.

6.2.2 Performance comparisons

Performance parameters are now compared between active controlled and self-pitch (passive) controlled rotor blades and the uncontrolled ones. Figure 6.10 shows the calculated non-dimensional aerodynamic torque, $\mathcal{T}^*$, the static pressure drop coefficient, p^*, and the aerodynamic efficiency η_{ad}.

Performance comparisons clearly show the effectiveness of the active pitch control in extending the operating range of the rotor, while incidence angle is kept to its maximum value, i.e. at the stall limit. Performance parameters of the active control are perfectly overlapped to their values when the blades are not controlled, in the limited operating range of the latest. More interesting is to compare performance between active controlled and self-controlled blades. Firstly, the torque coefficient for the active controlled solution is always higher than the self-controlled one, as required when the pitch law was established. Only for the maximum value of the flow coefficient, both the two control solutions allow to obtain the same output

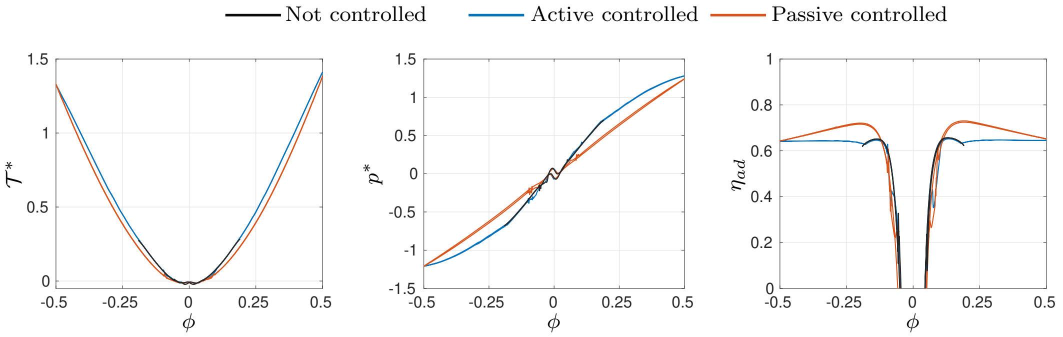

(a) Aerodynamic torque coefficient (b) Static pressure drop coefficient (c) Aerodynamic efficiency

Figure 6.10: Non-dimensional performance compared between controlled and not-controlled solutions.

torque. Similarly, the values of the pressure coefficient, when the active control is established, are always the highest, due to the higher incidence angle experienced by the blades. The pressure drop coefficient also looses its typical linear trend with the flow coefficient, while this is preserved when the blades are self-controlled. Finally, rotor aerodynamic efficiency is significantly different for the two control solutions. The highest values are calculated for the self-controlled rotor, for a flow coefficient around 0.19, while the active rotor, controlled for the maximum output torque, presents an almost constant value of the aerodynamic efficiency in the entire operating region. This result highlights the possibility to define a control strategy to maximize the turbine efficiency, which has not been investigated with the present simulations, similarly to the approach followed to control the rotational speed of the rotor (see Sec. 6.1).

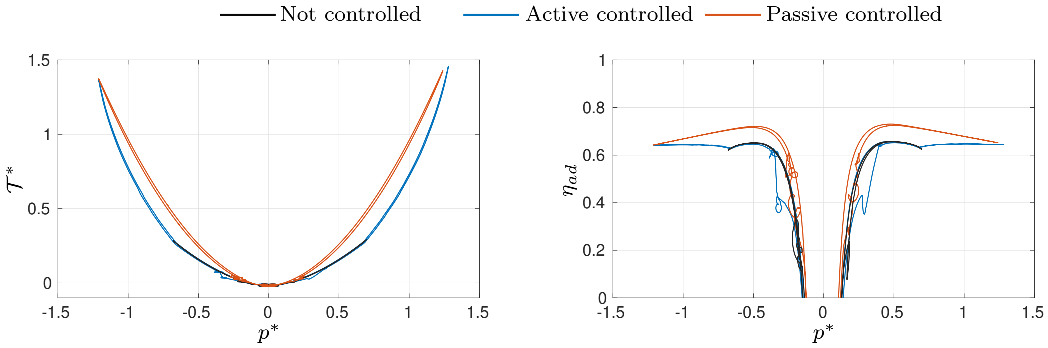

(a) Non-dimensional torque. (b) Aerodynamic efficiency.

Figure 6.11: Non-dimensional performance comparison, as a function of the pressure drop coefficient.

Performance parameters can be presented also as a function of the head coefficient of the rotor, i.e. the static pressure drop coefficient p^*, as shown in Fig.

6.11.

No substantial differences can be drawn from the representation of the aerodynamic efficiency with respect to p^*. On the other hand, the different behavior of the torque coefficient under the tested solutions is made more evident. For each value of the load on the blades, represented by p^*, active- and no-controlled rotors produce lower torque than the self-controlled rotor. This behavior is not surprising as the active control acts to always keep the aerodynamic load at its highest value, under different working conditions.

In conclusion, this preliminary 2-dimensional numerical investigation points out that an active control of the blade pitch angle allows to maximize different performance parameters, while a passive control is surely less expensive and complex than the former, achieving performance only marginally lower, but limiting flexibility in establishing the setpoint of the control strategy.

Chapter 7

Conclusions

This work presents an extensive analysis on the performance of the Wells turbine used to harvest wave energy, coupled with OWC devices. Theoretical rearrangements of well known relations used to characterize turbomachines performance have been proposed to define similar parameters that give a measure of the turbine performance, from different points of view. Aerodynamic losses and kinetic energy losses downstream the turbine have been quantified showing their relative weight on the overall efficiency with respect to the continuously varying operating conditions. The turbine efficiency has been also defined from the second-law point of view, i.e. by applying the exergy balance to the expansion process through the Wells turbine. Theoretical considerations have pointed out that no differences can be expected between first- and second-law efficiency, at least when the flow evolving inside the turbine can be assumed as incompressible.

The complexity of entropy estimation with experimental analyses has been overcome by simulating a number of rotor geometries, in order to verify the similarity between the first- and second-law efficiency. The way used to calculate intermediate quantities from the CFD simulations has been clarified before to present the results. The latter have shown the goodness of theoretical implications, at least for a low speed flow, thus confirming that first- and second-law approaches lead to very close results in estimating the turbine efficiency. The turbulence closure model used for simulations has been selected after a comparison of several largely used models, in order to understand which one better estimates the entropy production in the domain. As a result, the $k-\omega$ SST model has been selected, also for its capability to well predict the stall point of the turbine. Furthermore, numerical analyses have demonstrate that the difference between the net exergy flux and the entropy generation rate inside the domain, perhaps unsurprisingly as the entropy equation is not solved by the models, is significantly lower when the $k-\omega$ SST turbulence closure model is used. Finally, the entropy analyses can be still considered as a useful tool to locate source of losses in the flow field inside the Wells turbine, while no significant differences would be expected in efficiency calculation, with respect to the classical approach. On the other hand, this kind of analysis requires to pay great attention in selecting the turbulence closure model and simulation parameters in general, such as temporal and spatial discretization, since no equations for entropy conservation are solved in commercial CFD software.

Experimental investigations have been conducted to evaluate the performance parameters of the turbine, following the theoretical definitions. Measures of the global quantities were used to calculate the efficiency of the turbine and the losses contributions that affect its performance. Turbine aerodynamic performance is only slightly dependent on flow conditions, over a wide range of operating conditions that have been simulated in the laboratory. It has been also clarified that only a small part of the overall losses are due to the exhaust kinetic energy at the turbine exit, thus giving another important information on the actions that could be taken to improve turbine performance. A deep investigation on the local flow behavior near the Wells rotor, both at its inlet and outlet, under unsteady flow, has been conducted to locally estimate the turbine performance. This was very useful to locate the main source of losses, i.e. the hub region, due to the high proximity of the blades, and the tip region due to the leakage flow. The results of these experimental investigations could suggest modifications to the turbine's geometry. For example, it is possible to modify the tip gap and the *hub-to-tip* ratio to reduce the effects related to the leakage flow, or to act on the rotor solidity to increase the distance between the blades at the root. Finally, closer measurements to the rotor were carried out by means of a hot-wire-anemometer probe, in order to reconstruct the flow field along a blade pitch. HWA measurements have been used to characterize the turbulence intensity of the inlet flow and to reconstruct the flow field downstream the rotor. The last analysis proved useful to better understand the flow behavior downstream of the rotor, allowing to identify the position, extent and intensity of the loss concentration regions. Furthermore, the particular configuration of the rotor cascade of the Wells turbine determines a strong mutual interaction between the leading edge and the trailing edge of adjacent profiles, thus making the analysis and the interpretation of the measurements much more complicated, since the downstream flow mainly comes from the suction side of the profile.

Moreover, the experimental measurements have shown how the rotor performance depends on the operating conditions, as a confirmation of what expected from theoretical analyses. The two most investigated control strategies have been studied in the present work: the rotational speed control and the variable-pitch rotor blades.

The former has been experimentally analyzed from a turbomachinery point of view: the experiments were carried out to demonstrates the effectiveness of different control strategies, both applied under a periodic simulated wave motion. Although the efficiency improvements were relatively low, around $2 \div 4\%$ for both the two selected strategies, the experiments have pointed out that turbine performance can be improved modifying the operating conditions by controlling the rotational speed. The experimental results carried out in the present work can be extended at different flow conditions, for example considering operation at the stall limit in a wave period; under these extreme conditions, the gain of efficiency with the control of the rotational speed will be significantly higher.

The control solution based on the variable-pitch rotor blades has been numerically simulated by means of CFD. The case study, simplified as 2-dimensional, has been based on the geometry of the high solidity Wells turbine at DIMCM. An active control, carried out to extend the operating range of the turbine while maximizing the output torque, has been compared to a passive control, capable to extend the operating range to the same value of the active control. The passive controlled rotor blades has shown higher values of the aerodynamic efficiency and lower output torque, although the efficiency is not constant in the operating range. On the contrary, the active controlled rotor effectively produces higher output torque for each flow condition, but with a lower efficiency that is almost constant to its value at the stall limit, for each pitch angle. Although a passive controller can not achieves the higher performance, in terms of produced power, that can be obtained with an active controller designed to obtain the same operating range, the former is less expensive and simpler to design and it may represents an ideal choice to increase the turbine' s operating range.

7.1 Future investigations

The experimental and numerical activities carried out during the development of this thesis, can be further extended with a number of possible investigations listed below:

- Numerical simulations of the experimentally tested Wells turbine may be of interest in order to help in the investigation of local flow structures, partly too small and partly too complex to be investigated with probes, and to lead the design of experiments that could clarified the behavior of the flow field inside the Wells turbine.
- Experimental investigations with HWA, at different axial stations downstream the rotor, can be planned to reconstruct the vortex structures in the axial direction and to describe how they evolves and interacts during the mixing process at turbine exit.
- The comparison of different rotor geometries, made easier with the new designed "modular" Wells turbine. Local and global analyses, can be used in designing turbine configurations for real applications, and also to find more performing rotor geometries. These information can be also used to perform an optimization process of the turbine, with respect to the operating range of interest, also helped with a CFD approach.
- The possibility to reproduce non-regular wave periods with the OWC simulator housed at DIMCM, will allow to test the control of the rotational speed, as

implemented with the initial observation period, under flow conditions much more close to the real sea states.

- Experimental tests of a variable-pitch control system, both with the active and the passive solution.

Authored Conference and Journal Publications

[1] F. Licheri, F. Cambuli, P. Puddu and T. Ghisu. **A comparison of different approaches to estimate the efficiency of Wells turbines.** *Journal of Fluids Engineering*, 143(5), 02 2021, 10.1115/1.4049686

[2] T. Ghisu, F. Cambuli, P. Puddu, I. Virdis, M. Carta, and F. Licheri. **A critical examination of the hysteresis in Wells turbines using computational fluid dynamics and lumped parameter models.** *Journal of Offshore Mechanics and Arctic Engineering*, 142(2), 02 2020, 10.1115/1.4046379

[3] T. Ghisu, F. Cambuli, P. Puddu, I. Virdis, M. Carta, and F. Licheri. **A lumped parameter model to explain the cause of the hysteresis in OWC-Wells turbine systems for wave energy conversion.** *Applied Ocean Research*, 142(2), 94, 2020, 10.1016/j.apor.2019.101994

[4] F. Licheri, P. Puddu, T. Ghisu, and F. Cambuli. **Analisi numerico-sperimentale del flusso in turbina Wells.** *La Termotecnica*, Anno LXXII(10), 12, 2018

[5] F. Licheri, P. Puddu, T. Ghisu, and F. Cambuli. **Experimental analysis of the unsteady flow inside a Wells turbine.** *Proceedings of the 76 th Italian National Congress ATI*, 2021, 10.1051/e3sconf/202131211009

[6] F. Licheri, T. Ghisu, I. Virdis, P. Puddu and F. Cambuli. **Evaluation of entropy generation methods in Wells turbines.** *Proceedings of the 39 th International Conference on Offshore Mechanics and Arctic Engineering - OMAE*, 2019, 10.1115/omae2019-96513

[7] T. Ghisu, F. Cambuli, P. Puddu, I. Virdis, M. Carta, and F. Licheri. **A critical examination of the hysteresis in Wells turbines using computational fluid dynamics and lumped parameter models.** *Proceedings of the 39 th International Conference on Offshore Mechanics and Arctic Engineering - OMAE*, 2019, 10.1115/omae2019-96518

Appendix A

Comparison between fixed and rotating spinner

In order to evaluate the effects of a rotating spinner on turbine performance, numerical investigations, have been carried out on the existing facility described in Sec. 4.1.

The domain used for CFD simulations concerns the entire facility [130, 181], i.e. the chamber was included in the computational domain, and the piston motion was simulated by means of a moving wall. The domain and the computational mesh are shown in Figs. A.1 and A.2, respectively.

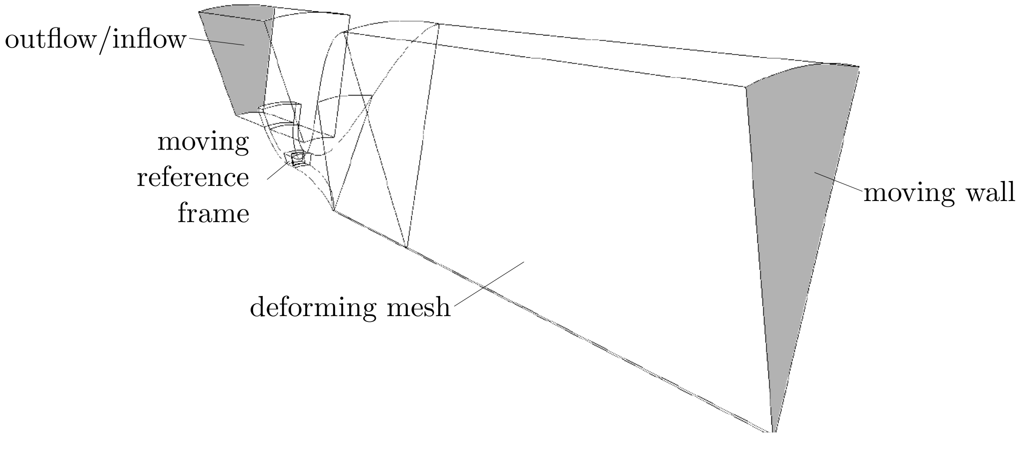

Figure A.1: Computational domain.

The data relating to the turbine were reported in Tab. 4.1, i.e. the high solidity Wells rotor with 14 blades were simulated. Unsteady operating conditions have been simulated by setting a piston stroke of 900 mm, the turbine rotational speed to 3600 rpm and a wave period of 9 s. The piston displacement was sinusoidal, similar to what reported in Fig. 5.5.

Simulations with rotating and fixed spinner were conducted by including or not

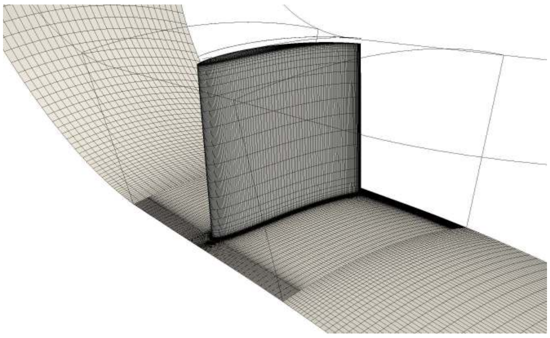

Figure A.2: Computational grid in the moving-reference-frame zone.

the spinner mesh in the rotating domain of the blade, while multiple-reference-frames simulate the interaction between stationary and rotating zones. More detailed information on the settings used for simulations can be found in [130, 181].

The first comparison between the two configurations, concerns the turbine global performance, as reported in Fig. A.3.

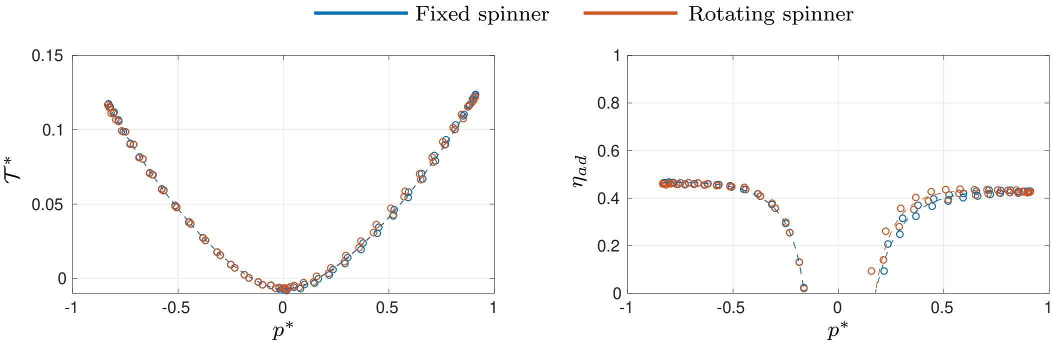

(a) Non-dimensional torque.

(b) Aerodynamic efficiency.

Figure A.3: Non-dimensional performance comparison, as a function of the static pressure drop coefficient.

No significant differences in performance can be observed between the two spinner's configurations, except for a slightly low value of the aerodynamic efficiency for the fixed spinner configuration, at low flow rates during the outflow phase. These very small differences present in the rotating spinner configuration can be attributed to some distortions induced to the inlet flow, if there's.

Velocities distributions along the blade height can give more information about the flow behavior near the turbine for the two configurations. Velocity components distributions, in the absolute frame, at turbine's inlet and outlet, are reported in Figs. A.4 (a) and (b), respectively, for the outflow phase.

Small, but significant, differences between the two configurations can be appreciated in the upstream flow in the hub region. The main differences can be observed in the distribution of the tangential component of the absolute velocity, C_θ, that shows

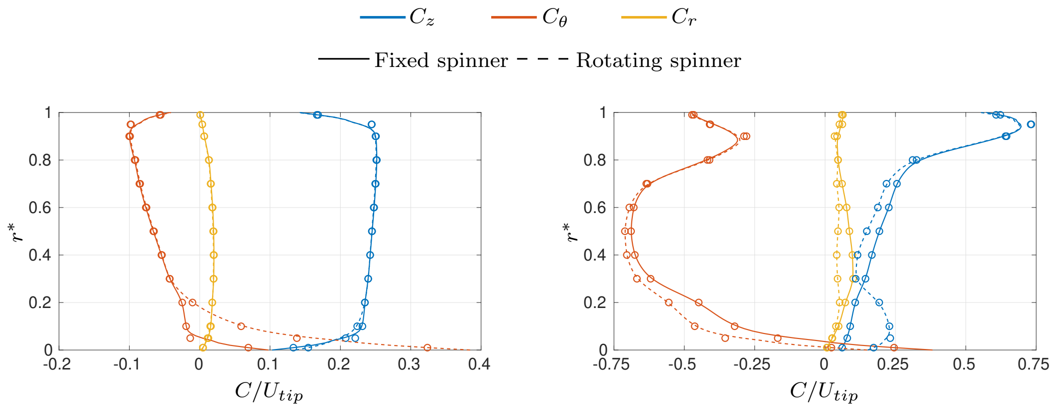

(a) Upstream velocity components.

(b) Downstream velocity components.

Figure A.4: Velocity components at turbine's inlet and outlet during the outflow phase, as a function of the non-dimensional radius.

higher and positive values when the spinner rotates, thus inducing an entrainment flow at low radii. Axial and radial components at turbine's inlet are not influenced by the spinner. On the contrary, the presence of a rotating spinner affects all the velocity components at turbine's outlet. These variations can be negligible for radial and tangential components, while they are more significant for the axial velocity component. In the hub region, higher values of the axial velocity component are observed when the spinner rotates, as the effect of the entrainment flow reduces the blockage near the blades root.

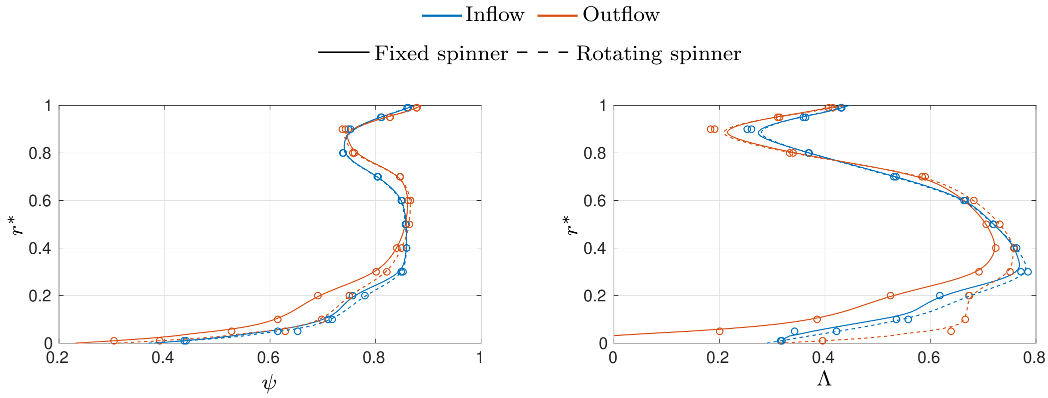

(a) Reduction coefficient of the relative velocity.

(b) Work coefficient.

Figure A.5: Comparison of local performance parameters during both the two phases.

Starting from the complete knowledge of the flow field near the turbine, the local performance parameter can be used to compare the two configurations. The work coefficient Λ and the reduction coefficient of the relative velocity ψ are represented in Fig. A.5, based on their definitions reported in Sec. 2.3.

Local performance along the blade span confirms, in a concise manner, that no differences can be observed between the two spinner configurations during the inflow phase. On the other hand, modifications in performance can be observed during the outflow phase, during which the turbine with a rotating spinner experiments slightly higher aerodynamic performance in the hub region, see Fig. A.5 (a), while producing a higher output work in the same blade region, see Fig. A.5 (b). These results justify the higher performance of the Wells rotor with a rotating spinner observed in Fig. A.3, although improvements at low radii, also relevant, do not determine proportional improvements of the global performance.

The analyses proposed in this section have been used to select which turbine configurations was preferable in designing the new rig (Sec. 4.2). The fixed spinner configuration, although slightly less performing, has been preferred due to the lower gradients that the velocity components experiment at blades' root, at the chamber side of the rotor. Thus, more similarity between the two feeding channels, i.e. during the inflow and the outflow phase, is expected.

Appendix B

Wall-proximity effects on "wedge" measurements

The "wedge" probe used for the investigation of the local flow field in the Wells turbine, see Sec. 5.3.2, has been characterized also for its wall-proximity effects. This analysis, often neglected when similar probes are used in large machines, becomes very important for the present case study, due to the reduced blade height.

Wall proximity effects of the "wedge" probe have been quantified by performing traversing measurements inside the low-speed wind tunnel shown in Fig. B.1.

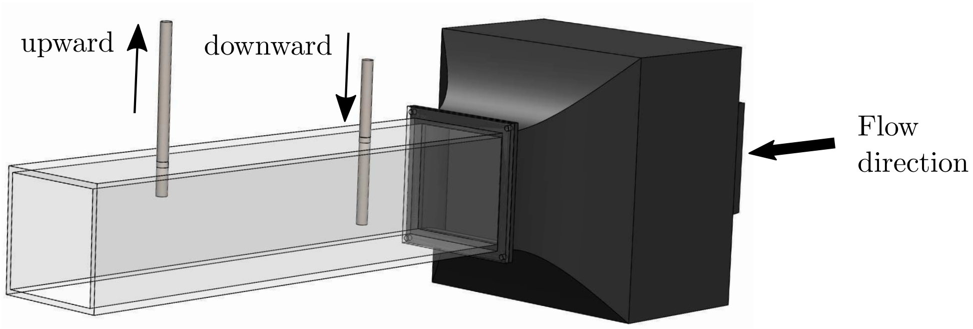

Figure B.1: Low-speed wind tunnel.

The calibration tunnel is configured as a blow-down wind-tunnel, and the flow is generated by an axial fan placed upstream the measurement section. The measurement section, made of transparent PMMA, is squared with a side of 200 mm. In Fig. B.1 are reported the directions along which the probe, schematized as a cylinder, is moved with respect to the walls. Wall-proximity effects are generally not equals with respect these two directions [182], and differences are expected in particular for the "wedge" probe, due its non symmetric taps configuration. Although this consideration, a preliminary test conducted for the "wedge" probe has shown that measures are relatively less affected by wall-proximity when the probe is moved upward. For this reason, proximity effects have been quantified, and correction factors have been based on measurements conducted, only when the probe is moved downward, inside the test section.

Two additional probes have been used to detect static and total pressures inside the tunnel, from the bottom wall to the midspan region. A pitot tube has employed for the static pressure traversing while a “Kiel” probe has been adopted to detect the total pressure. Tests have been conducted at different velocities of the main flow, between 10 ÷ 20 m/s, obtained by varying the fan rotational speed.

Correction factors have been established for the static and total pressure, and expressed as follows:

$$k_S = \frac{p - p_{wedge}}{p_t - p_s} \qquad\qquad k_T = \frac{p_t - p_{t,wedge}}{p_t - p_s} \tag{B.1}$$

where k_S and k_T are the correction factors referred to the static and total pressure, respectively, p and p_t are the static and total reference pressures.

Figure B.2 reports the correction factors k_S and k_T as a function of the non-dimensional distance from the wall d/H, i.e. the ratio between the distance of the measurement taps from the wall and the maximum head size of the wedge probe (equal to 2.5 mm).

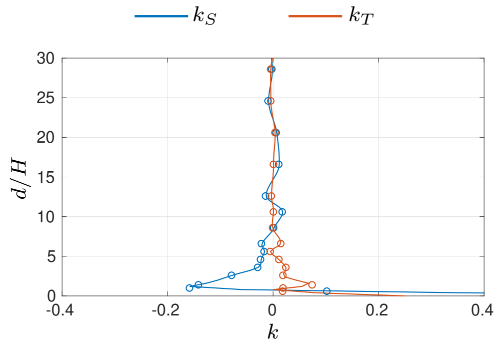

Figure B.2: Correction factors for wall-proximity effects of the “wedge” probe.

The distributions in Fig. B.2 clearly highlight a region near the wall in which the “wedge” measured pressures are distorted from the reference values. This zone is sensibly larger for the static pressure measurement, for which all the directional pressure taps are involved (see Sec. 5.3.2), while it is very small for the total pressure. Due to the large extension of wall effects with respect to the Wells annular channel height (about 12 times the maximum head size of the wedge probe), the correction factors have been averaged and assumed constant for each distance from the wall:

$$k_S = -0.115 \qquad\qquad k_T = -0.008 \tag{B.2}$$

It could be observed that the correction factor for the total pressure k_T is sensibly small; neglecting this correction does not sensibly affect the results of flow reconstruction inside the Wells turbine rig.

No sensibly wall-proximity effects have been observed on the reconstruction of the yaw angle, while the pitch angle calculation is distorted only when the probe’s head is touching the wall. Thus, no further corrections have been applied to flow angles.

Appendix C

Instrumentation data

In the present table, the instrumentation used for experimental measurements is summarizes.

Function	**Model**	**Full-scale**	**Sensitivity**
Wall static pressure at ambient side	Sensor Technics BSDX0010D4D	±1 kPa	2 V/kPa
Wall static pressure at chamber side	Sensor Technics 50SP001D44D	±7 kPa	0.3 V/kPa
Wedge probe pressures (equal for each tap)	Sensor Technics BSDX0025D4D	±2.5 kPa	0.8 V/kPa
Torque sensor	Instrumentation Devices DRFL-I	±2 Nm	5 V/Nm
Linear Potentiometer	MAFtec srl DWT-010-10K-CN1	1.5 m	4.0 V/m
Traversing motor for radial positioning	RMS Technologies R208 Driver	-	0.00125 mm/step
Traversing motor for angular positioning	Oriental Motors DG60-ASAK	-	0.02 deg/step

Bibliography

[1] T. Setoguchi, M. Takao, and K. Kaneko. Hysteresis on Wells turbine characteristics in reciprocating flow. *International Journal of Rotating Machinery*, 4(1):17–24, 1998.

[2] R. Pelc and R.M. Fujita. Renewable energy from the ocean. *Marine Policy*, 26(6):471–479, 2002.

[3] A. H. Izadparast and J. M Niedzwecki. Estimating the potential of ocean wave power resources. *Ocean Engineering*, 38(1):177–185, 2011.

[4] K. Gunn and C. Stock-Williams. Quantifying the global wave power resource. *Renewable Energy*, 44:296–304, 2012.

[5] G. Mørk, S. Barstow, A. Kabuth, and M. T. Pontes. Assessing the global wave energy potential. *Proceedings of the 29th International Conference on Ocean, Offshore and Arctic Engineering: Volume 3*, pages 447–454, 06 2010.

[6] J. Portilla, J. Sosa, and L. Cavaleri. Wave energy resources: Wave climate and exploitation. *Renewable Energy*, 57:594–605, 2013.

[7] G. Iglesias, M. López, R. Carballo, A. Castro, J.A. Fraguela, and P. Frigaard. Wave energy potential in Galicia (NW Spain). *Renewable Energy*, 34(11):2323–2333, 2009.

[8] P. Lenee-Bluhm, R. Paasch, and H.T. Özkan Haller. Characterizing the wave energy resource of the US Pacific Northwest. *Renewable Energy*, 36(8):2106–2119, 2011.

[9] D. Mollison and M.T. Pontes. Assessing the Portuguese wave-power resource. *Energy*, 17(3):255–268, 1992.

[10] G. Kim, W.M. Jeong, K.S. Lee, K. Jun, and M.E. Lee. Offshore and nearshore wave energy assessment around the Korean Peninsula. *Energy*, 36(3):1460–1469, 2011.

[11] S. Jin and D. Greaves. Wave energy in the UK: Status review and future perspectives. *Renewable and Sustainable Energy Reviews*, 143, 2021.

[12] S.P. Neill, A. Vögler, A.J. Goward-Brown, S. Baston, M.J. Lewis, P.A. Gillibrand, S. Waldman, and D.K. Woolf. The wave and tidal resource of Scotland. *Renewable Energy*, 114:3–17, 2017.

[13] A. Clément, P. McCullen, A. F. O. Falcão, A. Fiorentino, F. Gardner, K. Hammarlund, G. Lemonis, T. Lewis, K. Nielsen, S. Petroncini, M. T. Pontes, P. Schild, B.-O. Sjöström, H. C. Sørensen, and T. Thorpe. Wave energy in Europe: Current status and perspectives. *Renewable and Sustainable Energy Reviews*, 6(5):405–431, 2002.

[14] D. Vicinanza, P. Contestabile, and V. Ferrante. Wave energy potential in the north-west of Sardinia (Italy). *Renewable Energy*, 50:506–521, 2013.

[15] G. Besio, L. Mentaschi, and A. Mazzino. Wave energy resource assessment in the Mediterranean Sea on the basis of a 35-year hindcast. *Energy*, 94:50–63, 2016.

[16] D. Vicinanza, L. Cappietti, V. Ferrante, and P. Contestabile. Estimation of the wave energy in the Italian offshore. *Journal of Coastal Research*, pages 613–617, 2011.

[17] L. Liberti, A. Carillo, and G. Sannino. Wave energy resource assessment in the Mediterranean, the Italian perspective. *Renewable Energy*, 50:938–949, 2013.

[18] F. Karathanasi, T. Soukissian, and D. Sifnioti. Offshore wave potential of the Mediterranean sea. *Renewable Energy and Power Quality Journal*, 1(13):461–465, 2015.

[19] C.L. Re, G. Manno, G. Ciraolo, and G. Besio. Wave energy assessment around the Aegadian Islands (Sicily). *Energies*, 12(3), 2019.

[20] V. Vannucchi and L. Cappietti. Wave energy assessment and performance estimation of state of the artwave energy converters in italian hotspots. *Sustainability (Switzerland)*, 8(12), 2016.

[21] T. Aderinto and H. Li. Ocean wave energy converters: Status and challenges. *Energies*, 11(5), 2018.

[22] T. V. Heath. A review of oscillating water column. *Philosophical Transactions of the Royal Society A: Mathematical, Physical and Engineering Sciences*, 370(1959):235–245, 2012.

[23] J. Falnes. A review of wave-energy extraction. *Marine Structures*, 20(4):185–201, 2007.

[24] T. Aderinto and H. Li. Review on power performance and efficiency of wave energy converters. *Energies*, 12(22), 2019.

[25] A. F. O. Falcão and J. C. C. Henriques. Oscillating-Water-Column wave energy converters and air turbines: A review. *Renewable Energy*, 85:1391–1424, 2016.

[26] A. Garcia-Teruel and D. I. M. Forehand. A review of geometry optimisation of wave energy converters. *Renewable and Sustainable Energy Reviews*, 139:110593, 2021.

[27] B. Drew, A. R. Plummer, and M. N. Sahinkaya. A review of wave energy converter technology. *Proceedings of the Institution of Mechanical Engineers, Part A: Journal of Power and Energy*, 223(8):887–902, 2009.

[28] A. F. O. Falcão. Wave energy utilization: A review of the technologies. *Renewable and Sustainable Energy Reviews*, 14(3):899–918, 2010.

[29] N. Delmonte, D. Barater, F. Giuliani, P. Cova, and G. Buticchi. Oscillating water column power conversion: A technology review. *Proceedings of the IEEE Energy Conversion Congress and Exposition, ECCE 2014*, pages 1852–1859, 2014.

[30] A. F. O. Falcão and L. M. C. Gato. *Air turbines*, volume 8. 2012.

[31] M. Takao and T. Setoguchi. Air turbines for wave energy conversion. *International Journal of Rotating Machinery*, 2012, 2012.

[32] Y. Masuda. An experience of wave power generator through tests and improvement. *In: Evans D.V., de Falcão A. F. O. (eds) Hydrodynamics of Ocean Wave-Energy Utilization. International Union of Theoretical and Applied Mechanics.*, 1986.

[33] Zhen Liu, Ying Cui, Chuanli Xu, Lixin Sun, Ming Li, and Jiyuan Jin. Experimental and numerical studies on an OWC axial-flow impulse turbine in reciprocating air flows. *Renewable and Sustainable Energy Reviews*, 113:109272, 2019.

[34] T. Setoguchi, S. Santhakumar, H. Maeda, M. Takao, and K. Kaneko. A review of impulse turbines for wave energy conversion. *Renewable Energy*, 23(2):261–292, 2001.

[35] A. A. D. Carrelhas, L. M. C. Gato, J. C. C. Henriques, A. F. O. Falcão, and J. Varandas. Test results of a 30 kW self-rectifying biradial air turbine-generator prototype. *Renewable and Sustainable Energy Reviews*, 109:187–198, 2019.

[36] A. A. D. Carrelhas, L. M. C. Gato, J. C. C. Henriques, and A. F. O. Falcão. Experimental study of a self-rectifying biradial air turbine with fixed guide-vanes arranged into two concentric annular rows. *Energy*, 198:117211, 2020.

[37] L. M. C. Gato, A. R. Maduro, A. A. D. Carrelhas, J. C. C. Henriques, and D. N. Ferreira. Performance improvement of the biradial self-rectifying impulse air-turbine for wave energy conversion by multi-row guide vanes: Design and experimental results. *Energy*, 216:119110, 2021.

[38] A. F. O. Falcão, J. C. C. Henriques, L. M. C. Gato, and R. P. F. Gomes. Air turbine choice and optimization for floating oscillating-water-column wave energy converter. *Ocean Engineering*, 75:148–156, 2014.

[39] M. García-Díaz, B. Pereiras, C. Miguel-González, L. Rodríguez, and J. Fernández-Oro. CFD analysis of the performance of a double decker turbine for wave energy conversion. *Energies*, 14(4), 2021.

[40] M. García-Díaz, B. Pereiras, C. Miguel-González, L. Rodríguez, and J. Fernández-Oro. Design of a new turbine for OWC wave energy converters: The DDT concept. *Renewable Energy*, 169:404–413, 2021.

[41] A. A. Wells. Fluid Driven Rotary Transducer - BR. Pat. 1595700, 1976.

[42] A.S. Shehata, Q. Xiao, K.M. Saqr, and D. Alexander. Wells turbine for wave energy conversion: a review. *International Journal of Energy Research*, 41(1):6–38, 2017.

[43] H. Osawa, Y. Washio, T. Ogata, Y. Tsuritani, and Y. Nagata. The offshore floating type wave power device “Mighty Whale” open sea tests performance of the prototype. *Proceedings of the International Ocean and Polar Engineering Conference*, All Days, 05 2002. ISOPE-I-02-090.

[44] António F.O. Falcão, António J.N.A. Sarmento, Luís M.C. Gato, and Ana Brito-Melo. The Pico OWC wave power plant: Its lifetime from conception to closure 1986–2018. *Applied Ocean Research*, 98:102104, 2020.

[45] C. Boake, T. Whittaker, M. Folley, and H. Ellen. Overview and initial operational experience of the LIMPET wave energy plant. *Proceedings of the International Offshore and Polar Engineering Conference*, 12, 01 2002.

[46] Yago Torre-Enciso, I. Ortubia, L.I. Aguileta, and J. Marqués. Mutriku wave power plant: From the thinking out to the reality. *Proceedings of the 8th European Wave and Tidal Energy Conference*, pages 319–329, 01 2009.

[47] S. Raghunathan. The Wells air turbine for wave energy conversion. *Progress in Aerospace Sciences*, 31(4):335–386, 1995.

[48] L. M. C. Gato and A. F. O. Falcão. Aerodynamics of the Wells turbine. *International Journal of Mechanical Sciences*, 30(6):383 – 395, 1988.

[49] M. Inoue, K. Kaneko, T. Setoguchi, and H. Hamakawa. Air turbine with self-pitch controlled blades for wave power generator (estimation of performance by model testing). *JSME International Journal, Series B: Fluids and Thermal Engineering*, 32(1):19–24, 1989.

[50] R. Curran and L. M. C. Gato. The energy conversion performance of several types of Wells turbine designs. *Proceedings of the Institution of Mechanical Engineers, Part A: Journal of Power and Energy*, 211(2):133–145, 1997.

[51] M. Webster, L. M. C. Gato, and P. R. S. White. Variation of blade shape and its effect on the performance of the Wells turbine. *International Journal of Ambient Energy*, 19(3):149–156, 1998.

[52] L. M. C. Gato and M. Webster. An experimental investigation into the effect of rotor blade sweep on the performance of the variable-pitch Wells turbine.

Proceedings of the Institution of Mechanical Engineers, Part A: Journal of Power and Energy, 215(5):611–622, 2001.

[53] R. Starzmann, C. Moisel, T.H. Carolus, K. Tease, and R. Arlitt. Assessment method of sound radiated by cyclically operating Wells turbines. *International Journal of Marine Energy*, 2:12 – 27, 2013.

[54] J. S. Laves, L. M. C. Gato, A. F. O. Falcão, and J. C. C. Henriques. Experimental investigation on performance improvement by mid-plane guide-vanes in a biplane-rotor Wells turbine for wave energy conversion. *Renewable and Sustainable Energy Reviews*, 150:111497, 2021.

[55] S. Raghunathan and O. O. Ombaka. Effect of frequency of air flow on the performance of the Wells turbine. *International Journal of Heat and Fluid Flow*, 6(2):127–132, 1985.

[56] A. Thakker and R. Abdulhadi. The performance of Wells turbine under bi-directional airflow. *Renewable Energy*, 33(11):2467 – 2474, 2008.

[57] M. Paderi and P. Puddu. Experimental investigation in a Wells turbine under bi-directional flow. *Renewable Energy*, 57:570–576, 2013.

[58] P. Puddu, M. Paderi, and C. Manca. Aerodynamic characterization of a Wells turbine under bi-directional airflow. *Proceedings of the 68th Italian National Congress ATI*, 45:278–287, 2014.

[59] M. Torresi, M. Stefanizzi, F. Fornarelli, L. Gurnari, F. Filianoti, P. Giuseppe, and S. M. Camporeale. Performance characterization of a Wells turbine under unsteady flow conditions. *AIP Conference Proceedings*, 2191(1):020149, 2019.

[60] T. K. Das, K. Kumar, and A. Samad. Experimental analysis of a biplane Wells turbine under different load conditions. *Energy*, 206:118205, 2020.

[61] F. Licheri, P. Puddu, T. Ghisu, and F. Cambuli. Experimental analysis of the unsteady flow inside a Wells turbine. *Proceedings of the 76th Italian National Congress ATI*, 312:11009, 2021.

[62] S. M. Camporeale, M. Torresi, G. Pascazio, and B. Fortunato. A 3d unsteady analysis of a Wells turbine in a sea-wave energy conversion device. *Proceedings of the Turbo Expo 2003*, 6, Parts A and B:989–998, 06 2003.

[63] T. S. Dhanasekaran and M. Govardhan. Computational analysis of performance and flow investigation on Wells turbine for wave energy conversion. *Renewable Energy*, 30(14):2129–2147, 2005.

[64] M. Torresi, S.M. Camporeale, P.D. Strippoli, and G. Pascazio. Accurate numerical simulation of a high solidity Wells turbine. *Renewable Energy*, 33(4):735 – 747, 2008.

[65] M. Torresi, S.M. Camporeale, and G. Pascazio. Detailed CFD analysis of the steady flow in a Wells turbine under incipient and deep stall conditions.

Journal of Fluids Engineering, Transactions of the ASME, 131(7):0711031–07110317, 2009.

[66] K. Kincaid and D. W. MacPhee. Cfd analysis of stall in a Wells turbine. Volume 1: Fuels, Combustion, and Material Handling; Combustion Turbines Combined Cycles; Boilers and Heat Recovery Steam Generators; Virtual Plant and Cyber-Physical Systems; Plant Development and Construction; Renewable Energy Systems, 06 2018. V001T06A031.

[67] J. K. Watterson and S. Raghunathan. Computed effects of solidity on Wells turbine performance. *JSME International Journal, Series B: Fluids and Thermal Engineering*, 41(1 SUPPL. SI):177–183, 1998.

[68] C. Miguel González, G. Rodríguez Fuertes, M. García Díaz, B. Pereiras García, F. Castro, and J. M. Fernández Oro. Wells turbine with variable blade profile for wave energy conversion. *Proceedings of the International Conference on Offshore Mechanics and Arctic Engineering*, Volume 10: Ocean Renewable Energy, 06 2018.

[69] R. Starzmann, T. H. Carolus, K. Tease, and R. Arlitt. Effect of design parmeters on aero-acoustic and aerodynamic performance of Wells turbines. *Proceedings of the International Conference on Offshore Mechanics and Arctic Engineering*, Volume 5: Ocean Space Utilization; Ocean Renewable Energy:299–308, 06 2011.

[70] M. Takao, T. Setoguchi, S. Nagata, and K. Toyota. A study on the effects of blade profile and non-uniform tip clearance of the Wells turbine. *Proceedings of the International Conference on Offshore Mechanics and Arctic Engineering*, 6:625–632, 06 2008.

[71] P. Halder, S. H. Rhee, and A. Samad. Numerical optimization of wells turbine for wave energy extraction. *International Journal of Naval Architecture and Ocean Engineering*, 9(1):11 – 24, 2017.

[72] P. Halder, A. Samad, and D. Thévenin. Improved design of a Wells turbine for higher operating range. *Renewable Energy*, 106:122 – 134, 2017.

[73] T. Gratton, T. Ghisu, G. Parks, F. Cambuli, and P. Puddu. Optimization of blade profiles for the Wells turbine. *Ocean Engineering*, 169:202–214, 2018.

[74] T. K. Das and A. Samad. Influence of stall fences on the performance of Wells turbine. *Energy*, 194:116864, 2020.

[75] P. M. Kumar, P. Halder, and A. Samad. Performance analysis of Wells turbine with radiused blade tip. *Proceedings of the International Conference on Offshore Mechanics and Arctic Engineering*, Volume 10: Ocean Renewable Energy, 06 2018.

[76] P. M. Kumar and A. Samad. Introducing gurney flap to Wells turbine blade and performance analysis with openfoam. *Ocean Engineering*, 187:106212, 2019.

[77] A. J. N. A. Sarmento, L. M. C. Gato, and A. F. O. Falcão. Turbine-controlled wave energy absorption by oscillating water column devices. *Ocean Engineering*, 17(5):481–497, 1990.

[78] F. Licheri, A. Climan, P. Puddu, F. Cambuli, and T. Ghisu. Numerical study of a Wells turbine with variable pitch rotor blades. *Proceedings of the 73rd Italian National Congress ATI*, 148:511–518, 2018.

[79] M.H. Mohamed and S. Shaaban. Optimization of blade pitch angle of an axial turbine used for wave energy conversion. *Energy*, 56:229 – 239, 2013.

[80] K. C. Kincaid and D. W. MacPhee. Numerical fluid–structure interaction analysis of a Wells turbine with flexible blades. *Journal of Energy Resources Technology*, 142(8), 03 2020. 081305.

[81] V. Barnabei, A. Castorrini, A. Corsini, and F. Rispoli. Fsi analysis and simulation of flexible blades in a Wells turbine for wave energy conversion. *Proceedings of the 75th Italian National Congress ATI*, 197:11008, 01 2020.

[82] T. Ghisu, F. Cambuli, P. Puddu, N. Mandas, P. Seshadri, and G. T. Parks. Numerical evaluation of entropy generation in isolated airfoils and Wells turbines. *Meccanica*, 53(14):3437, November 2018.

[83] F. Licheri, F. Cambuli, P. Puddu, and T. Ghisu. A comparison of different approaches to estimate the efficiency of Wells turbines. *Journal of Fluids Engineering*, 143(5), 02 2021. 051205.

[84] A.S. Shehata, K.M. Saqr, Q. Xiao, M.F. Shehadeh, and A. Day. Performance analysis of Wells turbine blades using the entropy generation minimization method. *Renewable Energy*, 86:1123–1133, 2016.

[85] A.S. Shehata, Q. Xiao, M. El-Shaib, A. Sharara, and D. Alexander. Comparative analysis of different wave turbine designs based on conditions relevant to northern coast of egypt. *Energy*, 120:450–467, 2017.

[86] A.S. Shehata, Q. Xiao, M.M. Selim, A.H. Elbatran, and D. Alexander. Enhancement of performance of wave turbine during stall using passive flow control: First and second law analysis. *Renewable Energy*, 113:369–392, 2017.

[87] R. Soltanmohamadi and E. Lakzian. Improved design of Wells turbine for wave energy conversion using entropy generation. *Meccanica*, 51(8):1713–1722, 2016.

[88] M. Nazeryan and E. Lakzian. Detailed entropy generation analysis of a Wells turbine using the variation of the blade thickness. *Energy*, 143:385 – 405, 2018.

[89] S. Shaaban. Insight analysis of biplane Wells turbine performance. *Energy Conversion and Management*, 59:50 – 57, 2012.

[90] Q. Hu and Y. Li. Unsteady RANS Simulations of Wells Turbine Under Transient Flow Conditions. *Journal of Offshore Mechanics and Arctic Engineering*, 140(1), 09 2017. 011901.

[91] Y. Kinoue, T.H. Kim, T. Setoguchi, M. Mohammad, K. Kaneko, and M. Inoue. Hysteretic characteristics of monoplane and biplane Wells turbine for wave power conversion. *Energy Conversion and Management*, 45(9-10):1617–1629, 2004.

[92] T. Setoguchi, Y. Kinoue, T.H. Kim, K. Kaneko, and M. Inoue. Hysteretic characteristics of Wells turbine for wave power conversion. *Renewable Energy*, 28(13):2113–2127, 2003.

[93] T. Ghisu, P. Puddu, and F. Cambuli. Numerical analysis of a Wells turbine at different non-dimensional piston frequencies. *Journal of Thermal Science*, 24(6):535–543, 2015.

[94] F. Cambuli, T. Ghisu, I. Virdis, and P. Puddu. Dynamic interaction between owc system and Wells turbine: A comparison between cfd and lumped parameter model approaches. *Ocean Engineering*, 191:106459, 2019.

[95] I. Virdis, T. Ghisu, F. Cambuli, and P. Puddu. A lumped parameter model for the analysis of dynamic effects in Wells turbines. *Energy Procedia*, 148:503–510, 2018.

[96] A. Brito-Melo, L. M. C. Gato, and A. J. N. A. Sarmento. Analysis of Wells turbine design parameters by numerical simulation of the owc performance. *Ocean Engineering*, 29(12):1463–1477, 2002.

[97] M. Govardhan and T. S. Dhanasekaran. Effect of guide vanes on the performance of a self-rectifying air turbine with constant and variable chord rotors. *Renewable Energy*, 26(2):201–219, 2002.

[98] S. Raghunathan and W. C. Beattie. Aerodynamic performance of contra-rotating Wells turbine for wave energy conversion. *Proceedings of the Institution of Mechanical Engineers, Part A: Journal of Power and Energy*, 210(6):431–447, 1996.

[99] M. Folley, R. Curran, and T. Whittaker. Comparison of LIMPET contra-rotating Wells turbine with theoretical and model test predictions. *Ocean Engineering*, 33(8):1056 – 1069, 2006.

[100] T. K. Das and A. Samad. The effect of midplane guide vanes in a biplane Wells turbine. *Journal of Fluids Engineering*, 141(5), 11 2018.

[101] K. Kaneko, T. Setoguchi, H. Hamakawa, and M. Inoue. Biplane axial turbine for wave power generator. *International Journal of Offshore and Polar Engineering*, 1(2):122–128, 1991.

[102] L. M. C. Gato and R. Curran. Performance of the biplane Wells turbine. *Journal of Offshore Mechanics and Arctic Engineering*, 118(3):210–215, 08 1996.

[103] M.H. Mohamed, G. Janiga, E. Pap, and D. Thévenin. Multi-objective optimization of the airfoil shape of Wells turbine used for wave energy conversion. *Energy*, 36(1):438 – 446, 2011.

[104] S. Raghunathan and C. P. Tan. Effect of blade profile on the performance of the Wells self-rectifying air turbine. *International Journal of Heat and Fluid Flow*, 6(1):17–22, 1985.

[105] F. Licheri, T. Ghisu, I. Virdis, P. Puddu, and F. Cambuli. Evaluation of entropy generation methods in Wells turbines. *Proceedings of the International Conference on Offshore Mechanics and Arctic Engineering*, 10, 2019.

[106] S. Raghunathan, C. P. Tan, and O. O. Ombaka. Performance of the Wells self-rectifying air turbine. *Aeronautical Journal*, 89:369–379, December 1985.

[107] S. L. Dixon. *Fluid Mechanics and Thermodynamics of Turbomachinery.* Elsevier textbooks, [s.l.], 5. aufl. edition, 2005.

[108] S. Raghunathan, C. P. Tan, and N. A. J. Wells. Theory and performance of a Wells turbine. *J. ENERGY*, 6(2 , Mar.-Apr. 1982):156–160, 1982.

[109] M. Suzuki, C. Arakawa, and T. Tagori. Fundamental studies on Wells turbine for wave power generator (1st report, the effect of solidity, and self-starting). *Bulletin of JSME*, 27(231):1925–1931, 1984.

[110] L. M. C. Gato and A. F. de O. Falca˜o. On the theory of the Wells turbine. *Journal of Engineering for Gas Turbines and Power*, 106(3):628–633, 07 1984.

[111] A. Bejan. *Advanced Engineering Thermodynamics.* John Wiley & Sons, Inc., 2006.

[112] S. C. Gülen. *Heat and Mass Balance*, page 136–153. Cambridge University Press, 2019.

[113] J. H. Horlock. Losses and efficiencies in axial-flow turbines. *International Journal of Mechanical Sciences*, 2(1):48–75, 1960.

[114] J. H. Ferziger and M. Periˇc. *Computational methods for fluid dynamics.* Springer-Verlag, 2002.

[115] H.K. Versteeg and W. Malalasekera. *An Introduction to Computational Fluid Dynamics: The Finite Volume Method.* Pearson Education Limited, 2007.

[116] D. A. Anderson, J. C. Tannehill, and R. H. Pletcher. *Computational fluid mechanics and heat transfer.* Taylor & Francis Inc, 1984.

[117] H. Herwig and F. Kock. Direct and indirect methods of calculating entropy generation rates in turbulent convective heat transfer problems. *Heat and Mass Transfer*, 43(3):207–215, Jan 2007.

[118] J. Moore and J. G. Moore. Entropy production rates from viscous flow calculations: part i - a turbulent boundary layer flow. *American Society of Mechanical Engineers (Paper)*, (83-GT-70), 1983.

[119] C. L. Iandoli, E. Sciubba, and N. Zeoli. The computation of the entropy generation rate for turbomachinery design applications: some theoretical remarks and practical examples. *International Journal of Energy Technology and Policy*, 6(1):64–95, 2008.

[120] Y. Jin and H. Herwig. Turbulent flow in rough wall channels: Validation of rans models. *Computers & Fluids*, 122:34 – 46, 2015.

[121] Pietro Asinari, Matteo Fasano, and Eliodoro Chiavazzo. A kinetic perspective on k–ε turbulence model and corresponding entropy production. *Entropy*, 18(4), 2016.

[122] T.-H. Shih, W. W. Liou, A. Shabbir, Z. Yang, and J. Zhu. A new k-ε eddy viscosity model for high reynolds number turbulent flows. *Computers & Fluids*, 24(3):227 – 238, 1995.

[123] ANSYS, Inc., Southpointe, 275 Technology Drive, Canonsburg, PA 15317. *ANSYS Fluent User's Guide*, 15.0 edition, November 2013.

[124] M. B. Wilkinson, J. Van der Spuy, and T. W. Von Backström. Performance Testing of an Axial Flow Fan Designed for Air-Cooled Heat Exchanger Applications. Volume 1: Aircraft Engine; Fans and Blowers; Marine, 06 2018. V001T09A005.

[125] T. Sun, P. Petrie-Repar, D. M. Vogt, and A. Hou. Detached-Eddy Simulation Applied to Aeroelastic Stability Analysis in a Last-Stage Steam Turbine Blade. *Journal of Turbomachinery*, 141(9), 05 2019.

[126] D. J. Hill and J. J. Defoe. Scaling of Incidence Variations With Inlet Distortion for a Transonic Axial Compressor. *Journal of Turbomachinery*, 142(2), 01 2020.

[127] I. Hashem, H. S. Abdel Hameed, and M.H. Mohamed. An axial turbine in an innovative oscillating water column (owc) device for sea-wave energy conversion. *Ocean Engineering*, 164:536 – 562, 2018.

[128] R. Valizadeh, M. Abbaspour, and M. T. Rahni. A low cost hydrokinetic Wells turbine system for oceanic surface waves energy harvesting. *Renewable Energy*, 156:610 – 623, 2020.

[129] T. Ghisu, P. Puddu, and F. Cambuli. Physical explanation of the hysteresis in Wells turbines: A critical reconsideration. *Journal of Fluids Engineering, Transactions of the ASME*, 138(11), 2016.

[130] T. Ghisu, P. Puddu, and F. Cambuli. A detailed analysis of the unsteady flow within a Wells turbine. *Proceedings of the Institution of Mechanical Engineers, Part A: Journal of Power and Energy*, 231(3):197–214, 2017.

[131] T. Ghisu, P. Puddu, F. Cambuli, and I. Virdis. On the hysteretic behaviour of Wells turbines. *Proceedings of the 72nd Italian National Congress ATI*, 126:706–713, 2017.

[132] T. Ghisu, F. Cambuli, P. Puddu, I. Virdis, M. Carta, and F. Licheri. A critical examination of the hysteresis in Wells turbines using computational fluid dynamics and lumped parameter models. *Journal of Offshore Mechanics and Arctic Engineering*, 142(5), 2020.

[133] C.J. Freitas. Journal of fluids engineering editorial policy statement on the control of numerical accuracy. *Journal of Fluids Engineering, Transactions of the ASME*, 115(3):339–340, 1993.

[134] P. J. Roache, K. N. Ghia, and F. M. White. Editorial Policy Statement on the Control of Numerical Accuracy. *Journal of Fluids Engineering*, 108(1):2–2, 03 1986.

[135] F. Stern, R. V. Wilson, H. W. Coleman, and E. G. Paterson. Comprehensive Approach to Verification and Validation of CFD Simulations—Part 1: Methodology and Procedures . *Journal of Fluids Engineering*, 123(4):793–802, 07 2001.

[136] I. B. Celik, U. Ghia, P. J. Roache, C. J. Freitas, H. Coleman, and P. E. Raad. Procedure for Estimation and Reporting of Uncertainty Due to Discretization in CFD Applications. *Journal of Fluids Engineering*, 130(7), 07 2008.

[137] T. Ghisu, F. Cambuli, P. Puddu, I. Virdis, and M. Carta. Discussion on “Unsteady RANS simulations of Wells turbine under transient flow conditions” by Hu and Li. *Journal of Offshore Mechanics and Arctic Engineering*, 141(4):045501–045501–5, 2019.

[138] A. Brito-Melo, F. Neuman, and A. J N A Sarmento. Full-scale data assessment in OWC Pico plant. *Proceedings of the International Journal of Offshore and Polar Engineering*, 18(1):27–34, 2008.

[139] A. J. Garrido, E. Otaola, I. Garrido, J. Lekube, F. J. Maseda, P. Liria, and J. Mader. Mathematical Modeling of Oscillating Water Columns Wave-Structure Interaction in Ocean Energy Plants. *Mathematical Problems in Engineering*, pages –, 2015.

[140] T. Ghisu, P. Puddu, F. Cambuli, N. Mandas, P. Seshadri, and G.T. Parks. Discussion on “Performance analysis of Wells turbine blades using the entropy generation minimization method” by Shehata, A. S., Saqr, K. M., Xiao, Q., Shahadeh, M. F. and Day, A. *Renewable Energy*, 118:386–392, 2018.

[141] L. W. Carr, K. W. McAlister, and W. J. McCroskey. Analysis of the development of dynamic stall based on oscillating airfoil experiments. Technical Report NASA Technical Note D-8382, NASA AMES Research Center, 1977.

[142] L. E. Ericsson and J. P. Reding. Fluid mechanics of dynamic stall: Part 1 unsteady flow concepts. *Journal of Fluids and Structures*, 2:1–33, 1988.

[143] G. N. Barakos and D. Drikakis. Computational study of unsteady turbulent flows around oscillating and ramping aerofoils. *International Journal for Numerical Methods in Fluids*, 186:163–186, 2003.

[144] T. Ghisu, F. Cambuli, P. Puddu, I. Virdis, M. Carta, and F. Licheri. A lumped parameter model to explain the cause of the hysteresis in OWC-Wells turbine systems for wave energy conversion. *Applied Ocean Research*, 94:101994, 2020.

[145] S. Mittal and P. Saxena. Prediction of hysteresis associated with the static stall of an airfoil. *AIAA journal*, 38(5):933–935, 2000.

[146] H. Sarlak, A. Frère, R. Mikkelsen, and J.N. Sørensen. Experimental investigation of static stall hysteresis and 3-dimensional flow structures for an nrel s826 wing section of finite span. *Energies*, 11(6), 2018.

[147] F. R. Menter. Performance of popular turbulence models for attached and separated adverse pressure gradient flows. *AIAA Journal*, 30(8):2066–2072, 1992.

[148] F.R. Menter. Two-equation eddy-viscosity turbulence models for engineering applications. *AIAA Journal*, 32(8):1598–1605, 1994.

[149] D. Li, H. Wang, Y. Qin, L. Han, X. Wei, and D. Qin. Entropy production analysis of hysteresis characteristic of a pump-turbine model. *Energy Conversion and Management*, 149:175 – 191, 2017.

[150] K. J. Fidkowski, M. A. Ceze, and P. L. Roe. Entropy-based drag-error estimation and mesh adaptation in two dimensions. *Journal of Aircraft*, 49(5):1485–1496, 2012.

[151] M. Mizoguchi, Y. Kajikawa, and H. Itoh. Static stall hysteresis of low-aspect-ratio wings. *Proceedings of the 32nd AIAA Applied Aerodynamics Conference*, 2014.

[152] R. Modarres, D.A. Peters, and J. Gaskill. Dynamic stall model with circulation pulse and static hysteresis for naca 0012 and vr-12 airfoils. *Journal of the American Helicopter Society*, 61(3), 2016.

[153] A. Thakker and R. Abdulhadi. Effect of blade profile on the performance of Wells turbine under unidirectional sinusoidal and real sea flow conditions. *International Journal of Rotating Machinery*, 2007, 2007.

[154] T. H. Kim, T. Setoguchi, M. Takao, K. Kaneko, and S. Santhakumar. Study of turbine with self-pitch controlled blades for wave energy conversion. *International Journal of Thermal Sciences*, 41(1):101–107, 2002.

[155] T. Ghisu, F. Cambuli, P. Puddu, I. Virdis, M. Carta, and F. Licheri. A lumped parameter model to explain the cause of the hysteresis in OWC-Wells turbine systems for wave energy conversion. *Applied Ocean Research*, 94:101994, 2020.

[156] S. Camporeale, P. Filianoti, and M. Torresi. Performance of a Wells turbine in a owc device in comparison to laboratory tests. *Proceedings of the 9th European Wave and Tidal Energy Conference (EWTEC2011)*, pages –, 01 2011.

[157] R. Starzmann and T. Carolus. Model-based selection of full-scale Wells turbines for ocean wave energy conversion and prediction of their aerodynamic and acoustic performances. *Proceedings of the Institution of Mechanical Engineers, Part A: Journal of Power and Energy*, 228(1):2–16, 2014.

[158] S. Raghunathan. A methodology for Wells turbine design for wave energy conversion. *Proceedings of the Institution of Mechanical Engineers, Part A: Journal of Power and Energy*, 209(3):221–232, 1995.

[159] F. Licheri. Progetto di una turbina Wells a calettamento variabile. Master's thesis, Cagliari State University, Cagliari (IT), A.A. 2017-18.

[160] H. W. Coleman and W. Glenn Steele. *Experimentation, Validation, and Uncertainty Analysis for Engineers.* John Wiley & Sons, Ltd, 2009.

[161] A. Notaristefano, P. Gaetani, V. Dossena, and A. Fusetti. Uncertainty Evaluation on Multi-Hole Aerodynamic Pressure Probes. *Journal of Turbomachinery*, 143(9), 05 2021. 091001.

[162] H. Fujita and L. S. G. Kovasznay. Measurement of reynolds stress by a single rotated hot wire anemometer. *Review of Scientific Instruments*, 39(9):1351–1355, 1968.

[163] X. He. Measurement with a rotating slant-sensor probe. *Dantec Information*, (6):9–12, 02 1988.

[164] P. Puddu. Tip leakage flow characteristics downstream of an axial flow fan. *Proceedings of the ASME Turbo Expo 1996*, Volume 1: Turbomachinery, 06 1996.

[165] F. Lòpez Penã and T. Arts. The rotating slanted hot wire anemometer in practical use. *Proceedings of the 2nd International Conference on Experimental Fluid Mechanics (ICEFM'94) - Torino*, pages 388–399, July 4-8 1994.

[166] N. Erriu, N. Mandas, and P. Puddu. Alcune considerazioni sulla valutazione dell'incertezza nelle misure con anemometro a filo caldo. *Proceedings of MISMAC VII Quartu S. Elena*, 2001.

[167] F. Nurzia and P. Puddu. Experimental investigation of secondary flows in a low hub-tip ratio fan. *Proceedings of the ASME Turbo Expo 1994*, Volume 1: Turbomachinery, 06 1994.

[168] L. V. King and H. T. Barnes. Xii. on the convection of heat from small cylinders in a stream of fluid: Determination of the convection constants of small platinum wires with applications to hot-wire anemometry. *Philosophical Transactions of the Royal Society of London. Series A, Containing Papers of a Mathematical or Physical Character*, 214(509-522):373–432, 1914.

[169] F. Jørgensen. Directional sensitivity of wire and fiber film probes. *Tech. Rep. DISA information*, pages 11–31, 1971.

[170] P. Puddu. Misure di turbolenza in elementi fissi e rotanti di turbomacchine con l'impiego di sonde a filo caldo. *Proceedings of MIS-MAC II Firenze*, 1993.

[171] K. D. Jensen. Flow measurements. *Journal of the Brazilian Society of Mechanical Sciences and Engineering*, XXIV(4):400–419, 12 2004.

[172] M. Amundarain, M. Alberdi, A.J. Garrido, I. Garrido, and J. Maseda. Wave energy plants: Control strategies for avoiding the stalling behaviour in the Wells turbine. *Renewable Energy*, 35(12):2639–2648, 2010.

[173] O. Barambones, J.A. Cortajarena, J.M. Gonzalez de Durana, and P. Alkorta. A real time sliding mode control for a wave energy converter based on a Wells turbine. *Ocean Engineering*, 163:275–287, 2018.

[174] J. Lekube, A.J. Garrido, and I. Garrido. Variable speed control in Wells turbine-based oscillating water column devices: Optimum rotational speed. *Proceedings of the 6th International Conference on Power Science and Engineering ICPSE2017*, 136(1), 2018.

[175] J. Lekube, A.J. Garrido, I. Garrido, E. Otaola, and J. Maseda. Flow control in Wells turbines for harnessing maximum wave power. *Sensors (Switzerland)*, 18(2), 2018.

[176] S. K. Mishra, S. Purwar, and N. Kishor. An optimal and non-linear speed control of oscillating water column wave energy plant with Wells turbine and dfig. *International Journal of Renewable Energy Research*, 6(3):995–1006, 2016.

[177] S. Ceballos, J. Rea, I. Lopez, J. Pou, E. Robles, and D.L. Osullivan. Efficiency optimization in low inertia Wells turbine-oscillating water column devices. *IEEE Transactions on Energy Conversion*, 28(3):553–564, 2013.

[178] L. M. C. Gato, L. R. C. Eca, and A. F. de O. Falcao. Performance of the Wells turbine with variable pitch rotor blades. *Journal of Energy Resources Technology*, 113(3):141–146, 09 1991.

[179] F. A. Di Bella. Development of a Wave energy-responsive self-actuated blade articulation mechanism for an OWC turbine. *American Recovery and Reinvestment Act of 2009*, 6 2010.

[180] J. R. M. Taylor and N. J. Caldwell. Design and construction of the variable-pitch air turbine for the Azores wave energy plant. *Proceedings of the 3rd European Wave Power Conference*, pages 7–12, October 1998.

[181] T. Ghisu, P. Puddu, and F. Cambuli. A comparison between experimental and numerical analysis of a Wells turbine. *11th European Conference on Turbomachinery Fluid Dynamics and Thermodynamics, ETC 2015*, 03 2015.

[182] A. L. Treaster and A. M. Yocum. The calibration and application of five-hole probes. *Proceedings of the 24th International Instrumentation Symposium*, pages 255–266, 01 1978.